Nanometer-sized Aerosol Particles in the Atmosphere: Measurement, Analysis, and Impact

Thesis by
Weimeng (Stephanie) Kong

In Partial Fulfillment of the Requirements for the
Degree of
Doctor of Philosophy

CALIFORNIA INSTITUTE OF TECHNOLOGY
Pasadena, California

2020
Defended June 19, 2020

Weimeng (Stephanie) Kong
ORCID: 0000-0002-9432-2857

ACKNOWLEDGEMENTS

In the beginning, I would like to express my sincere gratitude to my advisors Dr. John Seinfeld and Dr. Richard Flagan for guiding me well throughout this adventure and encouraging me to grow as an independent scientist. John, thank you for inspiring my passion for aerosol research and teaching me to always stay curious and keep learning; Rick, thank you for encouraging me to pursue a career in science policy and offering guidance when I need the most, whether it is a surprise visit to your office, or a random video call from the US to Finland. It has truly been a privilege to work with both of you in the past five years. Besides my advisors, my sincere thanks also go the other members of my thesis advisory committee, Dr. Zhen-gang Wang and Dr. Mitchio Okumura, for their insightful comments and encouragement. I would also like to acknowledge the generous support from the National Science Foundation, the NASA Airborne Science Program and the Naval Postgraduate School.

Many graduate students and postdoctoral researchers in the Seinfeld and Flagan lab have helped me throughout my time at Caltech. In particular, I am grateful to Yuanlong Huang, Stavros Amanatidis, and Huajun Mai for introducing me to the realm and the beauty of instrumentation development. To Dr. Tran Nguyen, although we did not overlap for a long time at Caltech, it was a great pleasure to work with you on ICARUS. Additionally, I thank Sophia Charan, Ryan Ward, Ben Schulze, Chris Kenseth, Reina Buenconsejo, Becky Schwantes, and Kelvin Bates, for all the exciting collaborative projects that we worked together. To Elyse Pennington, thank you for the company, from Claremont to Pasadena. I also appreciate all the support from my fellow labmates, Brigitte Rooney, Wilton Mui, Changhyuk Kim, Atsushi Matsuki, Buddhi Pushpawela, and Renee McVay.

I will always remember my colleagues and coworkers at CLOUD, for the sleepless nights in the T11 and for the fun we had exploring Geneva, Stockholm, Wengen, and Helsinki. I wholeheartedly appreciate all the guidance from Dr. Jasper Kirkby and Dr. Neil Donahue, and I feel very lucky to work with Mingyi Wang and Ruby Marten on the runaway growth project.

To my undergraduate advisor, role model, and friend, Dr. Lelia Hawkins, I would not be who I am today without you. I sincerely appreciate your continuous support and encouragement, from my sophomore year at Harvey Mudd College until now.

Thank you for convincing me that I should pursue a doctoral degree in atmospheric science, which is one of the best and rewarding, yet hard, experiences I have had so far.

To my friends who motivated me throughout this journey: thank you all for always supporting me, encouraging me, and making sure that I have a life outside Caltech. Thanks to Ge Jin who has been a sturdy shelter for me ever since our freshman year in high school, regardless of how far apart we are; to the "Squad": Amis Pan, Taotao Zhou, and Yushuang Sun, for laughing and crying with me, exploring our "La La Land" together, being my partners-in-crime, and sharing the love for Zipper, Chloe, and Infinite; to my roommates Yanzhe Zhu and Alison Wu, for being the best company during the COVID-19 crisis, for taking care of me when I was not at my best, and for all the food adventures, work-out sessions, long and deep chats, and holiday or birthday parties, whether it be 2 p.m. or 2 a.m.; to Ji Su Lee, Alex An, Obosa Obazuaye, and Bruce Yan, for being there for me with a helping hand or a word of advice whenever I need you; to Hao Xie, for being my best surfing buddy and a great listener; to Xinran Liu, Zach Wu, Xinyan Liu, and my fellow Chemical Engineering graduate students, for all the fun working together on homework and projects in our first year; to Jinglin Huang, Sam Zhang, Jing Li, Siteng Fan, and many others from the Caltech Graduate Student Council, the Caltech Y, and the Caltech International Student Program, for making my life in graduate school more enjoyable and meaningful. To Chloe, Hengheng, and Heehee, you will be missed.

Lastly, I am grateful to my parents and my grandparents for their unconditional love, patience, and encouragement. Staying 6,000 miles away from my family for ten years has not been easy for me, and yet it is just as difficult, if not more, for you. The distance, however, did not prevent you from keeping me sane and grounded. You mean the whole world to me. I love you.

ABSTRACT

New particle formation (NPF) from gaseous precursor vapors is frequently observed in the ambient environment and contributes to a major source of global cloud condensation nuclei (CCN). The survival and CCN activation of newly formed particles are highly dependent on particle growth below 10 nm. Characterizing and understanding nanoparticle early growth will therefore help to quantify the impact of NPF on cloud reflectivity and global energy budget. In this work, I first present a recently developed instrument, the Caltech nano-Scanning Electrical Mobility Spectrometer (nSEMS), which consists of a charge conditioner, a novel differential mobility analyzer (DMA), and a two-stage condensation particle counter (CPC). This new design, coupled with a data inversion method that combines empirical calibration and COMSOL simulation, can help to measure nanoparticle size distributions from 1.5 nm to 25 nm more accurately. This instrument was employed in the experiments conducted in the Cosmics Leaving OUtdoor Droplets (CLOUD) chamber at the European Organization for Nuclear Research (CERN) to better understand NPF, particle growth and survival. Multiple experimental parameters were varied to study the influence of different highly oxygenated molecules (HOMs) and inorganic trace gases, such as ammonia and nitrogen oxides on particle early growth. Experiment results have suggested a novel mechanism that may help to explain nanoparticle formation and growth in highly polluted urban environments or in the cold free troposphere. In as little as a few minutes, freshly nucleated particles as small as 2 nanometers in diameter can grow very rapidly due to simultaneous condensation of nitric acid and ammonia. This can help them to survive through the so-called "valley of death" where they would otherwise be lost to larger particles, and instead allow them to grow to sizes where they are less vulnerable to loss and can continue on to sizes where they influence local air quality or climate. Further, the laboratory results of nanoparticle growth were incorporated into the Global Model of Aerosol Processes (GLOMAP) model to study the impact of this extremely rapid growth on the global CCN budget. Having realized the importance of conducting well-controlled chamber experiments and of using chamber experimental data, we established an online data infrastructure, the Index of Chamber Atmospheric Research in the United States (ICARUS), for storing, sharing, and using chamber data. A combined effort of the described works contributes to better measuring the size distribution of nanoparticles and to understanding their impact on global climate.

PUBLISHED CONTENT AND CONTRIBUTIONS

W. Kong, S. Amanatidis, H. Mai, C. Kim, B. Schulze, Y. Huang, G. Lewis, S. V. Hering, J. H. Seinfeld, and R. C. Flagan (2020). "The nano-scanning electrical mobility spectrometer (nSEMS) and its application to size distribution measurements of 1.5-25 nm particles". In: *Atmospheric Measurement Techniques*. Submitted.
W.K. designed and conducted the experiment, assisted in building the instrument and running the simulation, analyzed the data, and wrote the manuscript for this project.

M. Wang, W. Kong*, R. Marten, and the CLOUD Collaboration (May 2020). "Rapid growth of new atmospheric particles by nitric acid and ammonia condensation". In: *Nature* 581.7807, pp. 184–189. ISSN: 1476-4687. DOI: 10.1038/s41586-020-2270-4.
*These authors contributed equally to this work. W.K. prepared the CLOUD measuring instruments, collected the data, contributed to the scientific discussion, and wrote the manuscript for this project.

R. H. Schwantes, S. M. Charan, K. H. Bates, Y. Huang, T. B. Nguyen, H. Mai, W. Kong, R. C. Flagan, and J. H. Seinfeld (2019). "Low-volatility compounds contribute significantly to isoprene secondary organic aerosol (SOA) under high-NO_x conditions". In: *Atmospheric Chemistry and Physics* 19.11, pp. 7255–7278. DOI: 10.5194/acp-19-7255-2019.
W.K. assisted in DMA operation and data analysis for this project.

S. Charan, W. Kong, R. C. Flagan, and J. H. Seinfeld (2018). "Effect of particle charge on aerosol dynamics in Teflon environmental chambers". In: *Aerosol Science and Technology* 52.8, pp. 854–871. DOI: 10.1080/02786826.2018.1474167.
W.K. designed and conducted the experiments, and analyzed the DMA data for this project.

O. V. Kalashnikova, M. J. Garay, K. H. Bates, C. M. Kenseth, W. Kong, C. D. Cappa, A. I. Lyapustin, H. H. Jonsson, F. C. Seidel, F. Xu, D. J. Diner, and J. H. Seinfeld (2018). "Photopolarimetric Sensitivity to Black Carbon Content of Wildfire Smoke: Results From the 2016 ImPACT-PM Field Campaign". In: *Journal of Geophysical Research: Atmospheres* 123.10, pp. 5376–5396. DOI: 10.1029/2017JD028032.
W.K. collected and analyzed field data for this project.

H. Mai, W. Kong, J. H. Seinfeld, and R. C. Flagan (2018). "Scanning DMA data analysis II. Integrated DMA-CPC instrument response and data inversion". In: *Aerosol Science and Technology* 52.12, pp. 1400–1414. DOI: 10.1080/02786826.2018.1528006.
W.K. conducted the experiments and assisted in data analysis and model development for this project.

D. Stolzenburg, M. Simon, A. Ranjithkumar, and the CLOUD Collaboration (June 25, 2020). "Enhanced growth rate of atmospheric particles from sulfuric acid". In: *Atmospheric Chemistry and Physics* 20 (12), pp. 7359–7372. DOI: 10.5194/acp-20-7359-2020.
W.K. prepared the CLOUD measuring instruments and collected the data for this project.

B. C. Schulze, S. M. Charan, C. M. Kenseth, W. Kong, K. H. Bates, W. Williams, A. R. Metcalf, H. H. Jonsson, R. Woods, A. Sorooshian, R. C. Flagan, and J. H. Seinfeld (June 3, 2020). "Characterization of aerosol hygroscopicity over the Northeast Pacific Ocean: Impacts on prediction of CCN and stratocumulus cloud droplet number concentrations". In: *Journal of Geophysical Research: Earth and Space* 7 (7). DOI: 10.1029/2020EA001098.
W.K. collected and analyzed field data for this project.

M. Simon, L. Dada, M. Heinritzi, and the CLOUD Collaboration (Aug 3, 2020). "Molecular understanding of new-particle formation from α-pinene between −50 and +25 ^{o}C". English. In: *Atmospheric Chemistry and Physics Discussions* 20 (15), pp. 9183–9207. ISSN: 1680-7316. DOI: 10.5194/acp-20-9183-2020.
W.K. prepared the CLOUD measuring instruments and collected the data for this project.

TABLE OF CONTENTS

LIST OF ILLUSTRATIONS

LIST OF TABLES

NOMENCLATURE

CERN. European Organization for Nuclear Research.

CI-APi-TOF. Chemical Ionization with the Atmospheric Pressure interface Time-Of-Flight Mass Spectrometer, often used for molecular sulfuric acid detection.

CLOUD. Cosmics Leaving OUtdoor Droplets, an experiment being run at CERN to investigate the microphysics between galactic cosmic rays (GCRs) and new aerosol particles under controlled conditions.

CPC. Condensation Particle Counter, a particle counter that detects and counts aerosol particles by first growing them by condensing supersaturated vapors on particle seeds.

CS. Condensation sink, a parameter to quantify the rate of vapor condensation onto an existing aerosol population.

DMA. Differential Mobility Analyzer, the classifier component in an SEMS or SMPS system that selects particles of different sizes.

FIGAERO-CIMS. Chemical Ionization Time-Of-Flight Mass Spectrometer equipped with a Filter Inlet for Gases and AEROsols, a mass spectrometer that measures aerosol composition.

GCR. Galactic cosmic rays, high-energy protons and atomic nuclei that move through the space.

GLOMAP. Global Model of Aerosol Processes, a box model that studies aerosol microphysics on a large scale.

GR. Growth rates, a parameter to describe how fast nanoparticles grow, given in nm/h.

HOM. Highly oxygenated molecules, formed from autoxidation involving peroxy radicals arising from volatile organic compounds.

ICARUS. Index of Chamber Atmospheric Research in the United States, an online database for atmospheric chamber data storing, sharing, and using.

MABNAG. Model for Acid-Base Chemistry in Nanoparticle Growth, a model that studies the effect of salt formation on nanoparticle growth.

NPF. New particle formation, a process where nanometer-sized atmospheric particles form from gaseous reactions.

PTR-TOF-MS. Proton Transfer Reaction Time-of-Flight Mass Spectrometry, an instrument that detects volatile organic compounds.

SEMS. Scanning Electrical Mobility Spectrometer, an instrument that uses electrical mobility to measure aerosol particle diameters, also known as a Scanning Mobility Particle Sizer, or SMPS.

VOC. Volatile organic compounds, organic chemicals that have high vapor pressures at ambient conditions.

Chapter 1

INTRODUCTION

1.1 Background and Motivation

A more accurate estimation of cloud formation and cloud reflectivity can substantially improve our understanding of global solar radiation and climate (IPCC, 2013). Because most clouds owe their existence to aerosols, which can serve as tiny seeds for cloud formation, aerosol-cloud interactions remains one of the most important phenomena that must be quantified to evaluate the multiplex impact of atmospheric composition on climate.

Aerosols are minute solid or liquid particles suspended in the air, and they play an important role in the overall global energy balance and climate. They can scatter or absorb sunlight and thus directly affect the Earth's solar radiation. In addition, because aerosols participate in cloud formation, they can indirectly alter cloud reflectivity and Earth's albedo (IPCC, 2013). Aerosol particles can exist in sizes from 10^{-4} to 10 μm, falling under the following categories: nucleation mode (< 10 nm), Aitken mode (10 to 100 nm), accumulation mode (100 nm to 1μm), and coarse mode (> 1 μm) (Seinfeld and Pandis, 2006). Once aerosol particles are in the accumulation mode, they can act as cloud seeds for water vapors to condense on, which are called cloud condensation nuclei (CCNs). Size, composition, and other properties of CCNs can alter cloud brightness and reflectivity (Albrecht, 1989; Penner et al., 2004). Bright clouds block sunlight from reaching Earth's surface, and dark clouds keep the Earth warm. In spite of their small sizes, particles in the nucleation mode have been estimated to contribute to half of the global CCN budget (Merikanto et al., 2009). These nanoparticles are formed through the nucleation of atmospheric condensable vapors and can grow from clusters to large size CCNs through condensation or coagulation, and thus influence cloud formation and climate (Fig1.1).

Atmospheric nucleation and new particle formation (NPF) are frequently observed across the globe: in deserted forests, highly polluted megacities, coastal sites, polar regions, or the remote free troposphere (Kulmala et al., 2004; Sihto et al., 2011; Guo et al., 2014; Kerminen et al., 2018; Lee et al., 2019). Field observations have shown that NPF in the free troposphere and its subsequent downward transport to the

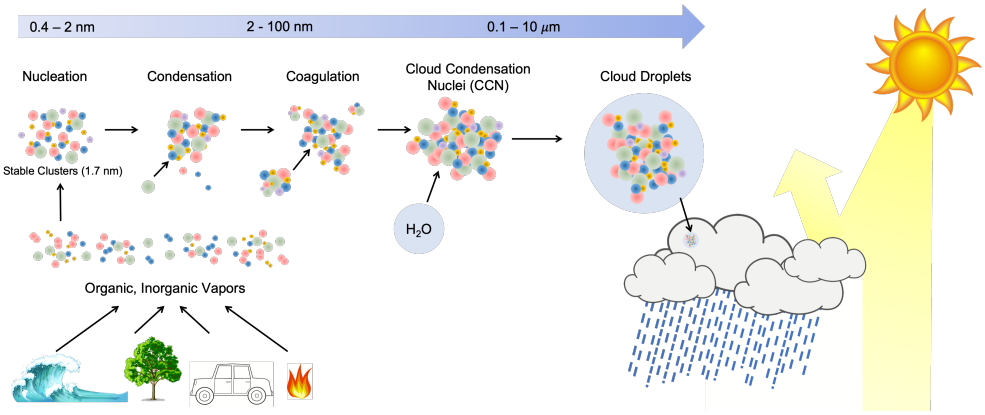

Figure 1.1: A schematic showing the complication and importance of new particle formation and growth in the atmosphere. Inorganic and organic vapors from a variety of sources can form nucleating clusters which stabilize at around 1.7 nm. These clusters can further grow to fine particles (CCNs) through condensation or coagulation, which involves complex physical and chemical processes that could not be fully incorporated into current global models. The failure to capture these processes has resulted in the greatest uncertainty in estimating and interpreting Earth's changing energy budget.

boundary layer has a significant impact on the CCN concentrations and low clouds formation, which is a major uncertainty source for calculating the Earth's radiative forcing (IPCC, 2013; Rose et al., 2017). For example, a rapid downward transport of nanoparticles was observed during the GoAmazon2014/5 campaign through precipitation, which influenced cloud properties in the pristine boundary layer (Wang et al., 2016). In addition to the campaign in the Amazon, the NASA Atmospheric Tomography Mission results indicated that NPF in the upper troposphere persists at all longitudes across the tropical band of the globe, which covers about 40% of Earth's surface, and is a globally important source of CCNs in the lower troposphere (Williamson et al., 2019). Other than its impact on clouds, NPF is believed to be a major contributor to urban smog and haze formation in populated cities, which raises significant health concerns that are related to human exposures to particulate matter (Anderson et al., 2012; Guo et al., 2014; Yao et al., 2018). Compared to large particles, these tiny nanoparticles freshly formed from nucleation are believed to exert the most severe health effects, since they are small enough to be deposited in the pulmonary region or to penetrate into bloodstream (Lee et al., 2019).

Given the significance of NPF in both climate and human health, it is crucial for us scientists to better study this process and to evaluate its impact. Despite the rigorous efforts that have been made to measure, characterize, and understand NPF, there are

many challenges lying ahead. For instance, particle-size distribution measurement in the low-nanometer regime suffers great uncertainties due to the low transmission efficiencies in conventional sizing instrument because small particles are more prone to high diffusional losses (Jiang et al., 2011). Although field observations have provided valuable information on NPF, the mechanism of nucleation and NPF can only be understood if isolated from other atmospheric processes, which will require precisely controlled laboratory setup with state-of-the-art measurement techniques. The explicit detailed schemes of NPF and its subsequent growth observed in laboratory are often too computationally expensive to include in large-scale modeling. Yet the current simplified representation of NPF and its contribution to cloud formation in current models cannot fully capture the importance of NPF on a global scale. Compared to the measurement data, models tend to underestimate the magnitude of NPF and subsequent growth of nanoparticles to CCN sizes (Williamson et al., 2019).

1.2 Content and Organization

In an effort to overcome the above challenges in understanding NPF and its impact, I have dedicated my dissertation work, included in the chapters and appendices of this thesis, to better measure, characterize, and quantify nanoparticle formation and its early growth (Figure 1.2). This dissertation aims to present advances in nanoparticle measuring techniques that can be used both in laboratory and field studies, demonstrate significant findings from well-controlled environmental chamber studies, bridge the discrepancies between modeling and observations, and establish a new platform to better organize, share, and use environmental chamber data.

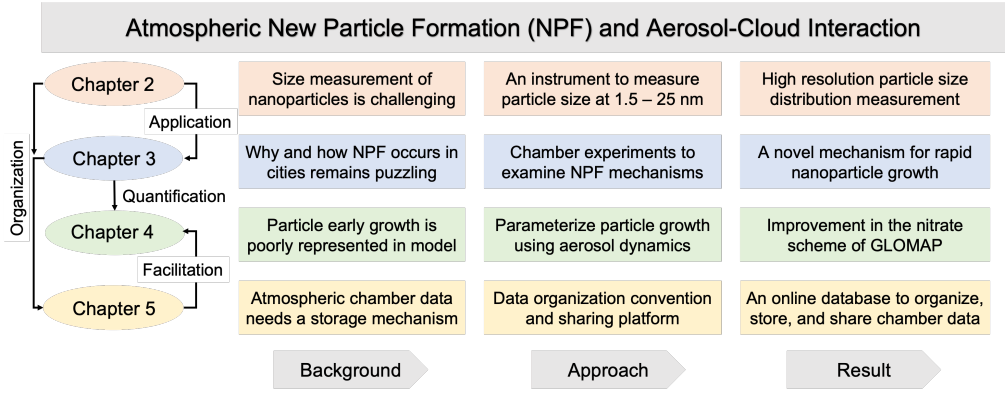

Figure 1.2: Organizational roadmap of this dissertation on investigating atmospheric new particle formation and aerosol-cloud interaction

Chapter 2: Instrumentation Development

Nanoparticle size distributions measured from conventional differential mobility analyzers often suffer great uncertainties in the small size range (< 10 nm) due to particle diffusional loss and biased data interpretation. The Caltech nano-Scanning Electrical Mobility Spectrometer (nSEMS) has demonstrated a better instrument performance in nanometer-sized range with a completely new design. The nSEMS consists of a soft x-ray charge conditioner, a novel particle classifier, and a two-stage condensation particle counter (CPC). The accuracy of data interpretation and inversion has also been enhanced using detailed numerical modeling of flows, fields, and particle trajectories. I characterized each individual component of the nSEMS and validated the integrated transfer function with empirical measurements. The viability of nSEMS has been proved by its successful application in experiments conducted in the Cosmics Leaving OUtdoor Droplets (CLOUD) chamber at the European Organization for Nuclear Research (CERN). The size distribution results acquired from the nSEMS during the CLOUD experiments have greatly improved our understanding of urban NPF.

Chapter 3: Laboratory Studies

How nanoparticles survive in urban environments remains one of the most puzzling topics in the field. If urban particle growth rates are similar to those found in cleaner environments (1-10 nm/h), then conventional understanding suggests that new urban particles should be rapidly scavenged by the high concentration of pre-existing particles. In order to better understand the chemical and physical processes of NPF in cities and isolate other factors that may affect nanoparticle growth, we conducted a number of experiments under various atmospheric conditions in the well-controlled CLOUD chamber. Multiple experimental parameters were varied to study the influence of different highly oxygenated molecules (HOMs) and inorganic trace gases, such as ammonia and nitrogen oxides on particle early growth. Our results suggest that below about +5 ^{O}C, nitric-acid and ammonia vapors can condense onto freshly nucleated particles as small as a few nanometers in diameter and the resulting particle growth rates can be extremely high, reaching well above 100 nm/h. This phenomenon is very likely to occur in inhomogeneous urban settings, especially in wintertime with strong local sources such as traffic, as well as vertical mixing. The results from this CLOUD study may help to explain how freshly nucleated particles can be shepherded through the smallest size range where they are most vulnerable to scavenging loss and survive to form larger particles even in highly polluted cities.

Chapter 4: Modeling and Impact

The explicit physical and chemical processes of nanoparticle growth derived from chamber studies, including those from CLOUD, are often too computationally expensive to include in large-scale modeling. To achieve the best trade-off between computation cost and accuracy, nanoparticle early growth results from CLOUD experiments have been parameterized using thermodynamic and kinetic principles. In order to capture the full picture of nanoparticle growth, survival, and activation, size distribution information from the nSEMS were compared and combined with other particle sizing instruments from CLOUD to obtain a continuous particle growth profile over the range from 1 to 500 nm. Nanoparticle growth was modeled as gas-to-particle condensational growth to compare with experimental measurements. The resulting parameter was defined as the condensational flux that contributes to particle growth. I then evaluated the parameter derived from the CLOUD experiments by incorporating it into the Global Model of Aerosol Processes (GLOMAP), which introduces a new convention of describing particle growth in box models.

Chapter 5: Database Development

The CLOUD experiments demonstrated the importance of conducting chamber experiments to study aerosols as they help to constrain experimental variables and to understand complicated processes and mechanisms. In order to better store, share, and use atmospheric chamber data in the U.S., the Index of Chamber Atmospheric Research in the United States (ICARUS) project aimed to create a sustainable web-based infrastructure for chamber data archiving and organization. An open-access website was established by our project to upload and store atmospheric chamber experimental data. I have also developed multiple software tools, experimental protocols, and data conventions to facilitate the data organization process.

References

B. A. Albrecht (Sept. 1989). "Aerosols, Cloud Microphysics, and Fractional Cloudiness". en. In: *Science* 245.4923, pp. 1227–1230. ISSN: 0036-8075, 1095-9203. DOI: 10.1126/science.245.4923.1227. (Visited on 05/06/2020).

J. O. Anderson et al. (2012). "Clearing the Air: A Review of the Effects of Particulate Matter Air Pollution on Human Health". In: *Journal of Medical Toxicology* 8.2, pp. 166–175. DOI: 10.1007/s13181-011-0203-1.

S. Guo et al. (2014). "Elucidating severe urban haze formation in China". In: *Proceedings of the National Academy of Sciences* 111.49, pp. 17, 373–17, 378. ISSN: 0027-8424. DOI: 10.1073/pnas.1419604111.

IPCC (2013). *Climate Change 2013: The Physical Science Basis*. Cambridge University Press, 32 Avenue of the Americas, New York, NY 10013-2473, USA.

J. Jiang et al. (2011). "Transfer Functions and Penetrations of Five Differential Mobility Analyzers for Sub-2 nm Particle Classification". In: *Aerosol Science and Technology* 45.4, pp. 480–492. DOI: 10.1080/02786826.2010.546819.

V.-M. Kerminen et al. (Sept. 2018). "Atmospheric new particle formation and growth: review of field observations". In: *Environmental Research Letters* 13.10, pp. 103, 003. DOI: 10.1088/1748-9326/aadf3c.

M. Kulmala et al. (Mar. 2004). "Formation and growth rates of ultrafine atmospheric particles: A review of observations". In: *Journal of Aerosol Science* 35, pp. 143–176. DOI: 10.1016/j.jaerosci.2003.10.003.

S.-H. Lee et al. (2019). "New Particle Formation in the Atmosphere: From Molecular Clusters to Global Climate". In: *Journal of Geophysical Research: Atmospheres* 124.13, pp. 7098–7146. DOI: 10.1029/2018JD029356.

J. Merikanto et al. (Nov. 2009). "Impact of nucleation on global CCN". In: *Atmospheric Chemistry and Physics* 9. DOI: 10.5194/acp-9-8601-2009.

J. E. Penner et al. (Jan. 2004). "Observational evidence of a change in radiative forcing due to the indirect aerosol effect". en. In: *Nature* 427.6971, pp. 231–234. ISSN: 1476-4687. DOI: 10.1038/nature02234. (Visited on 05/06/2020).

C. Rose et al. (2017). "CCN production by new particle formation in the free troposphere". In: *Atmospheric Chemistry and Physics* 17.2, pp. 1529–1541. DOI: 10.5194/acp-17-1529-2017.

J. H. Seinfeld and S. N. Pandis (2006). *Atmospheric Chemistry and Physics*. 2nd ed. Hoboken, New Jersey: John Wiley & Sons.

S.-L. Sihto et al. (2011). "Seasonal variation of CCN concentrations and aerosol activation properties in boreal forest". In: *Atmospheric Chemistry and Physics* 11.24, pp. 13269–13285. DOI: 10.5194/acp-11-13269-2011.

J. Wang et al. (2016). “Amazon boundary layer aerosol concentration sustained by vertical transport during rainfall”. In: *Nature* 539.7629, pp. 416–419. DOI: 10.1038/nature19819.

C. J. Williamson et al. (2019). “A large source of cloud condensation nuclei from new particle formation in the tropics”. In: *Nature* 574.7778, pp. 399–403. DOI: 10.1038/s41586-019-1638-9.

L. Yao et al. (2018). “Atmospheric new particle formation from sulfuric acid and amines in a Chinese megacity”. In: *Science* 361.6399, pp. 278–281. DOI: 10.1126/science.aao4839.

Chapter 2

THE NANO-SCANNING ELECTRICAL MOBILITY SPECTROMETER (NSEMS) AND ITS APPLICATION TO SIZE DISTRIBUTION MEASUREMENTS OF 1.5–25 NM PARTICLES

W. Kong, S. Amanatidis, H. Mai, C. Kim, B. Schulze, Y. Huang, G. Lewis, S. V. Hering, J. H. Seinfeld, and R. C. Flagan (2020). "The nano-scanning electrical mobility spectrometer (nSEMS) and its application to size distribution measurements of 1.5-25 nm particles". In: *Atmospheric Measurement Techniques*. Submitted.

abstract

Particle size measurement in the low nanometer regime is of great importance to the study of cloud formation and to better understand aerosol-climate interaction. Here we present the design, modeling, and experimental characterization of the nano-Scanning Electrical Mobility Spectrometer (nSEMS), a recently developed instrument that probes particle physical properties in the 1.5 - 25 nm range. The nSEMS consists of a charge conditioner, a novel differential mobility analyzer, and a two-stage condensation particle counter (CPC). The charge conditioner employs a soft x-ray bipolar ion source in a compact housing designed to optimize both nanoparticle charging and transmission efficiency. The mobility analyzer, a radial opposed migration ion and aerosol classifier (ROMIAC), can classify nanometer-sized particles with minimal degradation of its resolution or diffusional losses. The ROMIAC operates on a dual high-voltage supply with fast polarity-switching capability to minimize sensitivity to variations in the chemical nature of the ions used to charge the aerosol. Particles transmitted through the charge conditioner and mobility analyzer are measured using a two-stage CPC. They are first activated in a fast-mixing diethylene glycol (DEG) stage before being counted by a second detection stage, an ADI MAGIC^{TM} water-based CPC. The transfer function of the integrated instrument is derived from both finite-element modeling and experimental characterization. The nSEMS performance has been evaluated during measurement of transient nucleation and growth events in the CLOUD atmospheric chamber at CERN. We show that the nSEMS can provide high time and size resolution measurement of nanoparticles, and can capture the critical aerosol dynamics of newly formed atmospheric particles.

2.1 Introduction

Aerosol particles can either be emitted into the atmosphere directly from primary sources, or generated through the nucleation of atmospheric condensable precursor vapors. Atmospheric nucleation, or new particle formation (NPF), is frequently observed across the globe under diverse environmental conditions, ranging from populated urban centers (Dunn et al., 2004; Z. Wang et al., 2017; Yao et al., 2018; M. Wang et al., 2020) to remote areas such as forests or oceans (O'Dowd et al., 2002; Bonn and Moortgat, 2003; Paasonen et al., 2010; Dall'Osto et al., 2017), as well as in the free troposphere (Kulmala et al., 2004; Kerminen et al., 2018; Lee et al., 2019). Large-scale simulations and parameterizations suggest that NPF may generate half of the global cloud condensation nuclei (CCN, Merikanto et al., 2009; Gordon et al., 2017). In addition to their climate impact, ultrafine particles formed by nucleation can also have disproportionate adverse effects on human health (Brown et al., 2000).

To understand the formation and subsequent growth of freshly nucleated particles in the atmosphere and to evaluate their impact on climate and human health requires measurement techniques that can enable particle size distribution measurements in the low-nanometer regime. Nanoparticle sizing is often achieved using electrical mobility to separate charged particles according to the velocities with which they migrate in an electric field. The differential mobility analyzer (DMA) has long been the most widely used instrument to measure size distribution of sub-micron ($< 1\ \mu$m) aerosol particles (Knutson and Whitby, 1975; Flagan, 1998). Most DMAs separate charged aerosol particles of different electrical mobilities by applying an electric field between two coaxial electrodes that are parallel to a particle-free sheath flow. Classified particles from the DMAs are typically counted by a condensation particle counter (CPC) that uses supersaturated vapors to grow particle seeds before detection (Quant et al., 1992). This integrated instrument initially used step-wise variation in the voltage. By keeping the voltage applied between the electrodes constant at each step, particles are transmitted throughout the entire system under a steady field profile before they are counted by the CPC. This static-mode measurement system is referred to as the DMPS, or the differential mobility particle sizer (Fissan et al., 1983). However, since the DMPS often requires the system to reach a steady-state before any reliable measurement can be made, the relatively long residence time of the particles in the DMA makes it less ideal to capture transient aerosol activities. By continuously changing the voltage through an exponential ramp, the scanning electrical mobility spectrometer (SEMS; also known as the Scanning

Mobility Particle Sizer, SMPS) considerably accelerates the particle classification using electrical mobility (S. C. Wang and Flagan, 1990).

While the traditional SEMS can only detect particles with mobility-equivalent diameters above 10 nm, many efforts have focused on extending the classification range to smaller aerosol particles. The first major step in this direction was the Vienna short-column DMA that measured nanoparticles down to 3.5 nm (Winklmayr et al., 1991); the "nano-DMA", modified from the traditional long-column DMA design, can measure particle size distribution in the range of 3 - 50 nm (D. .-.-R. Chen et al., 1998); a radial DMA (RDMA) that classifies particles in a radial flow toward the center of parallel disk electrodes also demonstrated a high detection efficiency for particles between 3 - 10 nm (S.-H. Zhang et al., 1995). Both designs have been extended to smaller sizes. Through meticulous aerodynamic design and very large sheath flow rates, up to 1000 L/min, Rosell-Llompart et al. (1996) refined the Vienna DMA into one instrument suitable for particle classification down to as small as 1 nm. Brunelli et al. (2009) developed an RDMA that could also classify 1 nm particles at much more modest flow rates, albeit at lower resolution. An opposed migration aerosol classifier (OMAC) design uses a particle-free cross flow instead of the parallel sheath flow in the DMAs to balance particle electrical migration. Since the aerosol being classified fills the space between the electrodes, rather than occupying only a narrow slice of that space as in a DMA, this changes of the scaling for where diffusion begins to degrade the resolution of the classifier, thereby enabling classification at lower voltages, or operation at higher resolution than is possible with conventional DMAs (Flagan, 2004; Downard et al., 2011). The radial opposed migration ion and aerosol classifier (ROMIAC), a radial form of the OMAC, was prototyped and proved its capacity of measuring sub-2 nm particles or ions and even separating peptide stereoisomers owing to its high resolving power (Mui et al., 2013; Mui et al., 2017). The challenges with measuring particles in the low-nanometer regime lie not only in classification, but also in particle detection. Some single-stage CPCs have been operated at sufficiently high supersaturation to activate particles as small as 1 nm diameters, but in the experiment that requires high radiation environment for which this instrument was developed, this can lead to nucleation within the CPC. Therefore, we took a more conservative approach that has proven robust and effective for sub-10nm particle detection, namely a two-stage CPC, in which the first stage employs a low vapor pressure working fluid, typically diethylene glycol (DEG) that can activate small particles with minimal risk of homogeneous nucleation (Iida et al., 2009). Owing to the low vapor pressure, the

first stage does not grow particles to optically detectable size, so a second "booster" stage is used to grow the activated clusters and optically detect them. The second stage is typically a conventional CPC. The operation of two activation and growth systems in series compounds another challenge to SEMS/SMPS measurements; the residence time within the CPC can distribute counts of particles that exit the DMA over many time bins (Russell et al., 1995; Collins et al., 2002), thereby degrading the resolution of the instrument, especially for tiny nanoparticles for which resolution may already have been compromised due to diffusional broadening. This effect becomes increasingly important at scan rates that are fast relative to the response time of the CPC. Therefore, CPCs with a narrow distribution of residence times are preferred for a SEMS that targets the low-nanometer range.

In this work we show the development of a nano-scanning electrical mobility spectrometer (nSEMS) that features a soft x-ray aerosol charge conditioner, a fast-scanning ROMIAC particle classifier, and a two-stage CPC, to acquire fast and accurate particle size distributions in the range of 1.5 - 25 nm. The two-stage CPC includes a fast-mixing activation stage using DEG as working fluid, followed by an eco-friendly, fast-response, water-based CPC (Hering et al., 2019). Each component of the nSEMS was characterized separately; the integrated transfer function was derived based on both experimental results and finite-element modeling using COMSOL Multiphysics^{TM}. The nSEMS has been intensively used in the Cosmics Leaving OUtdoor Droplets (CLOUD) experiments at CERN. A comparison of nSEMS data with measurements from other well-calibrated particle sizing instruments at CLOUD confirms its capacity to provide reliable size distribution in the low-nanometer size regime.

2.2 The nSEMS Design and System Features

The nSEMS was designed to capture critical aerosol dynamics during atmospheric nucleation and subsequent nanoparticle growth, both in environmental chamber experiments and in ambient measurements. To this end, its design and operating parameters have been optimized to provide size distribution measurements with relatively high size resolution in the sub-25 nm range, and with a fairly short duty cycle. The nSEMS classifies particles of different sizes according to their electrical mobilities, Z_p, which is defined as the ratio of particle migration velocity, v_m, to the electric field strength within the classifier, E:

$$Z_p = \frac{v_m}{E} = \frac{\phi e C_c}{3\pi\mu d_p} \tag{2.1}$$

where ϕ is the net number of elementary charges, e, on the particle, C_c is the Cunningham slip correction factor that accounts for the noncontinuum effects, μ is the dynamic viscosity, and d_p is the particle diameter. Figure 2.1 shows a schematic of nSEMS main components; a soft x-ray charger, a ROMIAC that operates on a continuously varying voltage, and a two-stage CPC. Detailed operating parameters and default settings are summarized in Table 2.1. Particles entering a mobility-based sizing system typically pass through a charge conditioner to attain a known, steady-state charge distribution to enable accurate data inversion. The nSEMS charge conditioner employs a soft x-ray source that directly ionizes the air around the incoming particles. The charge conditioner can be remotely switched off to enable measurements based on the natural charge of ions or particles, if so desired. Although it remains challenging to determine the actual charging state of sub-20 nm particles (Lòpez-Yglesias and Flagan, 2013), the Fuchs charging efficiencies, f_c, used in electrical mobility calculations are approximated based on the Wiedensohler (1988) correlation for consistency with other studies (Tröstl et al., 2015; D. Stolzenburg et al., 2017) and to facilitate comparison with data from other instruments. While the ROMIAC only requires an aerosol sample flow rate of 1.2 L/min in the default setup, the charge conditioner pulls the aerosol at a higher flow rate (4.6 L/min) to overcome the high diffusional losses. The aerosol entering the ROMIAC is drawn from the core of the flow exiting the charge conditioner (M. R. Stolzenburg and McMurry, 1991). The charged nanoparticles transmitted through a core-sampling probe enter the ROMIAC at a flowrate of 1.2 L/min, tangentially into a flow distribution channel, and then enters the classification region through a narrow slit. Unlike traditional DMAs, where the particle-free sheath flow is parallel to the electrodes, ROMIAC uses a 12 L/min recirculated, filtered cross-flow that enters and exits the classification region through screen electrodes (Flagan, 2004; Mui et al., 2013; Mui et al., 2017). For nondiffusive particles, the ideal resolving power of the classifier, $\mathcal{R}_{\text{nom,nd}}$, is given as:

$$\mathcal{R}_{\text{nom,nd}} = \frac{1}{\beta\,(1 + |\delta|)} \tag{2.2}$$

for all of the designs, configurations or flow rate ratios (Flagan, 1999). The two flow factors, the imbalance factor, δ, and the aerosol-to-cross-flow ratio, β, are defined as:

$$\delta = \frac{Q_{\text{c}} - Q_{\text{a}}}{Q_{\text{a}} + Q_{\text{c}}},\ \beta = \frac{Q_{\text{a}} + Q_{\text{c}}}{Q_{\text{x, in}} + Q_{\text{x, out}}} \tag{2.3}$$

where Q_{a} is the incoming polydipersed aerosol flow rate, Q_{c} is that of the outgoing classified sample flow, and $Q_{\text{x, in}}$ and $Q_{\text{x, out}}$ are the entering and exiting cross

flow rates. If the incoming flows are balanced with the outgoing flows ($Q_a = Q_c$; $Q_{x,\,in} = Q_{x,\,out}$), then the two factors can be simplified to $\delta = 0$, $\beta = \mathcal{R}_{nom,nd}^{-1}$. A resolution of $\mathcal{R}_{nom,nd} = 10$ is generally sufficient to capture the critical cluster-to-ion formation process under ambient conditions. In order to get a reasonable size coverage to study the subsequent condensational or coagulational growth of newly formed nanoparticles, voltage is exponentially ramped between 20 V and 10,000 V with a characteristic time:

$$\tau_s = \frac{t_{ramp}}{\ln(V_{high}/V_{low})} \tag{2.4}$$

of approximately 8 s. The mean residence time of the sample flow in the classifier, τ_f, is:

$$\tau_f = \frac{\mathcal{V}_{class}}{Q_{class}} \tag{2.5}$$

with $\mathcal{V}_{class}$ and $Q_{class} = (Q_a + Q_c)/2$ corresponding to the volume and particle flow rates in the classification region. For the ROMIAC, $\mathcal{V}_{class} = \pi(R_2^2 - R_1^2)b$, where $R_1 = 0.24$ cm and $R_2 = 1.61$ cm are the inner/outer electrode radii, $b = 1$ cm is the gap between the high-voltage and ground electrodes, resulting in a classification volume $\mathcal{V}_{class} \simeq 8.0$ cm^3. The resulting mean gas residence time at the nominal aerosol flow rate is $\tau_f \simeq 0.4$ s. The mobility of the particles that is transmitted through an ideal, constant-voltage ROMIAC is:

$$Z_{p,ideal}^{*} = \frac{\left(Q_{x,\,in} + Q_{x,\,out}\right) b}{2\pi \left(R_2^2 - R_1^2\right) V^{*}} \tag{2.6}$$

where $Z_{p,ideal}^{*}$ can be treated as the centroid particle electrical mobility in scanning mode assuming highly idealized flow and electric fields and corresponds to the peak of the transfer functions (S.-H. Zhang et al., 1995; Mui et al., 2017). V^* is the corresponding voltage applied to the central electrode.

Most mobility-based particle sizing systems measure only one polarity of charged particles (usually positive) by employing a single polarity high-voltage supply. Since the nSEMS employs a soft x-ray ion source in the charge conditioner, the aerosol downstream of the charge conditioner contains both negatively and positively charged particles as they collide with ions of both polarities. Because ion properties, such as mass, mobility, and concentration, as well as experimental conditions can all affect particle charging efficiency, and the ions produced by the soft x-rays can vary due to trace species in the gas, measuring only particles with single polarity may lead to uncertainties and variabilities in computing particle concentrations (Steiner et al., 2014; X. Chen et al., 2018). To optimize instrument performance and avoid

potential variability in particle charging, the ROMIAC operates on a custom-built dual high-voltage supply with fast polarity-switching capability. In the default operating mode of the nSEMS, the polarity of the scanning voltage is switched at the start of every scan, but the polarity can also be fixed, either positive or negative, or it can be turned off to meet different scientific needs. This feature not only helps to better understand the performance of bipolar diffusion charging, it also enables measurement of the charge state of the sampled aerosol particles by deactivating the charge conditioner for some or all scans. This becomes an important feature when studying atmospheric nucleation as it enables discrimination between neutral and ion-mediated nucleation (Kirkby et al., 2016; Wagner et al., 2017).

Classified particles transmitted through the ROMIAC are subsequently detected by a two-stage CPC that enables particle counting approaching 1 nm in size (Iida et al., 2009). The first stage employs a fast-mixing condensational activation and growth reactor (J. Wang et al., 2002; Shah and Cocker, 2005) that uses DEG as the working fluid to activate the nanoparticles. As in the Airmodus particle-size magnifiers and the CPC of Sgro and J. F. d. l. Mora (2004), supersaturation is produced by turbulent mixing of the hot (70 °C) DEG vapor with cold (20 °C) particle-laden flow, at a flow rate of 0.3 and 1.2 L/min, respectively. The downstream growth tube is cooled to 10 °C to accelerate particle growth and remove excess vapor. In contrast to the Airmodus particle size magnifier (PSM) and the CPC of Sgro and J. F. d. l. Mora (2004), on which the PSM is based, the residence time in the activation stage of the present CPC has been minimized to speed instrument response. A modified ADI MAGIC^{TM} water-based CPC serves as the second stage to grow particles sufficiently large for optical detection (Hering et al., 2019). Particle counts are recorded over the nSEMS size distribution scan at 5Hz. The sample flow rate of the CPC is 1.00 L/min. Between the activation and booster stages, the flow is split between the water-CPC and a smaller excess flow to minimize deposition of excessive DEG vapor in the intervening plumbing and the water CPC.

Data acquisition and instrument control for the nSEMS are accomplished with a National Instruments^{TM} sbRIO-9637 CompactRIO single-board controller coupled with a Field Programmable Gate Array (FPGA) module. The FPGA module, which is programmable using LabVIEW 2018, is capable of operating at clock speeds up to 40 MHz with optimized hardware and memory settings. The FPGA is controlled by a microprocessor that runs on a real-time Linux operating system (OS), greatly reducing the overhead and response lag associated with typical LabVIEW applica-

tions running on other platforms. The real-time OS and FPGA enable independent time loops for precise control of the voltage exponential ramp and recording of CPC concentrations. The board controller is connected to a Windows PC via Ethernet, enabling communication among different programs, visualization of real-time data, and online monitoring of critical parameters without compromising instrument timing.

2.3 Characterization of the nSEMS

Compared to the DMPS, the SEMS can accelerate mobility-based size distribution measurements by classifying particles in a time-varying electric field and eliminating the transition time between measurement channels. Although the exponential voltage ramping allows investigation of rapidly evolving aerosol particles, it alters the particle trajectories in the classifier, such that the transfer function may differ significantly from that expected for a DMPS. Numerical simulations of particle trajectories in a scanning cylindrical DMA have shown that the width of instrument transfer function for fast scans can be significantly greater than that for a static DMA (Collins et al., 2004; Mai and Flagan, 2018; Mai et al., 2018). Similarly, voltage scanning of the ROMIAC may distort the transfer functions from those seen in static-mode operation.

Finite-element modeling of particle transmission

Both numerical simulations and derivations of analytical solutions for idealized instruments have proven to be powerful tools in the study of the transfer functions of DMAs operating in scanning mode (Collins et al., 2004; Dubey and Dhaniyala, 2011). However, the ROMIAC geometry and particle trajectories are more complicated than those in long-column cylindrical DMAs. In order to fully understand the flows, electric field, and particle trajectories inside a scanning ROMIAC, particle transmission has been examined with finite-element simulations using COMSOL Multiphysics® (Version 5.3).

We have solved Navier-Stokes and Maxwell equations for the flow and electric fields, respectively, using the "Laminar" and "Electrostatic" modules in COMSOL Multiphysics®. The time-varying electric field, $E_{(x,y,z,t)}$, can be treated as quasi-steady state:

$$E_{(x,y,z,t)} = E_0(x, y, z) f(t) \ , \tag{2.7}$$

where $E_0(x, y, z)$ is the electric field in the beginning of the voltage ramp at $V(t = 0) = V_{\text{low}}$, and $f(t)$ is the time variation factor depending on the characteristic

ramping time τ_s defined in Eq.(2.4):

$$f(t) = \begin{cases} 1, & 0 \le t < t_{\text{low}} \\ e^{\frac{t-t_{\text{low}}}{\tau_s}}, & t_{\text{low}} \le t < t_{\text{low}} + t_{\text{ramp}} \\ \dfrac{V_{\text{high}}}{V_{\text{low}}}, & t_{\text{low}} + t_{\text{ramp}} \le t < t_{\text{low}} + t_{\text{ramp}} + t_{\text{high}} \end{cases} \tag{2.8}$$

Because the particles classified in the ROMIAC are sufficiently small that their inertial effects can be neglected, particle motion is numerically simulated using the "Particle trajectories" module in COMSOL, with only the drag, electrostatic forces, and Brownian motion being considered, as the particles are assumed to be massless. The scanning ROMIAC transfer function is defined as

$$\Omega_{\text{ROMIAC}}(Z_{\text{p}}, \beta, \delta, t) = \frac{Q_{\text{c}}\, N_{\text{c}}(t)}{Q_{\text{a}}\, N_{\text{a}}}, \tag{2.9}$$

where N_{a} and N_{c} are the number of particles going in and coming out of the ROMIAC during the simulation. In order to determine the scanning ROMIAC transfer function with adequate time resolution, 200 particles are injected into the ROMIAC every 2.5 ms; simulations were performed for the default flows and voltage ramp settings listed in Table 2.1. The times at which particles enter and exit the scanning ROMIAC were recorded. Figure 2.2 shows an example of the finite-element solutions of the flow and electric fields for $d_{\text{p}} = 4$ nm particles. The modeled instrument response for particles with 13 different mobility diameters across the sizing range of the instrument are shown with solid lines in Figure 2.3. The peak transmission ratio for particles larger than about 5 nm remains flat, at approximately 60%, and progressively drops at smaller sizes. Simulation was also performed for different ramp times in order to compare the transfer function distortions that may result from fast voltage scanning (Figure 2.12).

Laboratory characterization of the ROMIAC

Although particle trajectory simulations using COMSOL Multiphysics® have proven very effective at retrieving particle transfer functions, they cannot fully capture the nonideal behavior of particles inside the classifier due to the high computation cost (Mai and Flagan, 2018; Amanatidis et al., 2020). As a result, experimental calibrations are needed to closely examine the scanning ROMIAC performance. Figure 2.4 shows the tandem differential mobility analyzer (TDMA, Rader and McMurry, 1986) calibration setup used; aerosols of a known size are selected with a classifier (a constant voltage ROMIAC or DMA for small, 1 - 20 nm, or

large, 12 - 26.5 nm, respectively) before entering the nSEMS. Depending on the target size range, source particles were generated from electrosprayed tetra-alkyl ammonium solutions (Ude and J. F. d. l. Mora, 2005), a heated Nichrome wire, or atomized sodium chloride solution. The polydisperse aerosols generated from the hotwire or the atomizer were size-selected by a ROMIAC or a cylindrical DMA operating at constant voltage to provide a narrow-mobility distribution sample for nSEMS calibration. In order for the size-selected source particles to approximate a monodisperse aerosol, both the cylindrical DMA and the classifying ROMIAC were run at higher resolution than the nSEMS standard operating condition ($\mathcal{R}_{nd} \geq 10$), using open-loop controlled sheath flow or cross flow, respectively.

Due to perturbations of the electric field and imperfections in the instrument fabrication, particle transmission in the ROMIAC can deviate from the designed performance. When the ROMIAC of the nSEMS is operated in static mode, correction factors can be determined empirically to account for any deviations from theoretical or numerical performance. In terms of particle sizing, an empirical mobility correction factor, f_z, can be calculated by comparing the experimental transfer function with the expected $Z^*_{\text{p,ideal}}$, as defined in Eq.(2.6) using the TDMA calibration setup (Mui et al., 2017). This correction factor, $f_z = Z^*_p / Z^*_{\text{p,ideal}}$, is estimated to be 1.03 for the ROMIAC classifier used in the nSEMS system.

Characterization of the two-stage CPC

In addition to the ROMIAC, nonideal performance of the two-stage CPC may also affect the nSEMS data acquisition and interpretation. Figure 2.5 shows the experimental setup that was used to measure the size-dependent detection efficiency of the two-stage CPC. The classifying ROMIAC was operated in static mode with a resolving power of $\mathcal{R}_{nd} = 10$. The hotwire particle generator was set at similar conditions as shown in Figure 2.4. An aerosol electrometer was placed in between the ROMIAC and the two-stage CPC to measure the total particle number concentrations coming out of the classifier. The plumbing upstream of the CPC was kept the same as on the integrated nSEMS system so that the resulting plumbing delays would be taken into account in this calibration. The CPC counting efficiency relative to that of the aerosol electrometer is shown in Figure 2.6. The 50% cut-off size is about 1.6 nm, and the counting efficiency reaches a plateau when particle mobility-equivalent diameter is larger than about 2.1 nm ($d_p \geq 2.1$nm). The empirically determined

two-stage CPC counting efficiency was fitted with a logistic function:

$$\eta_{\mathrm{cpc}} = \frac{\eta_{\max}}{1 + e^{-k(d_{\mathrm{p}} - d_{\mathrm{p},0})}}, \tag{2.10}$$

where $\eta_{\max} = 0.841$, $k = 6.30\ \mathrm{nm}^{-1}$, and $d_{\mathrm{p},0} = 1.54$ nm, based on the calibration results.

In addition to detection efficiency, the delay in CPC response also complicates the transfer function of the system. When the classifier is operated at scanning mode, the slow response of the CPC may introduce a smearing effect and broaden the particle transfer functions (Russell et al., 1995; Collins et al., 2002). To explore the extent of this effect, the nSEMS was run with different voltage ramp times (10 s - 1400 s). At long voltage ramp times, e.g., at 1400 s, the nSEMS can be treated as operating in a quasi-static mode, where the CPC response time has no impact on the transfer functions. Figure 2.7 shows the experimentally determined particle transfer functions of the nSEMS at different t_{ramp}, for $d_{\mathrm{p}} = 18$ nm particles. The results indicate that the smearing effect is small when t_{ramp} is longer than 30 s ($\tau_{\mathrm{s}} \geq 4.83$ s). To account for this effect, the response of the two-stage CPC can be modeled as a plug flow reactor (PFR) in series with a continuous stirred-tank reactor (CSTR) to estimate its particle residence time distribution, $E_{\mathrm{cp}}(t)$ (Russell et al., 1995; Mai et al., 2018):

$$\begin{aligned} E_{\mathrm{cp}}(t) &= E_{\mathrm{p}}(t) \star E_{\mathrm{c}}(t) \\ &= \int_{-\infty}^{\infty} E_{\mathrm{c}}(t') E_{\mathrm{p}}(t - t') \mathrm{d}t' \\ &= \begin{cases} 0, & t < \tau_{\mathrm{p}} \\ \frac{1}{\tau_{\mathrm{c}}} e^{-\frac{t - \tau_{\mathrm{p}}}{\tau_{\mathrm{c}}}}, & t \geq \tau_{\mathrm{p}}, \end{cases} \end{aligned} \tag{2.11}$$

where τ_{p} and τ_{c} are the mean residence time of the PFR and the CSTR, respectively, and $\star$ is the symbol for the convolution of two functions (Bracewell and Bracewell, 1986). The transfer function of the integrated nSEMS system, $\Omega_{\mathrm{nSEMS}}(Z_{\mathrm{p}}, \beta, \delta, t)$, can be written as

$$\Omega_{\mathrm{nSEMS}}(Z_{\mathrm{p}}, \beta, \delta, t) = \Omega_{\mathrm{ROMIAC}}(Z_{\mathrm{p}}, \beta, \delta, t) \star E_{\mathrm{cp}}(t) \tag{2.12}$$

The residence time distribution is computed by deconvoluting the quasi-static nSEMS transfer function measured with $t_{\mathrm{ramp}} = 1400$ s, from that measured with $t_{\mathrm{ramp}} = 50$ s. The resulting characteristic times for the CPC residence time distribution were $\tau_{\mathrm{c}} = 0.20$ s and $\tau_{\mathrm{p}} = 0.70$ s (2.13). The dashed lines in Figure 2.3 show

the convoluted nSEMS transfer function, $\Omega_{\mathrm{nSEMS}}(Z_{\mathrm{p}}, \beta, \delta, t)$, combining the CPC residence time distribution in addition to the scanning ROMIAC simulation.

Derivation of the integrated instrument transfer function and data inversion

Data inversion is required to retrieve particle size distribution of the source particles, N, from the particle counts measured by the CPC, $\mathbf{R}_{\mathrm{nSEMS}}$, given that:

$$\mathbf{R}_{\mathrm{nSEMS}} = \mathbf{A}_{\mathrm{nSEMS}} N \tag{2.13}$$

where $\mathbf{A}_{\mathrm{nSEMS}}$ is often referred to as the inversion kernel for the instrument. The time-series instrument response can be written as $\mathbf{R}_{\mathrm{nSEMS}} = [R_{\mathrm{nSEMS},1}, R_{\mathrm{nSEMS},2}, \cdots, R_{\mathrm{nSEMS},I}]^{\mathrm{T}}$. With the default nSEMS voltage ramp time, $t_{\mathrm{ramp}} = 50$ s, and the CPC data recording frequency, $t_{\mathrm{c}} = 0.2$ s, the vector length for one complete scan is $I = 250$. The particle number counts recorded by the CPC in the i^{th} time bin, $R_{\mathrm{nSEMS},i}$, can be represented as the integral of the total number of particles transmitted over the time interval $(i-1)t_{\mathrm{c}} \leq t < it_{\mathrm{c}}$:

$$\begin{aligned} R_{\mathrm{nSEMS},i} &= Q_{\mathrm{a}} \int_{(i-1)t_{\mathrm{c}}}^{it_{\mathrm{c}}} \int_{-\infty}^{\infty} N(d_{\mathrm{p}}) \sum_{\phi} p_{\mathrm{charge}}(d_{\mathrm{p}}, \phi)\, \eta_{\mathrm{CPC}}(d_{\mathrm{p}}, \phi) \\ &\times \Omega_{\mathrm{nSEMS}}(Z_{\mathrm{p}}(d_{\mathrm{p}}, \phi), \beta, \delta, t)\, \mathrm{d}d_{\mathrm{p}}\, \mathrm{d}t \end{aligned} \tag{2.14}$$

The particle charging probability from the soft x-ray charge conditioner, $p_{\mathrm{charge}}(d_{\mathrm{p}}, \phi)$, was assumed to be that of the Wiedensohler (1988) approximation, and is computed separately for scans of negative and positive polarity. In order to obtain the instrument transfer function, $\Omega_{\mathrm{nSEMS}}(Z_{\mathrm{p}}, \beta, \delta, t)$, for each time bin, the simulated ROMIAC transfer functions were first fitted as Gaussian functions:

$$\Omega_{\mathrm{ROMIAC}}(Z_{\mathrm{p}}, \beta, \delta, t) = a \exp\left(-\frac{(t-b)^2}{2c^2}\right) \tag{2.15}$$

The three fitting parameters, a, b, and c, were then interpolated over the entire time vector with 250 bins. By substituting the interpolated parameters back into Eq.(2.15), a ROMIAC transfer function, $\Omega_{\mathrm{ROMIAC}}(Z_{\mathrm{p}}, \beta, \delta, t)$, was generated for each time bin. The fitted transfer functions were adjusted by the empirically determined mobility correction factor, f_z. The nSEMS transfer function for each time bin, $\Omega_{\mathrm{nSEMS}}(Z_{\mathrm{p}}, \beta, \delta, t)$, was then computed by the convolution of the ROMIAC transfer function and the CPC residence time distribution of Eq.(2.12). Similar to the CPC instrument response, the inversion kernel matrix can also be decomposed into a time-series form, $\mathbf{A}_{\mathrm{nSEMS}} = [A_{\mathrm{nSEMS},1}, A_{\mathrm{nSEMS},2}, \cdots, A_{\mathrm{nSEMS},I}]^{\mathrm{T}}$, where

$$\begin{aligned} A_{\mathrm{nSEMS},i} &= Q_{\mathrm{a}}\, p_{\mathrm{charge}}(d_{\mathrm{p}}, \phi)\, \eta_{\mathrm{CPC}}(d_{\mathrm{p}}, \phi)\, \mathrm{d}\log d_{\mathrm{p}}\, t_{\mathrm{c}} \\ &\times \Omega_{\mathrm{nSEMS},i}(Z_{\mathrm{p}}(d_{\mathrm{p}}, \phi), \beta, \delta, t) \end{aligned} \tag{2.16}$$

where $\mathrm{d}\log d_\mathrm{p}$ is the logarithmically spaced size-bin with total length I. We then applied a totally nonnegative least squares (TNNLS) algorithm to retrieve the sample particle size distribution from the inversion kernel and the particle number concentrations detected by the CPC, i.e., solving for $N = \mathbf{A}_\mathrm{nSEMS}^{-1}\mathbf{R}_\mathrm{nSEMS}$ (Merritt and Y. Zhang, 2005).

Calibration results

Figure 2.8 shows the nSEMS scanning response with size-selected particles of different mobility-equivalent diameters using the TDMA setup shown in Figure 2.4b ($d_\mathrm{p} \leq 10.70$ nm) and Figure 2.4c ($d_\mathrm{p} \geq 12.00$ nm) with the default operating parameters listed in Table 2.1. The particles fed into the nSEMS using the TDMA set-up were not monodisperse, which may have led to peak broadening and particle losses. In order to compare the experimental result with simulation, we deconvoluted the CPC residence time distribution and the static classifier transfer function from the instrument response as shown in Figure 2.8 (**Stolzenburg:2008aa**):

$$\Omega_\mathrm{ROMIAC}(\tilde{Z}_\mathrm{p},\beta,\delta,t) = \begin{cases} \frac{R_{\mathrm{nSEMS},i}}{E_\mathrm{cp}\Omega_\mathrm{ROMIAC}(\tilde{Z}_\mathrm{p},\beta,\delta,\sigma)}, & d_\mathrm{p} < 12\mathrm{nm} \\ \frac{R_{\mathrm{nSEMS},i}}{E_\mathrm{cp}\Omega_\mathrm{DMA}(\tilde{Z}_\mathrm{p},\beta,\delta,\sigma)}, & d_\mathrm{p} \geq 12\mathrm{nm} \end{cases} \tag{2.17}$$

where the dimensionless mobility, $\tilde{Z}_\mathrm{p}$, is defined as the ratio of input particle electrical mobility and the ideal mobility, $Z^*_\mathrm{p,ideal}$, as defined in Eq. 2.6:

$$\tilde{Z}_\mathrm{p} = \frac{Z_\mathrm{p}}{Z^*_\mathrm{p,ideal}} \tag{2.18}$$

and $\Omega_\mathrm{ROMIAC}(\tilde{Z}_\mathrm{p},\beta,\delta,\tilde{\sigma})$ and $\Omega_\mathrm{ROMIAC}(\tilde{Z}_\mathrm{p},\beta,\delta,\tilde{\sigma})$ are the diffusing transfer function for the ROMIAC and long-column DMA operated at static mode, respectively:

$$\begin{aligned} \Omega(\tilde{Z}_\mathrm{p},\beta,\delta) \;=\; & \frac{\tilde{\sigma}}{\sqrt{2}\beta(1-\delta)}\left[\epsilon\left(\frac{\tilde{Z}_\mathrm{p}-(1+\beta)}{\sqrt{2}\tilde{\sigma}}\right)+\epsilon\left(\frac{\tilde{Z}_\mathrm{p}-(1-\beta)}{\sqrt{2}\tilde{\sigma}}\right)\right. \\ & \left. -\;\epsilon\left(\frac{\tilde{Z}_\mathrm{p}-(1+\beta\delta)}{\sqrt{2}\tilde{\sigma}}\right)-\epsilon\left(\frac{\tilde{Z}_\mathrm{p}-(1-\beta\delta)}{\sqrt{2}\tilde{\sigma}}\right)\right] \end{aligned} \tag{2.19}$$

where ϵ is a function of $\mathrm{erf}(x)$, the error function:

$$\epsilon(x) = x\,\mathrm{erf}(x) + \frac{\exp\left(-x^2\right)}{\sqrt{\pi}} \tag{2.20}$$

The dimensionless diffusion factor, $\tilde{\sigma}$, is defined as:

$$\tilde{\sigma}^2 = \frac{G_\mathrm{class}}{\mathrm{Pe}_\mathrm{mig}}\tilde{Z}_\mathrm{p} \tag{2.21}$$

At ambient temperature, the migration Péclet number for singly-charged particles can be approximated as a function of the static voltage:

$$\mathrm{Pe}_{\mathrm{mig}} = \frac{\phi e V}{kT} \approx \frac{V}{0.0255[V]} \tag{2.22}$$

The dimensionless geometry factor for classifiers, G_{class}, is estimated to be $G_{\mathrm{LDMA}} = 2.55$ for the TSI 3081 LDMA at $\mathcal{R}_{\mathrm{nd,\ DMA}} \approx 12$, and for the ROMIAC at $\mathcal{R}_{\mathrm{nd,\ ROMIAC}} \approx 10$, can be computed as:

$$G = \begin{cases} \frac{8}{3}, & \xi = 0 \\ \dfrac{4\left\{\frac{4}{15}\left[\left(1-|\xi|^{5/2}\right)-(1-|\xi|)^{5/2}\right]+\frac{1}{3}\left(\frac{\xi}{\alpha}\right)^2\left[\left(1-|\xi|^{3/2}\right)-(1-|\xi|)^{3/2}\right]\right\}}{|\xi|(1-|\xi|)}, & 0 < |\xi| < 1 \\ 2\left[\frac{4}{3}+\left(\frac{1}{\alpha}\right)^2\right], & |\xi| = 1 \end{cases} \tag{2.23}$$

where $\xi = \beta^{-1}(\tilde{\mathrm{Z}}_{\mathrm{p}}-1))$ and $\alpha = L/b = 0.015$ m$/0.01$ m $= 1.5$ for the ROMIAC. The real resolution of the scanning ROMIAC can then be computed using the full width at half maximum of the transfer function, $\Omega_{\mathrm{ROMIAC}}(\tilde{\mathrm{Z}}_{\mathrm{p}}, \beta, \delta, t)$, (*Flagan*, 1999; *Flagan*, 2004):

$$\mathcal{R} = \frac{Z_{\mathrm{p}}^*}{\Delta Z_{\mathrm{p}}} \tag{2.24}$$

The transmission efficiency can be calculated as the area under the transfer function normalized by the area of an ideal transfer function, which in non-dimensionless form is equivalent to the flow factor, β:

$$\eta = \frac{1}{\beta}\int \Omega_{\mathrm{ROMIAC}}(\tilde{\mathrm{Z}}_{\mathrm{p}}, \beta, \delta, t)\ \mathrm{d}\tilde{Z}_{\mathrm{p}} = \frac{1}{\beta}\int \frac{N_{\mathrm{out}}}{N_{\mathrm{in}}}\ \mathrm{d}\tilde{Z}_{\mathrm{p}} \tag{2.25}$$

Figure 2.9 shows the comparison of ROMIAC resolution and efficiency between experiment, COMSOL simulation, and the theoretical limit calculated for the DMA and the OMAC operated in static mode (Flagan, 2004). The overall performance of the nSEMS shows convincing agreement with the finite-element simulation results in Figure 2.3, which proves the feasibility of coupling laboratory calibrations with numerical simulation to predict the instrument response of a SEMS system. Compared to the simulation and theoretical calculation, the effect of diffusional degradation at low voltages remains minimal for the scanning ROMIAC system compared to other conventional nano-SMPS systems, as previously predicted for the static OMAC (Flagan, 2004; Downard et al., 2011). Figure 2.10 shows the nSEMS peak voltage (V^*) as a function of particle mobility when operated at a cross-flow rate of $Q_c = 12$ L/min. In addition to the calibration results using the hotwire or atomized particle sources, it also includes the signature peak of tetra-heptyl ammonium

bromide (THAB) ions (see Figure 2.4a for setup). Particle mobilities are calculated using Eq.(2.1) at given diameters assuming that the particles are singly charged. The experimentally determined voltages at the transfer-function peaks are in close agreement with those predicted by the COMSOL simulation in Figure 2.3. From the laboratory characterization results, the method of using empirical data to adjust the simulated particle transmission has proven to be an efficient and effective way to derive SEMS or SMPS system transfer function. In addition, the nSEMS, as the first system that employs an opposed-migration classifier with continuously varying voltage, has also demonstrated the great potential of scanning OMAC systems for providing fast and accurate particle size information in the low-nanometer regime without significant diffusional degradation.

2.4 Application to Particle Size Distribution Measurement

Atmospheric new particle formation and its subsequent growth have a great impact on aerosol number concentrations and the Earth's total energy budget. In order to better understand the climate significance of NPF, much research has attempted to study the mechanisms of nucleation and the growth rates of nanoparticles. For example, the CLOUD experiments at CERN have extensively probed the roles of sulfuric acid, ammonia, cosmic rays, and other atmospheric components on nucleation (Kirkby et al., 2011; Kirkby et al., 2016). To determine the particle formation and growth rates from the atmospheric chamber experiments, the particle size distribution needs to be measured at high resolving power and with a short duty cycle. In addition to being able to capture the transient aerosol dynamics during NPF events, since most of the nucleation occurs in clean atmospheric conditions, the instrument must be capable of taking measurements at relatively low particle concentrations. The nSEMS was used for particle sizing in both the CLOUD 13 and the CLOUD 14 campaigns. Figure 2.11 shows a particle size distribution measured with nSEMS during an ion-induced nucleation event that simulated atmospheric nucleation and nanoparticle growth in urban environment in CLOUD 13. The experiment was conducted in the presence of sulfuric acid, nitric acid, and ammonia at -10 ^{o}C and 60 % RH. When particles reached $d_{\mathrm{p}} \approx 4.6$ nm, nitric acid and ammonia started condensing rapidly onto the particles, resulting in a growth rate of 40 nm/h. This extremely fast growth from nitric acid and ammonia co-condensation can generally persist for only a few minutes, and activate only the largest of the initial small nuclei, before depleting the nitric acid supersaturation and turning off additional nucleation. Those few nuclei that activate are often present only in

low concentrations (M. Wang et al., 2020). Consequently, the other conventional particle sizing instruments that are connected to the CLOUD chamber were not able to fully capture this rapid growth event; the concentrations were too low to be detected by the nano-SMPS (Tröstl et al., 2015), and the size of the particles evolved so fast that a higher size resolution was required than could be attained by the DMA-train that measures six sizes in parallel with separate static DMAs (D. Stolzenburg et al., 2017). In the region where multiple instruments can capture the aerosol dynamics, the intercomparison between the results of different instruments showed reasonably good agreement. Combining these measurements also provided detailed particle growth information in rapidly evolving new particle formation events that the other instruments could follow M. Wang et al., 2020. In addition to enabling high resolving power measurements of size distributions during rapid particle growth events, the nSEMS also provides valuable information on natural ion and charged particle concentrations in the chamber when operated with the charge conditioner switched off. The ability to measure the concentrations of positive and negative nanoparticles separately facilitates study of the role of ions in atmospheric nucleation and growth.

The design and performance of a novel nanoparticle size-classifying instrument, the nSEMS, has been evaluated. The concept of OMAC was first proposed in order to overcome the diffusional degradation at lower voltages of the DMA (Flagan, 2004). The radial form of the OMAC, the ROMIAC, was then designed to classify nanoparticles in the low-nanometer regime with high resolving power in static mode (Mui et al., 2013; Mui et al., 2017). According to the ideal model of OMAC, particles are transmitted through the classification region parallel to the porous electrodes, and voltage variations would lead to excessive particle losses. A key feature of the ROMIAC design was to both introduce the sample and to extract the classified ions or particles on the ground-electrode side of the classifier. The resulting trajectories, which can be seen in COMSOL Multiphysics^{TM} simulations shown in Figure 2.12, reduce losses associated with voltage scanning to acceptable levels, thereby enabling measurement acceleration by voltage scanning and operating as a SEMS. The ability to classify particles at low voltage with minimal diffusional degradation of the transfer function, combined with a fast response CPC that minimizes residence time distribution related to the smearing effect, made it possible for the ROMIAC to be operated with fast exponential voltage ramping, greatly accelerating the measurement over that of static mode operation. The nSEMS system, which uses a soft x-ray charge conditioner, a scanning ROMIAC as classifier, and a two-

stage CPC as particle detector, can provide highly resolved particle size distribution measurements, in the 1.5 - 25 nm size range in one minute or less (we did not push the bound on the scan rate in the initial application of the nSEMS at CLOUD). The integrated instrument transfer function, which can reproduce how particles are transmitted inside the nSEMS within 10% uncertainty, has been derived by combining COMSOL finite-element analysis with empirical adjustments. The particle size distributions measured by the nSEMS using the described data inversion method agrees reasonably well with other instruments (Tröstl et al., 2015; D. Stolzenburg et al., 2017) used in the CLOUD experiment (M. Wang et al., 2020). However, there remain uncertainties associated with particle charge distribution. The dual-polarity scanning feature of the nSEMS makes it possible to observe the charge effects on the evolution of the size distribution as particles nucleate and grow. Its dual polarity capability should also facilitate characterization of the particle charge distribution in the low nanometer regime, thereby improving the instrumental transfer function and data inversion. Overall, this instrument is able to provide robust particle sizing information in the sub-25 nm region, and is extremely powerful in examining atmospheric nucleation and the subsequent growth of nanoparticles.

Acknowledgement

The authors would like to thank the CLOUD experiment for providing the facility for instrument testing and operation. We gratefully acknowledge a generous gift from Christine and Dwight Landis to improve the data acquisition system of the instrument. This work was supported by the National Science Foundation under Grants No. AGS 1602086 and AGS 1801329.

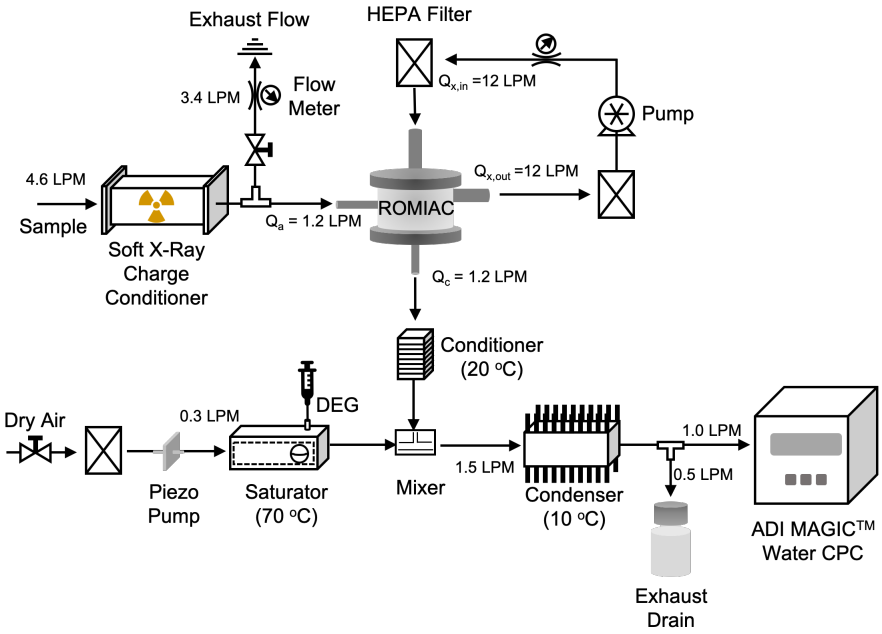

Figure 2.1: Schematic of the nSEMS main components; a soft x-ray charge conditioner, a radial opposed-migration ion and aerosol classifier (ROMIAC), and a two-stage condensation particle counter (CPC). Core-sampling of the input sample flow is employed to minimize particle diffusional losses in the charge conditioner. The ROMIAC is operated on exponentially increasing voltage ramps between 20 V and 10,000 V of both positive and negative polarity, at 1.2 L/min and 12 L/min aerosol and cross-flows (Table 2.1). After exiting the classifier, monodisperse aerosol particles are mixed with 0.3 L/min diethylene glycol (DEG) vapor in the first stage of the CPC. This fast-mixing stage allows nanoparticles to grow through rapid vapor condensation before they enter the second, "booster" CPC stage, a modified Aerosol Dynamics Inc. (ADI) MAGIC^{TM} water CPC operated at a flow rate of 1.0 L/min, where particles grow further and are optically detected.

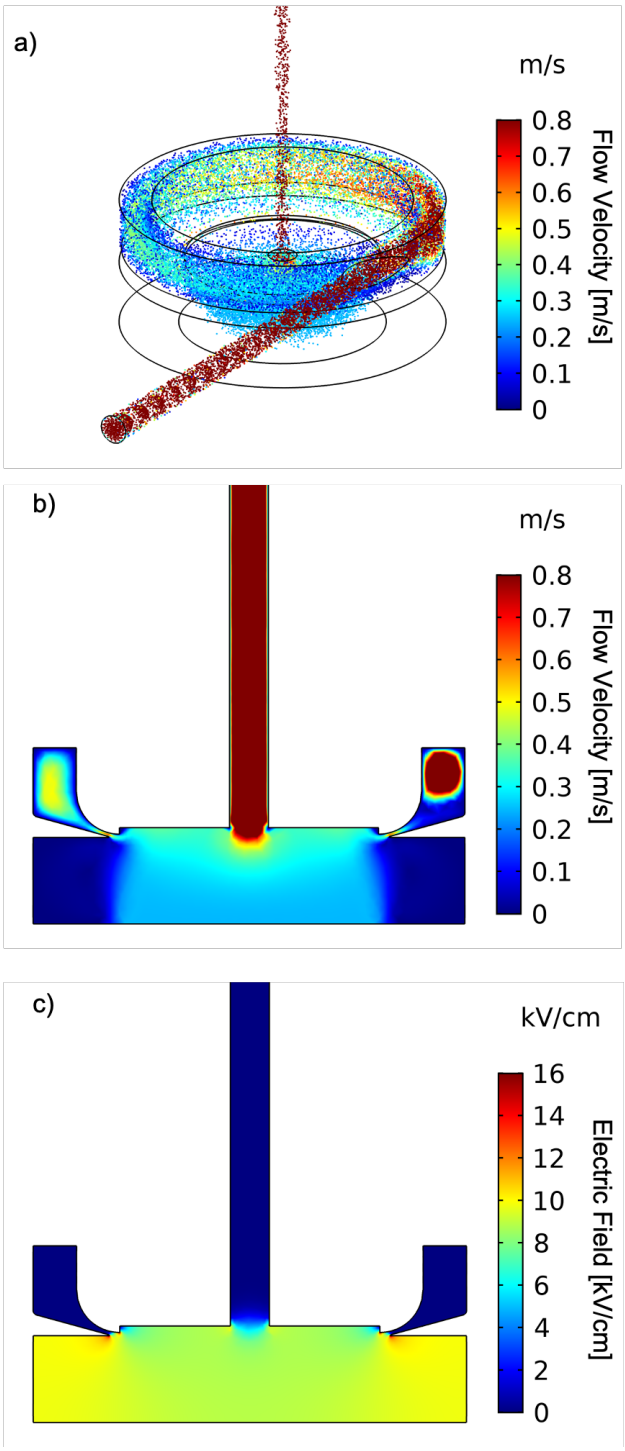

Figure 2.2: Example of finite-element simulations of the scanning ROMIAC at Q_a = 1.2 L/min, Q_c = 12 L/min, d_p = 4.0 nm. (a) Particle trajectories over a 50 s upscan at $t \approx 25$ s. Cross-section view of (b) the flow velocity, and (c) electric field distribution. The magnitude of the electric field corresponds to the maximum, 10 kV, electric potential.

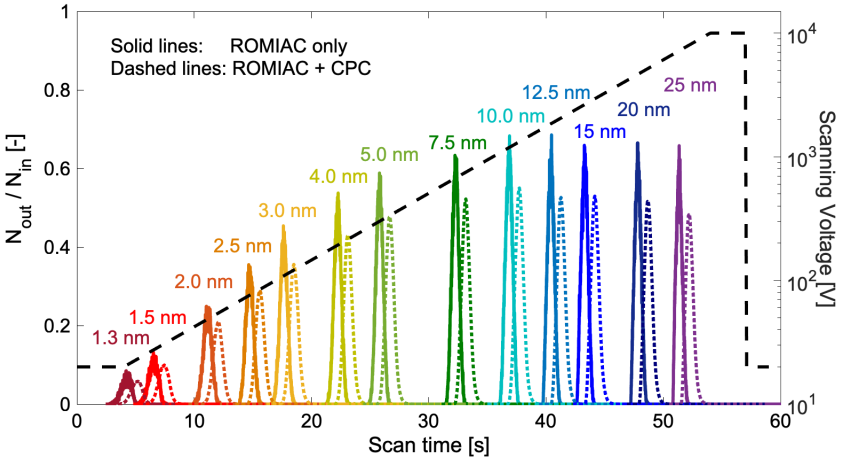

Figure 2.3: Simulated transfer function of the scanning ROMIAC with monodisperse input particles in the 1.3 – 25 nm size range. The transfer function is calculated as the ratio of particle number at the exit and the entrance of ROMIAC over a voltage scan (dashed black line) with t_{ramp} = 50 s. Solid lines show the transfer function of the classifier (scanning ROMIAC) only; dashed lines show the simulated ROMIAC transfer function coupled with the CPC residence time distribution (see Eq. (2.12)). The integrated transfer function peaks (dashed lines) are used to compute the inversion kernel for nSEMS data inversion.

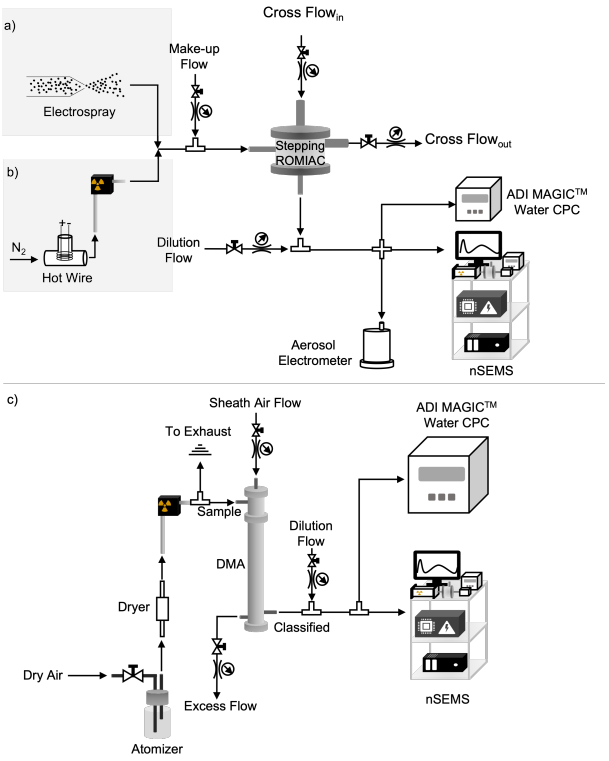

Figure 2.4: The experimental setup used for the nSEMS calibration and characterization in different particle size ranges. (a) < 3 nm size range: tetra-alkyl ammonium ions produced by an electrospray were classified using static ROMIAC as classifier ($\mathcal{R}_{\text{nom,nd}} \approx 10$), and an aerosol electrometer as a reference for the upstream particle number. The electrospray was operated at 3000 V and 25 cm H_2O pressure. The tetra-alkyl ammonium solutions were prepared with 10 - 20 mg salt in 1.5 ml methanol. (b) 1.5 – 20 nm size range: A heated Nichrome wire (hotwire) was employed as aerosol source, a static ROMIAC as classifier ($\mathcal{R}_{\text{nom,nd}} \approx 10$), and both an aerosol electrometer and ADI MAGIC$^{\text{TM}}$ water CPC as upstream particle counters. The hotwire was operated in the range of 5.0 - 7.0 V and 4.5 - 6.5 A. (c) 12.0 – 26.5 nm size range: atomized sodium chloride was employed as aerosol source, a cylindrical differential mobility analyzer (DMA) as classifier ($Q_{\text{a}} = 0.5L/min$, $Q_{\text{sh}} = 5.8L/min$, $\mathcal{R}_{\text{nom,nd}} \approx 12$), and an ADI MAGIC$^{\text{TM}}$ water CPC as upstream particle counter. Both b) and c) follow a TDMA calibration setup (Rader and McMurry, 1986), which uses a classifier at a constant voltage to select particles within a narrow distribution of sizes.

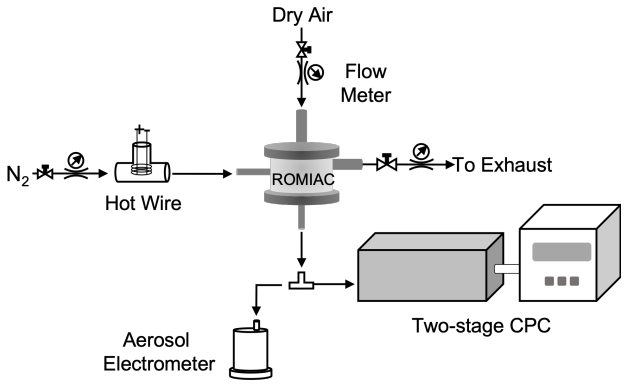

Figure 2.5: Experimental setup used to characterize the two-stage CPC detection efficiency. A heated Nichrome wire (hotwire) aerosol generator was used to provide aerosol samples. The ROMIAC was operated at static mode to provide stable, monodisperse aerosol particles for both the two-stage CPC and the aerosol electrometer. The ROMIAC aerosol and cross-flow rates were Q_a = 2.5 L/min and Q_c = 35.5 L/min. The electrometer was pre-calibrated against a TSI 3760A butanol-based CPC and an ADI MAGIC^{TM} water-based CPC.

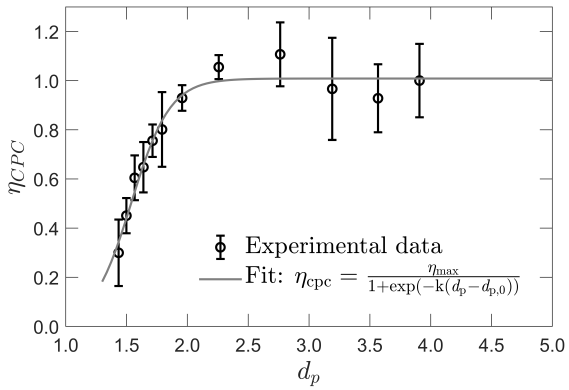

Figure 2.6: Detection efficiency of the two-stage CPC as a function of $d_{\rm p}$, the mobility-equivalent particle diameter. The efficiency is corrected for the dilution due to the vapor flow. The size-dependent detection efficiency is fitted to a logistic function with fitting parameters $\eta_{\rm max}$ = 0.841, k = 6.30 nm^{-1}, and $d_{\rm p,0}$ = 1.54 nm. The fit is used to approximate the CPC detection efficiency, $\eta_{\rm cpc}$, in the data inversion.

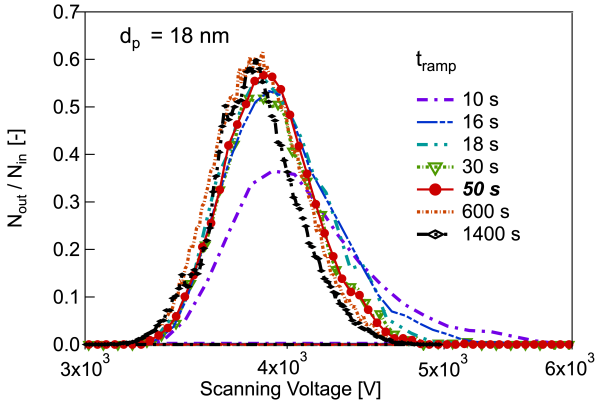

Figure 2.7: Effect of voltage ramp time, t_{ramp}, on the nSEMS scanning transfer function with $d_{\text{p}} = 18$ nm input particles. The nSEMS voltage is increased exponentially from 20 V to 10 kV, over ramp times within 10 – 1400 s, including the default $t_{\text{ramp}} = 50$ s. CPC smearing of the transfer function increases with decreasing t_{ramp}, and becomes very pronounced at $t_{\text{ramp}} < 20$ s.

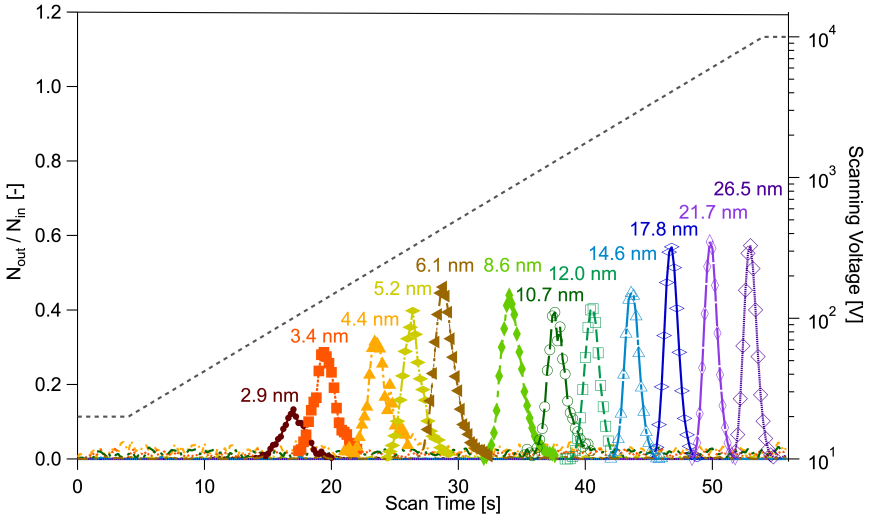

Figure 2.8: Experimental calibration of the nSEMS using the TDMA setup shown in Figure 2.4. Particles entering the nSEMS were classified as described; the reported mobility-equivalent diameters were calculated based on the upstream classifier operating parameters. The nSEMS was operated at the default parameters listed in Table 2.1, with $t_{\text{ramp}} = 50$ s. The ratio of downstream to upstream particle counts of the nSEMS is shown as a function of time over the voltage scan, with input particles in the 2.9 – 26.5 nm range. The applied voltage is indicated by the dashed gray line. Only a fraction of the sizes used in the calibration are shown here for clarity; results from the complete size calibration summary are presented in Figure 2.10.

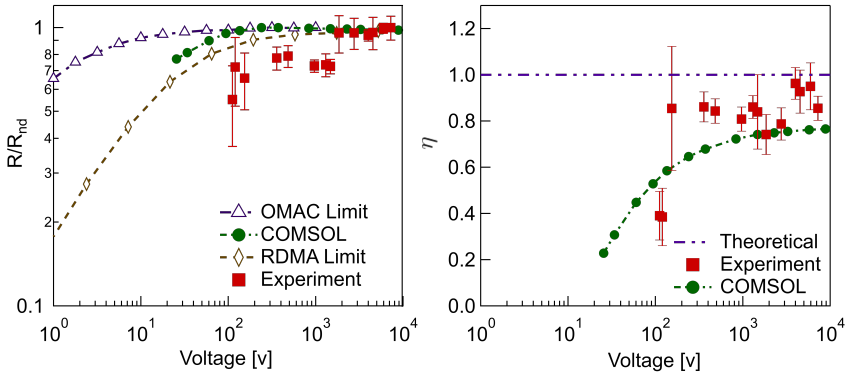

Figure 2.9: Comparison between experimental, simulated, and theoretical transfer functions. (a) Effect of operating voltage on classifier resolution, calculated as the actual resolution based on the full width at half maximum (FWHM) (Eq. (2.24)) over $\mathcal{R}_{\text{nd}}$, the resolution at the nondiffusive regime (>5000V). (b) Particle transmission efficiency as a function of operating voltage. Transmission efficiency, η, is calculated as the ratio of the actual over the ideal area below the transfer function peak. The error bars represent one standard deviation of uncertainty from multiple experiments at one size.

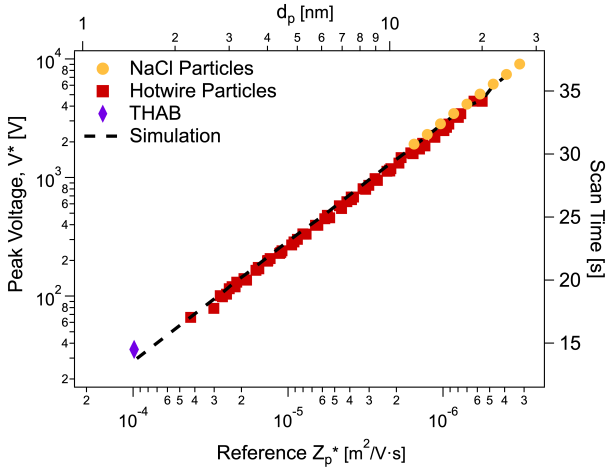

Figure 2.10: nSEMS voltage at the peak transmission (V^*) as a function of the input reference particle mobility, Z_{p}^*. Symbols represent experimental results with tetra-heptyl ammonium bromide (THAB), hotwire, and atomized NaCl particles produced using the setups shown in Figure 2.4. The black dotted line demonstrates the voltage at peak transmission predicted by the finite-element simulations. The top axis shows the corresponding particle diameter, d_{p}, at a given mobility, Z_{p}^*, as defined in Eq.(2.1); the right axis shows the corresponding time in the scan.

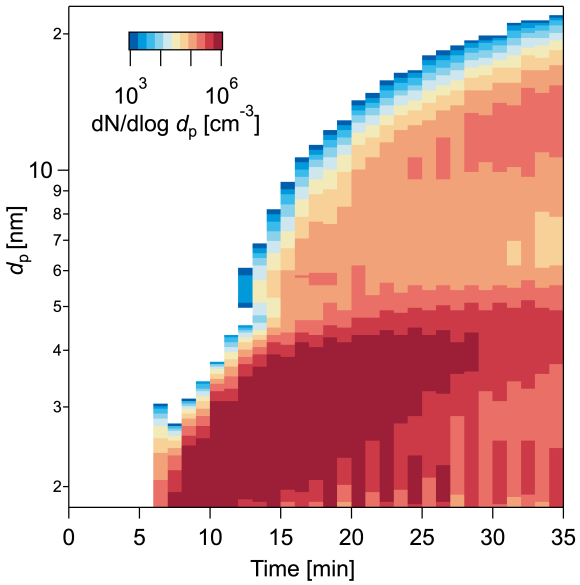

Figure 2.11: Particle size distribution measured by the nSEMS during a nucleation and growth event in the CLOUD 13 campaign with anthropogenic trace gases. The experiment was conducted at -10^{o}C and 60% RH, with 24 pptv HNO_3, 2131 pptv NH_3, 0.46 pptv H_2SO_4, and 0.28 pptv highly oxygenated organic molecules (HOM). The nSEMS high-voltage polarity was switched between scans to probe both positively and negatively charged particles from the soft x-ray charge conditioner. A clear bimodal size distribution was observed by the nSEMS due to the rapid co-condensation of nitric acid and ammonia (M. Wang et al., 2020). The activation diameter, d_{act}, for nitric acid condensation is around 4.6 nm.

Table 2.1: Default nSEMS operating parameters, optimized for measurements of NPF events and nanoparticle growth. These settings enable particle size distribution measurements in the range of 1.5 - 25 nm, with a duty cycle of 1 min and a size classification resolution of $\mathcal{R}_{\text{nom,nd}}$ = 10.

Parameter	Notation	Value
Instrument total sampling rate (L/min)	Q_{s}	4.60[a]
ROMIAC polydisperse flow rate (L/min)	Q_{a}	1.20
ROMIAC monodisperse flow rate (L/min)	Q_{c}	1.20
ROMIAC incoming cross-flow flow rate (L/min)	$Q_{\text{x, in}}$	12.0
ROMIAC outgoing cross-flow flow rate (L/min)	$Q_{\text{x, out}}$	12.0
DEG feeding rate (L/min)	Q_{DEG}	0.30
CPC sampling rate (L/min)	Q_{CPC}	1.00
Low electrode voltage (V)	V_{low}	20.0
High electrode voltage (V)	V_{high}	10,000
CPC sample conditioner temperature (^{o}C)	T_{co}	20[b]
CPC DEG saturator temperature (^{o}C)	T_{sat}	70
CPC sample condenser temperature (^{o}C)	T_{cond}	10
Voltage ramp time (s)	t_{ramp}	50
Holding time at V_{low} (s)	t_{low}	4
Holding time at V_{high} (s)	t_{high}	2
Scan duty cycle (s)	t_{total}	60
CPC data recording frequency (s)	t_{c}	0.20

[a] All flow rate measurements have an uncertainty of ±2%.

[b] All temperature measurements have an uncertainty of ±0.1°C.

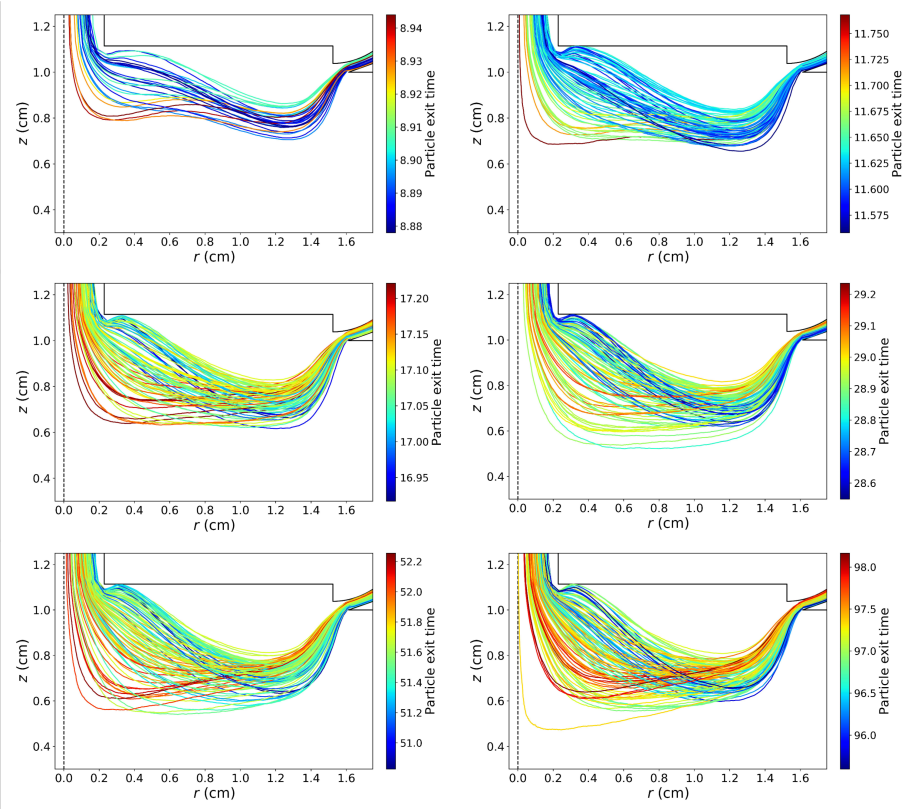

Figure 2.12: Finite-element simulations of particle trajectories at $d_{\mathrm{p}} = 20.8$ nm with different ramp time, $t_{\mathrm{ramp}} = 3$, 6, 12, 25, 50, 100 s, from top left to bottom right, respectively. Particles were assumed to be nondiffusive. The simulation was conducted with the flow setting $Q_{\mathrm{x}}/Q_{\mathrm{a}} = 10$ LPM/1 LPM.The color bar indicates the time at which the particles leave the classifying ROMIAC.

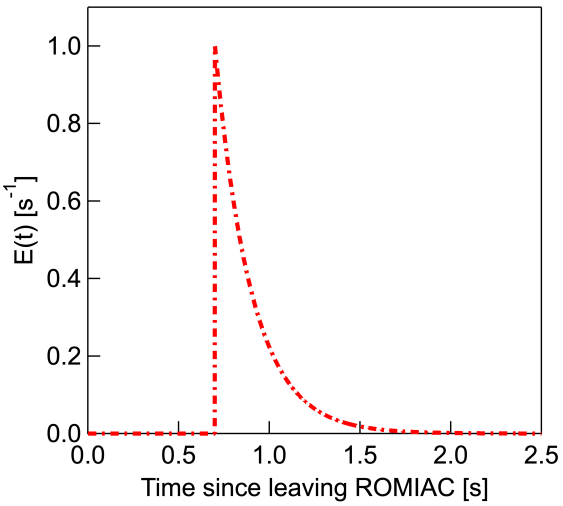

Figure 2.13: CPC residence time distribution fitting using PFR-CSTR in series. The residence time distribution in the CPC can be computed by deconvoluting the quasi-static nSEMS transfer function measured with t_{ramp} = 1400 s, from that measured with t_{ramp} = 50 s. CPC was modeled as a PFR in series with a CSTR and the mean residence time of the PFR, τ_{p}, 0.7 s and that of the CSTR, τ_{c}, is 0.2 s

References

S. Amanatidis et al. (Feb. 2020). "The Spider DMA: A miniature radial differential mobility analyzer". In: *Aerosol Science and Technology* 54.2, pp. 175–189. ISSN: 0278-6826. DOI: 10.1080/02786826.2019.1626974. (Visited on 05/07/2020).

B. Bonn and G. K. Moortgat (2003). "Sesquiterpene ozonolysis: Origin of atmospheric new particle formation from biogenic hydrocarbons". en. In: *Geophysical Research Letters* 30.11. ISSN: 1944-8007. DOI: 10.1029/2003GL017000. (Visited on 05/06/2020).

R. N. Bracewell and R. N. Bracewell (1986). *The Fourier transform and its applications*. Vol. 31999. McGraw-Hill New York.

L. M. Brown et al. (2000). "Respiratory dose of inhaled ultrafine particles in healthy adults". In: *Philosophical Transactions of the Royal Society of London. Series A: Mathematical, Physical and Engineering Sciences* 358.1775, pp. 2693–2705. DOI: 10.1098/rsta.2000.0678.

N. A. Brunelli et al. (Jan. 2009). "Radial Differential Mobility Analyzer for One Nanometer Particle Classification". In: *Aerosol Science and Technology* 43.1, pp. 53–59. ISSN: 0278-6826. DOI: 10.1080/02786820802464302.

D. .-.-R. Chen et al. (June 1998). "Design and evaluation of a nanometer aerosol differential mobility analyzer (Nano-DMA)". en. In: *Journal of Aerosol Science* 29.5, pp. 497–509. ISSN: 0021-8502. DOI: 10.1016/S0021-8502(97)10018-0. (Visited on 05/06/2020).

X. Chen et al. (Aug. 2018). "Stationary characteristics in bipolar diffusion charging of aerosols: Improving the performance of electrical mobility size spectrometers". In: *Aerosol Science and Technology* 52.8, pp. 809–813. ISSN: 0278-6826. DOI: 10.1080/02786826.2018.1479058. (Visited on 11/12/2018).

D. R. Collins et al. (Jan. 2002). "Improved Inversion of Scanning DMA Data". In: *Aerosol Science and Technology* 36.1, pp. 1–9. ISSN: 0278-6826. DOI: 10.1080/027868202753339032.

D. R. Collins et al. (Aug. 2004). "The Scanning DMA Transfer Function". In: *Aerosol Science and Technology* 38.8, pp. 833–850. ISSN: 0278-6826. DOI: 10.1080/027868290503082. (Visited on 05/09/2020).

M. Dall'Osto et al. (June 2017). "Arctic sea ice melt leads to atmospheric new particle formation". en. In: *Scientific Reports* 7.1, pp. 1–10. ISSN: 2045-2322. DOI: 10.1038/s41598-017-03328-1. (Visited on 05/06/2020).

A. J. Downard et al. (Apr. 2011). "An Asymptotic Analysis of Differential Electrical Mobility Classifiers". In: *Aerosol Science and Technology* 45.6, pp. 727–739. ISSN: 0278-6826. DOI: 10.1080/02786826.2011.558136.

P. Dubey and S. Dhaniyala (Aug. 2011). “A New Approach to Calculate Diffusional Transfer Functions of Scanning DMAs”. In: *Aerosol Science and Technology* 45.8, pp. 1031–1040. ISSN: 0278-6826. DOI: 10.1080/02786826.2011.579644. (Visited on 05/09/2020).

M. J. Dunn et al. (2004). “Measurements of Mexico City nanoparticle size distributions: Observations of new particle formation and growth”. en. In: *Geophysical Research Letters* 31.10. ISSN: 1944-8007. DOI: 10.1029/2004GL019483. (Visited on 05/06/2020).

H. J. Fissan et al. (Jan. 1983). “Determination of particle size distributions by means of an electrostatic classifier”. en. In: *Journal of Aerosol Science* 14.3, pp. 354–357. ISSN: 0021-8502. DOI: 10.1016/0021-8502(83)90133-7. (Visited on 05/06/2020).

R. C. Flagan (Jan. 1998). “History of Electrical Aerosol Measurements”. In: *Aerosol Science and Technology* 28.4, pp. 301–380. ISSN: 0278-6826. DOI: 10.1080/02786829808965530. (Visited on 05/06/2020).

– (June 1999). “On Differential Mobility Analyzer Resolution”. In: *Aerosol Science and Technology* 30.6, pp. 556–570. ISSN: 0278-6826. DOI: 10.1080/027868299304417. (Visited on 05/07/2020).

– (Sept. 2004). “Opposed Migration Aerosol Classifier (OMAC)”. en. In: *Aerosol Science and Technology* 38.9, pp. 890–899. ISSN: 0278-6826, 1521-7388. DOI: 10.1080/027868290505242. (Visited on 03/24/2020).

H. Gordon et al. (2017). “Causes and importance of new particle formation in the present-day and preindustrial atmospheres”. en. In: *Journal of Geophysical Research: Atmospheres* 122.16, pp. 8739–8760. ISSN: 2169-8996. DOI: 10.1002/2017JD026844. (Visited on 05/06/2020).

S. V. Hering et al. (Jan. 2019). “A MAGIC concept for self-sustained, water-based, ultrafine particle counting”. In: *Aerosol Science and Technology* 53.1, pp. 63–72. ISSN: 0278-6826. DOI: 10.1080/02786826.2018.1538549. (Visited on 05/07/2020).

K. Iida et al. (Jan. 2009). “Effect of Working Fluid on Sub-2 nm Particle Detection with a Laminar Flow Ultrafine Condensation Particle Counter”. In: *Aerosol Science and Technology* 43.1, pp. 81–96. ISSN: 0278-6826. DOI: 10.1080/02786820802488194. (Visited on 05/07/2020).

V.-M. Kerminen et al. (Sept. 2018). “Atmospheric new particle formation and growth: review of field observations”. en. In: *Environmental Research Letters* 13.10, p. 103003. ISSN: 1748-9326. DOI: 10.1088/1748-9326/aadf3c. (Visited on 03/23/2020).

J. Kirkby et al. (Aug. 2011). “Role of sulphuric acid, ammonia and galactic cosmic rays in atmospheric aerosol nucleation”. en. In: *Nature* 476.7361, pp. 429–433. ISSN: 1476-4687. DOI: 10.1038/nature10343. (Visited on 10/23/2018).

J. Kirkby et al. (May 2016). “Ion-induced nucleation of pure biogenic particles”. en. In: *Nature* 533.7604, pp. 521–526. ISSN: 1476-4687. DOI: 10.1038/nature17953. (Visited on 06/25/2018).

E. O. Knutson and K. T. Whitby (Nov. 1975). “Aerosol classification by electric mobility: apparatus, theory, and applications”. en. In: *Journal of Aerosol Science* 6.6, pp. 443–451. ISSN: 0021-8502. DOI: 10.1016/0021-8502(75)90060-9. (Visited on 05/06/2020).

M. Kulmala et al. (2004). “Formation and growth rates of ultrafine atmospheric particles: A review of observations”. In: *Journal of Aerosol Science* 35, pp. 143–176. DOI: 10.1016/j.jaerosci.2003.10.003.

S.-H. Lee et al. (2019). “New Particle Formation in the Atmosphere: From Molecular Clusters to Global Climate”. In: *Journal of Geophysical Research: Atmospheres* 124.13, pp. 7098–7146. DOI: 10.1029/2018JD029356.

X. Lòpez-Yglesias and R. C. Flagan (June 2013). “Population Balances of Micron-Sized Aerosols in a Bipolar Ion Environment”. In: *Aerosol Science and Technology* 47.6, pp. 681–687. ISSN: 0278-6826. DOI: 10.1080/02786826.2013.783683. (Visited on 05/07/2020).

H. Mai and R. C. Flagan (Dec. 2018). “Scanning DMA Data Analysis I. Classification Transfer Function”. In: *Aerosol Science and Technology* 52.12, pp. 1382–1399. ISSN: 0278-6826. DOI: 10.1080/02786826.2018.1528005. (Visited on 05/09/2020).

H. Mai et al. (Dec. 2018). “Scanning DMA data analysis II. Integrated DMA-CPC instrument response and data inversion”. In: *Aerosol Science and Technology* 52.12, pp. 1400–1414. ISSN: 0278-6826. DOI: 10.1080/02786826.2018.1528006. (Visited on 05/09/2020).

J. Merikanto et al. (2009). “Impact of nucleation on global CCN”. en. In: *Atmos. Chem. Phys.*, p. 16. DOI: 10.5194/acp-9-8601-2009.

M. Merritt and Y. Zhang (July 2005). “Interior-Point Gradient Method for Large-Scale Totally Nonnegative Least Squares Problems”. en. In: *Journal of Optimization Theory and Applications* 126.1, pp. 191–202. ISSN: 1573-2878. DOI: 10.1007/s10957-005-2668-z. (Visited on 05/13/2020).

W. Mui et al. (July 2013). “Ion Mobility-Mass Spectrometry with a Radial Opposed Migration Ion and Aerosol Classifier (ROMIAC)”. In: *Analytical Chemistry* 85.13, pp. 6319–6326. ISSN: 0003-2700. DOI: 10.1021/ac400580u. (Visited on 05/06/2020).

W. Mui et al. (July 2017). “Design, simulation, and characterization of a radial opposed migration ion and aerosol classifier (ROMIAC)”. In: *Aerosol Science and Technology* 51.7, pp. 801–823. ISSN: 0278-6826. DOI: 10.1080/02786826.2017.1315046. (Visited on 06/21/2018).

C. D. O'Dowd et al. (June 2002). "Marine aerosol formation from biogenic iodine emissions". en. In: *Nature* 417.6889, pp. 632–636. ISSN: 1476-4687. DOI: 10.1038/nature00775. (Visited on 05/06/2020).

P. Paasonen et al. (Nov. 2010). "On the roles of sulphuric acid and low-volatility organic vapours in the initial steps of atmospheric new particle formation". English. In: *Atmospheric Chemistry and Physics* 10.22, pp. 11223–11242. ISSN: 1680-7316. DOI: https://doi.org/10.5194/acp-10-11223-2010. (Visited on 05/06/2020).

F. R. Quant et al. (Jan. 1992). "Performance of condensation particle counters with three continuous-flow designs". en. In: *Journal of Aerosol Science*. Proceedings of the 1992 European Aerosol Conference 23, pp. 405–408. ISSN: 0021-8502. DOI: 10.1016/0021-8502(92)90435-X. (Visited on 05/06/2020).

D. J. Rader and P. H. McMurry (Jan. 1986). "Application of the tandem differential mobility analyzer to studies of droplet growth or evaporation". en. In: *Journal of Aerosol Science* 17.5, pp. 771–787. ISSN: 0021-8502. DOI: 10.1016/0021-8502(86)90031-5. (Visited on 05/11/2020).

J. Rosell-Llompart et al. (July 1996). "Sizing nanoparticles and ions with a short differential mobility analyzer". en. In: *Journal of Aerosol Science* 27.5, pp. 695–719. ISSN: 0021-8502. DOI: 10.1016/0021-8502(96)00016-X. (Visited on 05/20/2020).

L. M. Russell et al. (Jan. 1995). "Asymmetric Instrument Response Resulting from Mixing Effects in Accelerated DMA-CPC Measurements". In: *Aerosol Science and Technology* 23.4, pp. 491–509. ISSN: 0278-6826. DOI: 10.1080/02786829508965332. (Visited on 05/06/2020).

L. A. Sgro and J. F. d. l. Mora (Jan. 2004). "A Simple Turbulent Mixing CNC for Charged Particle Detection Down to 1.2 nm". In: *Aerosol Science and Technology* 38.1, pp. 1–11. ISSN: 0278-6826. DOI: 10.1080/02786820490247560.

S. D. Shah and D. R. Cocker (June 2005). "A Fast Scanning Mobility Particle Spectrometer for Monitoring Transient Particle Size Distributions". In: *Aerosol Science and Technology* 39.6, pp. 519–526. ISSN: 0278-6826. DOI: 10.1080/027868291004652.

G. Steiner et al. (Mar. 2014). "High-Resolution Mobility and Mass Spectrometry of Negative Ions Produced in a 241Am Aerosol Charger". In: *Aerosol Science and Technology* 48.3, pp. 261–270. ISSN: 0278-6826. DOI: 10.1080/02786826.2013.870327.

D. Stolzenburg et al. (May 2017). "A DMA-train for precision measurement of sub-10 nm aerosol dynamics". English. In: *Atmospheric Measurement Techniques* 10.4, pp. 1639–1651. ISSN: 1867-1381. DOI: doi.org/10.5194/amt-10-1639-2017. (Visited on 11/21/2018).

M. R. Stolzenburg and P. H. McMurry (Jan. 1991). "An Ultrafine Aerosol Condensation Nucleus Counter". In: *Aerosol Science and Technology* 14.1, pp. 48–65. ISSN: 0278-6826. DOI: 10.1080/02786829108959470. (Visited on 05/06/2020).

J. Tröstl et al. (Sept. 2015). "Fast and precise measurement in the sub-20nm size range using a Scanning Mobility Particle Sizer". In: *Journal of Aerosol Science* 87, pp. 75–87. ISSN: 0021-8502. DOI: 10.1016/j.jaerosci.2015.04.001. (Visited on 06/26/2019).

S. Ude and J. F. de la Mora (Oct. 2005). "Molecular monodisperse mobility and mass standards from electrosprays of tetra-alkyl ammonium halides". en. In: *Journal of Aerosol Science* 36.10, pp. 1224–1237. ISSN: 00218502. DOI: 10.1016/j.jaerosci.2005.02.009. (Visited on 07/17/2019).

R. Wagner et al. (Dec. 2017). "The role of ions in new particle formation in the CLOUD chamber". English. In: *Atmospheric Chemistry and Physics* 17.24. Publisher: Copernicus GmbH, pp. 15181–15197. ISSN: 1680-7316. DOI: https://doi.org/10.5194/acp-17-15181-2017. URL: https://www.atmos-chem-phys.net/17/15181/2017/ (visited on 05/21/2020).

J. Wang et al. (June 2002). "Fast Mixing Condensation Nucleus Counter: Application to Rapid Scanning Differential Mobility Analyzer Measurements". In: *Aerosol Science and Technology* 36.6, pp. 678–689. ISSN: 0278-6826. DOI: 10.1080/02786820290038366. (Visited on 05/06/2020).

M. Wang et al. (May 2020). "Rapid growth of new atmospheric particles by nitric acid and ammonia condensation". en. In: *Nature* 581.7807, pp. 184–189. ISSN: 1476-4687. DOI: 10.1038/s41586-020-2270-4. (Visited on 05/13/2020).

S. C. Wang and R. C. Flagan (Jan. 1990). "Scanning Electrical Mobility Spectrometer". In: *Aerosol Science and Technology* 13.2, pp. 230–240. ISSN: 0278-6826. DOI: 10.1080/02786829008959441. (Visited on 05/06/2020).

Z. Wang et al. (Jan. 2017). "New particle formation in China: Current knowledge and further directions". en. In: *Science of The Total Environment* 577, pp. 258–266. ISSN: 0048-9697. DOI: 10.1016/j.scitotenv.2016.10.177. (Visited on 05/06/2020).

A. Wiedensohler (June 1988). "An approximation of the bipolar charge distribution for particles in the submicron size range". en. In: *Journal of Aerosol Science* 19.3, pp. 387–389. ISSN: 0021-8502. DOI: 10.1016/0021-8502(88)90278-9. (Visited on 05/07/2020).

W. Winklmayr et al. (Jan. 1991). "A new electromobility spectrometer for the measurement of aerosol size distributions in the size range from 1 to 1000 nm". en. In: *Journal of Aerosol Science* 22.3, pp. 289–296. ISSN: 0021-8502. DOI: 10.1016/S0021-8502(05)80007-2. (Visited on 05/06/2020).

L. Yao et al. (July 2018). “Atmospheric new particle formation from sulfuric acid and amines in a Chinese megacity”. en. In: *Science* 361.6399, pp. 278–281. ISSN: 0036-8075, 1095-9203. DOI: 10.1126/science.aao4839. (Visited on 05/06/2020).

S.-H. Zhang et al. (Jan. 1995). “Radial Differential Mobility Analyzer”. In: *Aerosol Science and Technology* 23.3, pp. 357–372. ISSN: 0278-6826. DOI: 10.1080/02786829508965320. (Visited on 05/06/2020).

Chapter 3

RAPID GROWTH OF NEW ATMOSPHERIC PARTICLES BY NITRIC ACID AND AMMONIA CONDENSATION

M. Wang, W. Kong*, R. Marten, and the CLOUD Collaboration (May 2020). "Rapid growth of new atmospheric particles by nitric acid and ammonia condensation". In: *Nature* 581.7807, pp. 184–189. ISSN: 1476-4687. DOI: 10.1038/s41586-020-2270-4.

Abstract

New-particle formation is a major contributor to urban smog (Stanier et al., 2004; Yao et al., 2018), but how it occurs in cities is often puzzling (Kulmala et al., 2017). If urban particle growth rates are similar to those found in cleaner environments (1-10 nm/h), then current understanding suggests that new urban particles should be rapidly scavenged by the high concentration of pre-existing particles. Here we show with experiments performed under atmospheric conditions in the CLOUD chamber at CERN that, below about +5 °C, nitric acid and ammonia vapors can condense onto freshly nucleated particles as small as a few nanometers in diameter. Moreover, when it is cold enough (below -15 °C), nitric acid and ammonia can nucleate directly via an acid-base stabilization mechanism to form ammonium nitrate particles. Since these vapors are often 1000 times more abundant than sulfuric acid, the resulting particle growth rates can be extremely high, reaching well above 100 nm/h. However, these high growth rates require the gas-particle ammonium nitrate system to be out of equilibrium to sustain gas-phase supersaturations. In view of the strong temperature dependence that we measure for the gas-phase supersaturations, we expect such transient conditions can occur in inhomogeneous urban settings, especially in wintertime with strong local sources such as traffic, as well as vertical mixing. Even though rapid growth from nitric acid and ammonia condensation may last for only a few minutes, it is nonetheless fast enough to shepherd freshly nucleated particles through the smallest size range where they are most vulnerable to scavenging loss, thus greatly increasing their survival probability. We also expect nitric acid and ammonia nucleation and rapid growth to be important in the relatively clean and cold upper free troposphere, where ammonia can be convected from the continental boundary layer and nitric acid is abundant from electrical

storms (Höpfner et al., 2019; Williamson et al., 2019).

3.1 Introduction

New-particle formation may mask up to half of the radiative forcing caused since the industrial revolution by carbon dioxide and other long-lived greenhouse gases (Boucher et al., 2013). Present-day particle formation is thought to predominantly involve sulfuric acid vapors globally (McMurry et al., 2005; Kulmala et al., 2013; Gordon et al., 2017). Subsequent particle growth is richer, often involving organics (Riipinen et al., 2012). Often growth is the limiting step for survival of particles from freshly nucleated clusters to diameters of 50 or 100 nm, where they become large enough to directly scatter light and also to seed cloud formation (Pierce and Adams, 2007; Kuang et al., 2009).

New-particle formation in megacities is especially important (Yao et al., 2018), in part because air pollution in megacities constitutes a public health crisis (Apte et al., 2018) but also because the regional climate forcing associated with megacity urban haze can be large (Chen et al., 2018). However, new-particle formation in highly polluted megacities is often perplexing, because the apparent particle growth rates are only modestly faster than growth rates in remote areas (roughly a factor of 3) whereas the vapor condensation sink (to background particles) is up to two orders of magnitude larger (Fig. 3.7). This implies a very low survival probability in the "valley of death", where particles with diameters $d_p \leq 10$ nm have high Brownian diffusivity and will be lost by coagulational scavenging unless they grow rapidly (Kerminen and Kulmala, 2002; McMurry et al., 2005).

Ammonium nitrate has long been recognized as an important yet semi-volatile constituent of atmospheric aerosols (Takahama et al., 2004). Especially in winter and in agricultural areas, particulate nitrate can be a substantial air-quality problem (Xu et al., 2019). However, the partitioning of nitric acid and ammonia vapors with particulate ammonium nitrate is thought to rapidly reach an equilibrium, often favoring the gas phase when it is warm.

Because ammonium nitrate is semi volatile, nitric acid has not been thought to play an important role in new-particle formation and growth, where very low vapor pressures are required for constituents to be important. This includes sulfuric acid (McMurry, 1980) but also very low vapor pressure organics (Kirkby et al., 2016; Stolzenburg et al., 2018) and iodine oxides (O'Dowd et al., 2002). However, it is saturation ratio and not vapor pressure per se that determines the thermodynamic driving force

for condensation, and nitric acid can be three or four orders of magnitude more abundant than sulfuric acid in urban environments. Thus, even a small fractional supersaturation of nitric acid and ammonia vapors with respect to ammonium nitrate has the potential to drive very rapid particle growth, carrying very small, freshly nucleated particles through the valley of death in a few minutes. These rapid growth events can exceed 100 nm/h under urban conditions – an order of magnitude higher than previous observations – and the growth will continue until the vapors are exhausted and conditions return to equilibrium. Such transients will be difficult to identify in inhomogeneous urban environments yet have the potential to explain the puzzling observations of new-particle formation in highly polluted megacities.

3.2 Methods

The CLOUD facility

We conducted our measurements at the CERN CLOUD facility, a 26.1 m^3 electropolished stainless-steel CLOUD chamber that enables new-particle formation experiments under the full range of tropospheric conditions with scrupulous cleanliness and minimal contamination (Kirkby et al., 2011; Duplissy et al., 2016). The CLOUD chamber is mounted in a thermal housing, capable of keeping temperature constant in a range of -65 °C and +100 °C with ±0.1 °C precision (Dias et al., 2017) and relative humidity between 0.5 % and 101 %. Photochemical processes are initiated by homogeneous illumination with a built-in ultraviolet fiber-optic system, including four 200 W Hamamatsu Hg-Xe lamps at wavelengths between 250 and 450 nm and a 4 W KrF excimer UV laser at 248 nm with adjustable power. Ion-induced nucleation under different ionization levels is simulated with a combination of electric fields (±30 kV) and a high-flux beam of 3.6 GeV pions (π^+), which can artificially scavenge or enhance small ions. Uniform spatial mixing is achieved with magnetically coupled stainless-steel fans mounted at the top and bottom of the chamber. The characteristic gas mixing time in the chamber during experiments is a few minutes. The loss rate of condensable vapors and particles onto the chamber walls is comparable to the ambient condensation sink. To avoid contamination, the chamber is periodically cleaned through rinsing the walls with ultra-pure water and heating to 100 °C for at least 24 hours, ensuring extremely low contaminant levels of sulfuric acid $< 5 \times 10^4$ cm^{-3} and total organics < 50 pptv (Kirkby et al., 2016; Schnitzhofer et al., 2014). The CLOUD gas system is also built to the highest technical standards of cleanliness and performance. The dry air supply for the chamber is provided by boil-off oxygen (Messer, 99.999 %) and boil-off nitrogen (Messer,

99.999 %) mixed at the atmospheric ratio of 79:21. Highly pure water vapor, ozone and other trace gases can be precisely added at the pptv level.

Typical experimental sequence

To investigate the role of nitric acid in new-particle formation, we performed particle growth experiments at T = -10 °C, +5 °C, and +20 °C respectively, and (for the most part) RH $\simeq$ 60 %. A typical experiment started with illumination of the chamber at constant O_3 to photochemically produce ·OH radicals. The subsequent oxidation of pre-mixed SO_2, NO_2 and anthropogenic volatile organic compounds (VOCs, i.e. toluene or cresol) led to production of H_2SO_4, HNO_3 and Highly Oxygenated Organic Molecules (HOMs), respectively. As a result, nucleation was induced, followed once the particles reached an activation diameter, d_{act}, by rapid growth via condensation of nitric acid and ammonia. In some experiments, we also injected nitric acid vapor directly into the CLOUD chamber from an ultra-pure source to cover a wide range of conditions. In addition, to prove consistency we also carried out experiments with a biogenic precursor, α-pinene, as the replacement of anthropogenic VOCs as well as experiments without any organic vapors. For the experiments we focus on here, the HOM concentrations were either zero or small enough to have a minor effect on the experiment. In one case, we cooled the particle-free (< 1 cm^{-3}) chamber continuously from -10 °C to -25 °C, while holding nitric acid and ammonia at a constant level, but with no sulfuric acid ($< 5 \times 10^4$ cm^{-3} or 2×10^{-3} pptv). We observed new-particle formation purely from nitric acid and ammonia starting at -15 °C. The nucleation rate grew as the temperature dropped. Moreover, as shown in Fig. 3.1, at -25 °C, new-particle formation events appeared to be quenched when we swept out primary ions with the electric field, and not return until turning off the field to allow the primary ion production by galactic cosmic rays to again accumulate (~ 700 cm^{-3}). We list the chamber conditions and key parameters for all the experiments presented in this work in Table 3.2.

Instrumentation

To measure gas-phase nitric acid, we deployed a bromide chemical ionisation atmospheric pressure interface time-of-flight (CI-APi-TOF) mass spectrometer (Jokinen et al., 2012; Junninen et al., 2010) equipped with a commercial inlet (Airmodus, Ltd) to minimize wall contact of the sample (Eisele and Tanner, 1993). We flow dibromomethane (CH_2Br_2) into the ion-molecule reaction inlet to produce the primary reagent ion Br^-. During its collision with HNO_3, Br^- reacts either to form a

cluster or via a proton transfer from the HNO_3 to form NO_3^-:

$$Br^- + HNO_3 \rightarrow HNO_3 \cdot Br^-$$

$$Br^- + HNO_3 \rightarrow HBr + NO_3^-$$

To take the variation in the total reagent ions into account, nitric acid concentrations were quantified according to:

$$[HNO_3] = \frac{[NO_3^-]}{[Br^-] + [H_2O \cdot Br^-]} \times C$$

where C (in unit of pptv) is a calibration coefficient obtained by measuring HNO_3/N_2 mixtures with known nitric acid concentrations. The nitric acid source was a portable permeation tube, kept constantly at 40 °C. A 2 lpm N_2 flow was introduced into the permeation device to carry out nitric acid vapor. To determine the permeation rate of nitric acid, the outflow of the permeation tube was passed through an impinger containing deionized water, and the resulting nitric acid solution was analyzed via spectrophotometry. Line losses during the experiments and calibration procedures were calculated separately. The corrected calibration coefficient was determined as 7364 pptv.

Gas-phase ammonia was measured by a water cluster CI-APi-TOF mass spectrometer that was recently described elsewhere (Pfeifer et al., 2019). The crossflow ion source coupled to a TOF-MS enables the selective measurement of basic compounds (e.g. ammonia) by using positively charged water clusters as primary ions. Due to the low reaction times (< 1 ms), the instrument responds rapidly to changing chamber conditions with a detection limit of ammonia of 0.5 pptv.

Gas-phase sulfuric acid as well as highly oxygenated organic molecules (HOMs) were routinely measured with a detection limit of $\sim 5 \times 10^4$ cm^{-3} by two nitrate CI-APi-TOF mass spectrometers. One instrument was equipped with the Airmodus inlet and an X-ray generator as the ion source; the other deployed a homemade inlet and a corona discharge for ion generation (Kürten et al., 2011). An electrostatic filter was installed in front of each instrument to remove ions and charged clusters formed in the chamber. sulfuric acid and HOMs were quantified following the same calibration and loss correction procedures described previously (Kirkby et al., 2016; Tröstl et al., 2016; Kirkby et al., 2011).

Volatile organic compounds (VOCs) were monitored by a proton transfer reaction time of flight mass spectrometer (PTR-TOF-MS, Ionicon Analytik); it also provides

information about the overall cleanliness regarding VOCs in the chamber. The technique was extensively described previously (Breitenlechner et al., 2017). Direct calibration using diffusion sources allows for determination of mixing ratio of VOCs with an accuracy of 5 % and a typical detection limit of 25 pptv (Gautrois and Koppmann, 1999).

Gas monitors were used to measure ozone (O_3, Thermo Environmental Instruments TEI 49C), sulfur dioxide (SO_2, Thermo Fisher Scientific Inc. 42i-TLE) and nitric oxide (NO, ECO Physics, CLD 780TR). Nitrogen dioxide (NO_2) was measured by a cavity attenuated phase shift nitrogen dioxide monitor (CAPS NO_2, Aerodyne Research Inc.) and a homemade cavity enhanced differential optical absorption spectroscopy (CE-DOAS) instrument. Relative humidity of the chamber was determined by dew point mirrors (EdgeTech).

We measured the particle-phase composition via thermal desorption using an iodide-adduct chemical ionisation time-of-flight mass spectrometer equipped with a Filter Inlet for Gases and AEROsols (FIGAERO-CIMS) (M. Wang et al., 2016; Lopez-Hilfiker et al., 2014). FIGAERO is a manifold inlet for a CIMS with two operating modes. In one mode, gases are directly sampled into a 100 mbar turbulent flow ion-molecule reactor while particles are concurrently collected on a PTFE filter via a separate dedicated port. In the other mode, the filter is automatically moved into a pure N_2 gas stream flowing into the ion molecule reactor while the N_2 is progressively heated to evaporate the particles via temperature programmed desorption. Analytes are then chemically ionized and extracted into a TOF-MS, achieving a detection limit below 10^6 cm^{-3}.

Particle size distributions between 1.8 nm and 500 nm were monitored continuously by a differential mobility analyzer train (DMA-Train), a nano-Scanning Electrical Mobility Spectrometer (nSEMS), a nano-Scanning Mobility Particle Sizer (nano-SMPS), and a long-SMPS. The DMA-Train was constructed with six identical DMAs operating at different, but fixed, voltages. Particles transmitted through the DMAs were then detected by either a particle size magnifier (PSM) or a CPC, depending on the size ranges. An approximation of the size distribution with 15 size bins was acquired by logarithmic interpolation between the six channels (Stolzenburg et al., 2017). The nSEMS employed a novel, radial opposed migration ion and aerosol classifier (ROMIAC), which is less sensitive to diffusional resolution degradation than the DMAs (Mui et al., 2017), and a soft X-ray charge conditioner. After leaving the classifier, particles were first activated in a fast-mixing diethylene glycol stage

(Wimmer et al., 2013), and then counted with a butanol-CPC. The nSEMS transfer function that was used to invert the data to obtain the particle size distribution was derived using 3D finite element modeling of the flows, electric field, and particle trajectories (Mai and C. Flagan, 2018; Mai et al., 2018). The two commercial mobility particle size spectrometers, nano-SMPS and long-SMPS, have been fully characterized, calibrated and validated in several previous studies (Jurányi et al., 2011; Tröstl et al., 2015; Wiedensohler et al., 2012).

Determination of growth rate

The combined particle size distribution was reconstructed using measurement data from DMA-Train at 1.8-4.3 nm, nSEMS at 4.3-18.1 nm, nano-SMPS at 18.1-55.2 nm, and long-SMPS at 55.2-500 nm, and synchronized with long-SMPS measurement time. We list the sizing and resolution information of these instruments in Table 3.1.

Instrument	Components	Size Range	Size Resolution	Time Resolution
DMA-Train	Grimm S-DMA TSI 3776 CPC TSI 3788 CPC Airmodus A10 PSM	1.8 nm - 8.0 nm	15 bins	1 s
nSEMS	ROMIAC TSI 3760A CPC	1.5 nm - 23 nm	240 bins	1 min
nano-SMPS	TSI 3938 SMPS TSI 3776 CPC	2 nm - 64 nm	96 bins	1 min
long-SMPS	TSI 3071 DMA TSI 3776 CPC	20 nm - 500 nm	84 bins	5 min

Table 3.1: Specifications of the four particle sizing instruments employed in this work.

As depicted in Fig. 3.2a, the four instruments showed excellent agreement in their overlapping regions of the size ranges. The total number concentration obtained by integrating the combined size distribution agreed well with measurement by an Airmodus A11 nano condensation nucleus counter (nCNC) and a TSI 3776 ultrafine condensation particle counter (UCPC) (Fig. 3.2b). Particle growth rate, $\mathrm{d}d_p/\mathrm{d}t$, was then determined from the combined size distributions using the 50 % appearance time method (Stolzenburg et al., 2018), as a clear front of a growing particle population could be identified during most rapid growth events (Fig. 3.3). For the rapid growth rates, which are the principal focus here, the SMPS measurements provided the major constraint.

Determination of activation diameter.

The activation diameter (d_{act}) was interpreted as the size at which growth accelerated from the slow, initial rate to the rapid, post-activation rate. The activation diameter was determined using the particle size distribution acquired from DMA-Train or nSEMS at small sizes (< 15 nm). At the activation diameter, the growth rate calculated from the 50 % appearance time usually experienced a sharp change, from below 10 nm h^{-1}, often to over 100 nm h^{-1}, depending on concentrations of supersaturated HNO_3 and NH_3 vapors. Fast growth rate leads to relatively low steady-state concentration of particles just above the activation diameter; the activation event often resulted in a notable gap in the particle-number size distribution. In some cases, a clear bimodal distribution was observed with the number concentration in one size bin plunging below 10 counts cm^{-3} while the counts at larger sizes rose to more than 100 counts cm^{-3}; the centroid diameter of the size bin at which the number concentration dropped was then defined as the activation diameter (Fig. 3.4a).

Calculation of saturation ratio

We model the ammonium nitrate formed in the particle-phase as solids in our particle growth experiments since the relative humidity (~60 %) was less than the deliquescence relative humidity (DRH), given by (Seinfeld and Pandis, 2006)

$$\ln(DRH) = \frac{723.7}{T} + 1.6954 \tag{3.1}$$

The dissociation constant, K_p, is defined as the product of the equilibrium partial pressures of HNO_3 and NH_3. K_p can be estimated by integrating the van't Hoff equation (Denbigh and Denbigh, 1981). The resulting equation for K_p in units of ppb^2 (assuming 1 atm of total pressure) (Mozurkewich, 1993) is

$$\ln K_p = 118.87 - \frac{24084}{T} - 6.025 \ln(T) \tag{3.2}$$

The saturation ratio, S, is thus calculated via dividing the product of measured mixing ratios of HNO_3 and NH_3 by the dissociation constant. The dissociation constant is quite sensitive to temperature changes, varying over more than two orders of magnitude for typical ambient conditions. Several degrees of temperature drop can lead to much higher saturation ratio, shifting the equilibrium of the system toward the particle-phase drastically. As illustrated in Fig. 3.5, with an adiabatic lapse rate of -9 °C/km during fast vertical mixing, upward transport of a few hundred meters alone is sufficient for a saturated nitric acid and ammonia air parcel to reach the saturation ratio capable of triggering rapid growth at a few nanometers.

Determination of nucleation rate

The nucleation rate, $J_{1.7}$, is determined at 1.7 nm mobility diameter (1.4 nm physical diameter) here using particle size magnifier (PSM). At 1.7 nm, a particle is normally considered to be above its critical size and, therefore, thermodynamically stable. $J_{1.7}$ is calculated using the flux of the total concentration of particles growing past a specific diameter (here at 1.7 nm), as well as correction terms accounting for aerosol losses due to dilution in the chamber, wall losses and coagulation. Details can be found in our previous work (Lehtipalo et al., 2018).

The MABNAG model

To compare our measurements to thermodynamic predictions (including the Kelvin term for curved surfaces), we employed the model for acid-base chemistry in nanoparticle growth (MABNAG) (Yli-Juuti et al., 2013). MABNAG is a monodisperse particle population growth model that calculates the time evolution of particle's composition and size based on concentrations of condensing gases, RH and ambient temperature, considering also the dissociation and protonation between acids and bases in the particle phase. In the model water and bases are assumed always to be in equilibrium state between gas and particle phase. Mass fluxes of acids to and from the particles are determined based on their gas phase concentrations and their equilibrium vapor concentrations. In order to solve for the dissociation and composition dependent equilibrium concentrations, MABNAG couples a particle growth model to extended aerosol inorganics model (E-AIM) (Clegg and Seinfeld, 2006a; Clegg and Seinfeld, 2006b). In this study, we assumed particles in MABNAG as liquid droplets at +5 °C and -10 °C, and 60 % relative humidity. The simulation system consisted of four compounds: water, ammonia, sulfuric acid and nitric acid. The initial particle composition in each simulation was 40 sulfuric acid molecules and a corresponding amount of water and ammonia according to gas-particle equilibrium based on their gas concentrations. With this setting, the initial diameter was approximately 2 nm. Particle density and surface tension were set to 1500 kg m^{-3} and 0.03 N m^{-1}, respectively. In Fig. 3.6, we show that MAGNAG computations confirm that nitric acid and ammonia at the measured concentrations can activate small particles and cause rapid growth, and also confirm that the activation diameter depends on the ammonium nitrate saturation ratio, consistent with our measured diameter (diamonds in Fig. 3.10a).

Nano-Köhler theory

To prove consistency, we also calculated the equilibrium saturation ratios of ammonium nitrate above curved particle surfaces according to nano-Köhler theory (Kontkanen et al., 2018). This theory describes the activation of nanometer-sized inorganic clusters to growth by vapor condensation, which is analogous to Köhler theory describing the activation of CCN to cloud droplets. In this study, we assumed seed particles of ammonium sulfate, and performed calculations for three seed particle diameters (d_s = 1.4, 2.0, and 2.9 nm, respectively) at +5 °C and -10 °C, and at 60 % relative humidity. The equilibrium vapor pressures of HNO_3 and NH_3 over the liquid phase, and surface tension and density of liquid phase were obtained from E-AIM model (Clegg and Seinfeld, 2006a; Clegg and Seinfeld, 2006b). The equilibrium saturation ratios of ammonium nitrate were calculated as described in Section M6, also including the Kelvin term. The resulting Köhler curves showing the equilibrium saturation ratio as a function of particle diameter are presented in Fig. 3.4c. The maxima of each curve corresponds to the activation diameter (d_{act}); saturation ratios of 10 to 50 lead to d_{act} of 3 to 5 nm, consistent with our measurements in Fig. 3.10a. We summarize detailed results in Table 3.2.

Ambient nucleation and growth

In Table 3.3 we compile ambient observations of nucleation rates, growth rates, and the ambient condensation sink. In most cases these are derived from evolving particle size distributions. We summarize these observations in Fig. 3.7.

3.3 Results

Here we report experiments performed with mixtures of nitric acid, sulfuric acid, and ammonia vapors under atmospheric conditions in the CERN CLOUD chamber (Cosmics Leaving OUtdoor Droplets (Kirkby et al., 2011); see Methods for experimental details) from 21 September to 7 December 2018 (CLOUD 13). We varied the temperature from +20 to -10 °C, and in one case cooled progressively from -15 to -25 °C. We adjusted levels of sulfuric acid (H_2SO_4), ammonia (NH_3), and nitric acid (HNO_3), as well as aromatic precursors, to span ranges typical of polluted megacities. In Fig. 3.8 we show two representative events at -10 °C. In Fig. 3.8a we oxidized SO_2 with OH to form H_2SO_4 in the presence of 1915 pptv ammonia. The resulting "banana" is typical of such experiments as well as ambient observations under relatively clean conditions, with a single nucleation mode that appears shortly after the onset of nucleation and grows at roughly 20 nm/h. In Fig. 3.8b we repeated

Run	T (°C)	HNO_3 (pptv)	NH_3 (pptv)	H_2SO_4 (pptv)	HOMs (pptv)	RH %	d_{act} (nm)
2163.01	+20	150	2400	3.60	n/a	60	n/a
2140.06	+5	860	259	0.96	5.18	60	9.4
2140.08	+5	971	242	0.84	5.29	60	10.4
2140.10	+5	1130	244	0.88	5.25	60	10.0
2170.05	+5	292	370	3.00	n/a	60	n/a
2170.15	+5	1117	883	1.48	n/a	60	2.3
2170.20	+5	352	1387	1.48	n/a	60	4.7
2174.06	+5	640*	904	0.46	12.01	60	3.9
2156.13	-10	228	1085	0.16	n/a	60	1.6
2156.15	-10	64	2371	0.06	n/a	60	2.1
2156.17	-10	41	2659	0.07	n/a	60	2.4
2157.06	-10	n/a	1915	0.44	0.32	60	n/a
2158.02	-10	59 *	2654	0.38	0.26	60	2.9
2158.04	-10	24 *	2131	0.46	0.28	60	4.6
2158.06	-10	24 *	2077	0.36	0.29	60	4.5
2159.02	-10	23 *	1835	0.72	0.67	60	4.5
2159.04	-10	30 *	1694	1.04	0.78	60	4.9
2160.02	-10	16 *	1663	0.60	0.25	60	5.9
2160.06	-10	16 *	2535	0.30	0.23	60	6.5
2162.01	-15 → -24	272	1647	< 0.002	n/a	60 → 40	Nucleation

*HNO_3 production via NO_2 photo-oxidation.

Table 3.2: Conditions for all nucleation and growth experiments, and nano-Köhler simulations discussed in this work.

*HNO_3 production via NO_2 photo-oxidation.

this experiment but also with 5.8 ppbv NO_2, which was oxidized by OH to produce 24 pptv of HNO_3 vapor. The resulting size distribution initially resembles the first case, but when the particles reach about 5 nm, their growth rate accelerates to roughly 45 nm/h. This activation is reminiscent of cloud-droplet activation and thus suggestive of "nano-Köhler" behavior and the Kelvin curvature effect (Kontkanen et al., 2018).

We repeated these experiments over a range of conditions, either forming HNO_3 via NO_2 oxidation or injecting it directly into the CLOUD chamber from an ultra-pure evaporation source. We observed this activation and rapid growth behavior consistently. In Fig. 3.8c we show the resulting rapid growth rates after activation, based on the 50 % appearance time of the upper branch, at -10 °C (green) and +5 °C (purple) plotted against the product of the measured gas-phase HNO_3 and NH_3 mixing ratios. Both a strong correlation and a clear temperature dependence are

City/Region (Country)	J[a] ($cm^{-3} \cdot s^{-1}$)	GR[a] ($nm \cdot h^{-1}$)	CS ($10^{-4}\ s^{-1}$)	CS·10^4/GR ($h \cdot nm^{-1} \cdot s^{-1}$)	Reference
Hyytiälä (Finland)	0.8 ± 0.7	3.0 ± 1.9	17	6	Dal Maso et al., 2007
Hyytiälä (Finland)	0.6 ± 0.3	2.9± 1.4	21 ± 8.2	7	Dal Maso et al., 2005
Pallas (Finland)	0.1 ± 0.1	2.5 ± 1.7	4.8	2	Dal Maso et al., 2007
Pallas (Finland)	0.2	3.7	5.3	1	Komppula et al., 2003
Värriö (Finland)	0.9	3.6	10	3	Vehkamäki et al., 2004
Värriö (Finland)	0.2 ± 0.3	2.7 ± 1.4	7.0	3	Dal Maso et al., 2007
Tomsk (Russia)	0.4	5.5	16	3	Dal Maso et al., 2008
Sörmland (Sweden)	0.4 ± 0.4	3.9 ± 2.0	17	4	Dal Maso et al., 2007
Helsinki (Finland)	2.0	3.4	51	15	Hussein et al., 2008
Paris(France)	n/a	6.1 ± 1.8	73 ± 8	12	Pikridas et al., 2015
Po Valley (Italy)	5.9	6.8	140	20	Hamed et al., 2007
Brookfield (UK)	1.2 ± 0.4	5.3 ± 1.9	45 ± 22 $\times 10^{-3}$	9	Hama et al., 2017
Leicester (UK)	1.3 ± 0.4	7.4 ± 0.9	58 ± 8.7 $\times 10^{-3}$	8	Hama et al., 2017
Beijing (China)	n/a	3.2	290	90	Gao et al., 2012
Beijing (China)	10.8	5.2 ± 2.2	270 ± 210	52	Z. B. Wang et al., 2013
Beijing (China)	10.7 ± 6.2	5.2 ± 3.5	220 ± 130	42	Yue et al., 2018
Beijing (China)	n/a	6.5 ± 4.5	220 ± 170	34	Zhang et al., 2011
Hong Kong (China)	3.9 ± 3.5	5.6 ± 2.0	160 ± 42	28	Man et al., 2015
Nanjing (China)	3.7 ± 1.6	7.6 ± 1.2	280 ± 57	36	An et al., 2015
Nanjing (China)	1.1	8.5	240	28	Herrmann et al., 2014
Nanjing (China)	n/a	7.6 ± 1.7	230 ± 67	31	Yu et al., 2016
Shanghai (China)	8.7 ± 5.2[b]	11.4 ± 9.7	600 ± 240	53	Xiao et al., 2015
Shanghai (China)	n/a	8.0	200	25	Peng et al., 2014
Gadanki (India)	1.2 ± 2.3	4.1 ± 2.0	71 ± 46	17	Kanawade et al., 2014
New Delhi (India)	7.3 ± 3.9	14.9 ± 1.8	580 ± 89	39	Mönkkönen et al., 2005
Tecamac (Mexico)	283.0 ± 121.0[b]	26.0 ± 5.6	1300 ± 240	49	Iida et al., 2008
Tecamac (Mexico)	n/a	22.6 ± 12.3	820 ± 310	36	Iida et al., 2008
Atlanta (US)	n/a	20.0 ± 6.5	740 ± 130	37	McMurry et al., 2005
Boulder (US)	n/a	5.4 ± 1.0	230 ± 54	42	Iida et al., 2006
Boulder (US)	n/a	5.0 ± 1.0	220	43	Iida et al., 2008

Table 3.3: A summary of ambient particle formation rates (J), growth rates (GR) and condensation sinks (CS) in various remote and urban environments.

[a] J and GR were mostly calculated over the size range from a few nm to over 20 nm. [b] J calculated from 3 to 6 nm. The uncertainties indicate 1 σ errors.

evident; when it is colder, the particles grow at the same rate for a much lower product of vapor concentrations. This is consistent with semi-volatile uptake of both species, rate-limited by formation of ammonium nitrate.

To confirm this, we measured the composition of the particles using a Filter Inlet for Gases and AEROsols (FIGAERO) iodide (I^-) chemical ionisation mass spectrometer (CIMS) along with the gas-phase vapor concentrations via several CIMS methods. In Fig. 3.9 we show another rapid growth event, this one at +5 °C (indicated in Fig. 3.8c with a black outlined purple square). We started with an almost perfectly clean chamber and only vapors present (SO_2, HNO_3 and NH_3) at constant levels, as shown in Fig. 3.9a. Here we injected the HNO_3 without photochemical production so we could independently control HNO_3 and sulfuric acid. The FIGAERO showed no measurable signal in the absence of particles, indicating negligible cross-talk from

vapors. We then turned on UV lights to form OH radicals and initiate SO_2 oxidation to H_2SO_4. Fig. 3.9b shows the resulting number distribution; as in Fig. 3.8b, particles appear, grow slowly, and then activate and grow at 700 nm/h. We again show the 50 % appearance time of both modes. In Fig. 3.9c we show the associated volume distribution. Within 15 min of the onset of particle formation, the volume is dominated by the upper mode near 200 nm. Finally, in Fig. 3.9d we show a FIGAERO thermogram (signal versus desorption temperature) for particles collected between 10 and 40 min after the onset of photochemistry. Their composition is dominated by nitrate, with a much smaller but significant sulfate contribution; the semi-volatile nitrate desorbs at a much lower temperature than the sulfate. The I^- chemical ionisation is not sensitive to NH_3, but both nitrate and sulfate exist presumably as ammonium salts in the particles.

In addition to the correlation of activated particle growth rates with the product of HNO_3 and NH_3 at a given temperature, the observed activation diameter (d_{act}) shows a strong dependence on this product. The activation diameter is evident as a clear kink in the 50 % appearance curve as well as a notable absence of particles in the slower-growth mode above d_{act}. In Fig. 3.4a we show an example of how we determine d_{act}, using the emergence of a bimodal size distribution as the defining feature. In Fig. 3.10a we plot the observed activation diameter at each temperature in a phase space with [HNO_3] on the $\log(x)$ axis and [NH_3] on the $\log(y)$ axis (both in pptv). The number within each symbol is the observed activation diameter for that experiment. We show the saturation ratio of ammonium nitrate at each temperature via a series of diagonal lines in this log-log space (slope = -1); specifically, we show S = 1, 5, and 25, emphasizing S = 1 as thick solid line. We also indicate 1:1 [HNO_3]:[NH_3] with a dashed gray line (slope +1); points to the upper left (most of the values) are "nitric-acid limited", with more ammonia than nitric acid. All of these concentrations are well within ranges typically observed in wintertime mega-city conditions (Lu et al., 2019).

For both +5 and -10 °C, we consistently observe a relationship between S and d_{act} (we never achieved saturation at +20 °C and did not observe rapid growth). We observe no activation for $S < 1$, and activation for $S > 1$, with $\log(d_{act})$ inversely proportional to $\log([HNO_3]\cdot[NH_3])$ at each temperature, as shown in Fig. 3.4. Notably, d_{act} can be well under 10 nm and as low as 1.6 nm. This suggests that nitric acid and ammonia (ammonium nitrate) condensation may play a role in new-particle formation and growth within the valley of death, where very small particles are most

vulnerable to loss by coagulation (Kulmala et al., 2013).

We also performed experiments with only nitric acid, ammonia and water vapor added to the chamber (sulfuric acid contamination was measured to be $< 2 \times 10^{-3}$ pptv). For T < -15 °C and $S > 10^3$ we observed nucleation and growth of pure ammonium-nitrate particles, as shown in Fig. 3.10c. We progressively cooled the chamber to -24 °C, while holding the vapors at a constant level, as shown in Fig. 3.10b. The particle formation rate ($J_{1.7}$) rose steadily from 0.006 cm^{-3} s^{-1} to 0.06 cm^{-3} s^{-1} at -24 °C. In Fig. 3.1 we show a pure ammonium-nitrate nucleation experiment performed at -25 °C under vapor conditions reported in the tropical upper troposphere (Höpfner et al., 2019) (30-50 pptv nitric acid and 1.8 ppbv ammonia) showing that this mechanism can produce several 100 cm^{-3} particles per hour.

Our experiments show that semi-volatile ammonium nitrate can condense on tiny nanoparticles, consistent with nano-Köhler theory (Kontkanen et al., 2018). To confirm this we conducted a series of simulations using the monodisperse thermodynamic model MABNAG (Yli-Juuti et al., 2013), which treats known thermodynamics, including curvature (Kelvin) effects for a single evolving particle size. We show the points of the MABNAG simulations as triangles in Fig. 3.10a. MABNAG consistently and quantitatively confirms our experimental findings; there is little ammonium nitrate formation at $S < 1$, as expected, and activation behavior with ammonium nitrate condensation ultimately dominating the particle composition occurs at progressively smaller d_{act} as S rises well above 1.0. The calculated and observed d_{act} values are broadly consistent. In Fig. 3.11 we show two representative MABNAG growth simulations for the two points indicated with open and closed diamonds in Fig. 3.10a; the simulations show no ammonium nitrate formation when conditions are undersaturated but significant formation when conditions are saturated, with activation behavior near the observed d_{act} = 4.7 nm. We show the calculated composition as well as diameter versus time for these and other cases in Fig. 3.6.

We also conducted nano-Köhler simulations (Kontkanen et al., 2018), shown in Fig. 3.4b, which confirm the activation of ammonium nitrate condensation at diameters less than 4 nm depending on the size of an assumed ammonium sulfate core. For a given core size the critical supersaturation required for activation at -10 °C is a factor of 2-3 higher than at +5 °C, consistent with the observed behavior shown in Fig. 3.10a. While 1-2 nm particles contain only a handful of acid and base molecules, the MABNAG and Nano-Köhler simulations based on bulk

thermodynamics, with only a Kelvin term to represent the unique behavior of the nanoparticles, capture the activation and growth behaviors we observe.

3.4 Atmospheric implications

Our findings suggest that nitric acid and ammonia condensation to nanoparticles to form ammonium nitrate (or, by extension, aminium nitrates in the presence of amines) may be important in the atmosphere. This may include urban new-particle formation during wintertime via rapid growth. It may also play a role in free-tropospheric particle formation, where sufficient vapors may exist to allow nucleation and growth of pure ammonium-nitrate particles. We observe these behaviors in CLOUD for vapor concentrations well within those typical of the atmosphere.

Rapid growth may contribute to the often puzzling survival of newly-formed particles in megacities, where particles form at rates consistent with sulfuric acid - base nucleation and appear to grow at typical rates (roughly 10 nm/h) in the presence of extremely high condensation sinks that seemingly should scavenge all of the tiny nucleated particles. As shown in Fig. 3.7, the ratio of $10^4 \times$CS (1/s) and GR (nm/h) during nucleation events in Asian megacities typically ranges between 20 and 50, where the survival probability between 1.5 and 3 nm should drop precipitously (Kulmala et al., 2017). However, the observed growth rates are based on appearance times in measured ambient size distributions – just as in Figs 3.8 and 3.9 – and thus reflect a spatial and temporal average of air masses passing over a sampling site during the course of a day. Rapid growth rates can reduce CS/GR by a factor 10 or more, effectively displacing urban ratios into a range characteristic of remote regions (Fig. 3.7b). The empirically-derived nucleation rates in Fig. 3.7b are positively correlated with high CS/GR, consistent with high production rates of condensable vapors; however, the complicated microphysics below 10 nm make a simple determination of the growth rate difficult. Urban conditions are however far less homogeneous than CLOUD, or even remote boreal forests such as Hyytiälä. Because survival probability depends exponentially on CS/GR (McMurry et al., 2005; Kulmala et al., 2017), but spatial (and temporal) averaging as well as ambient mixing are linear, real urban conditions may contain pockets conducive to transient rapid growth and thus unusually high survival probability that are blurred in the (averaged) observations.

The key here is that nitric acid vapor and ammonia are often 1000 times or more

abundant than sulfuric acid vapor. Thus, although they tend toward equilibrium with ammonium nitrate in the particle phase, even a modest perturbation above saturation can unleash a tremendous thermodynamic driving force for condensational growth, nominally up to 1000 times faster than growth by sulfuric acid condensation. This may be brief, but because of this disparity in concentrations, even a small deviation in saturation ratio above 1.0 may drive rapid growth for a short period at several nm per minute as opposed to several nm per hour. The particles will not experience rapid growth for long, but they may grow fast enough to escape the valley of death.

We illustrate rapid growth in Fig. 3.11. Under most urban conditions, nucleation and the early growth up to the activation size is likely to be controlled by sulfuric acid and a base (ammonia or an amine), shown by the red "cores" in Fig. 3.11b. During the day (even in wintertime), when NO_2 is oxidized by OH in the gas phase to produce nitric acid at rates of up to 3 ppbv/h and ammonia from traffic, other combustion emissions, and agriculture can reach 8 ppbv (Lu et al., 2019), nitric acid and ammonia will not equilibrate but rather will approach a modest steady-state supersaturation driving ammonium-nitrate formation to balance the production and emissions. However, this steady state will only be reached after several e-folding time periods set by the particle condensation sink. Typically, new-particle formation occurs at the lower end of the condensation sink distribution (even under urban conditions) (McMurry et al., 2005; Yao et al., 2018), so this time scale will be several minutes, or a length scale of hundreds of meters in the horizontal and tens of meters in the vertical. There are ample sources of inhomogeneity on this time scale, including inhomogeneous sources such as traffic on major roadways and vertical mixing (with an adiabatic lapse rate of -9 °C/km) (Lu et al., 2019). Further, Large Eddy Simulations of a megacity (Hong Kong) confirm widespread eddies with spatial scales of tens to hundreds of meters and velocity perturbations of order 1 m/s (Letzel et al., 2012). This is consistent with the sustained inhomogeneity required for the rapid growth we demonstrate here, shown conceptually in Fig. 3.11a. It is thus likely that dense urban conditions will typically include persistent inhomogeneities maintaining supersaturation of nitric acid and ammonia with sufficient magnitude to drive rapid growth, as indicated by the blue "shell" in Fig. 3.11b. Our thermodynamic models support the phenomenology of Fig. 3.11b as show in Fig. 3.11c and d, though the composition is likely to be an amorphous mixture of salts as shown in Fig. 3.6. Rapid growth may be sufficient for particles to grow from vulnerable sizes near 2.5 nm to more robust sizes above 10 nm. For example, repeated nucleation bursts with very rapid growth have been observed in the ammonia and nitric acid-rich Cabauw

site in the Netherlands during the EUCAARI campaign (Manninen et al., 2010).

It is common for chemical transport models to employ an equilibrium assumption for ammonium-nitrate partitioning, as on the timescale of low spatial resolution and long time steps characteristic of large-scale models, the ammonium-nitrate aerosol system should equilibrate with respect to the bulk sub-micron particles. Further, because rapid growth appears to be rate limited by formation of ammonium nitrate, the covariance of base and nitric acid sources and concentrations may be critical. Even typical megacity steady-state vapor concentrations fall somewhat above the green points in Fig. 3.10a (toward larger mixing ratios). For constant production rates, as temperature falls the ammonium-nitrate saturation lines shown in Fig. 3.10a will sweep from the upper right toward the lower left, moving the system from rough equilibrium for typical urban production and emission rates when it is warmer than about +5 °C to a sustained supersaturation when it is colder. Just as equilibrium organic condensation and partitioning results in under-estimated growth rates from organics in the boreal forest (Pierce et al., 2011), equilibrium treatments of ammonium-nitrate condensation will underestimate the role of nitric acid in nanoparticle growth, especially for inhomogeneous urban environments.

While the pure ammonium-nitrate nucleation rates in Fig. 3.10c are too slow to compete in urban new-particle formation, this mechanism may provide an important source of new particles in the relatively clean and cold upper free troposphere, where ammonia can be convected from the continental boundary layer (Ge et al., 2018) and abundant nitric acid is produced by electrical storms (Höpfner et al., 2019). Theoretical studies have also suggested that nitric acid may serve as a chaperone to facilitate sulfuric-acid–ammonia nucleation (Liu et al., 2018). Larger (60-1000 nm) particles consisting largely of ammonium nitrate, along with more than 1 ppbv of ammonia, have been observed by satellite in the upper troposphere in the Asian Monsoon Anticyclone (Höpfner et al., 2019) and abundant 3-7 nm particles have been observed in situ in the Tropical Convective Region at low temperature and condensation sink (Williamson et al., 2019). While these particles are likely formed via nucleation, the mechanism is not yet known. However, our experiment under similar conditions shown in Fig. 3.1 demonstrates that it is plausible that pure ammonium-nitrate nucleation and/or rapid growth by ammonium-nitrate condensation contributes to these particles in the upper troposphere.

Our results indicate that nitric acid and ammonia condensation is likely to be an important new mechanism for particle formation and growth in the cold upper free

troposphere, as supported by recent observations (Höpfner et al., 2019; Williamson et al., 2019). Furthermore, this process could help to explain how newly-formed particles survive scavenging losses in highly polluted urban environments (Kulmala et al., 2017). As worldwide pollution controls continue to reduce SO_2 emissions sharply, the importance of NO_x and nitric acid for new-particle formation is likely to increase. In turn, controls on NO_x and ammonia emissions may become increasingly important, especially for reduction of urban smog.

Acknowledgement

We thank the European Organization for Nuclear Research (CERN) for supporting CLOUD with technical and financial resources and for providing a particle beam from the CERN Proton Synchrotron. This research has received funding from the US National Science Foundation (NSF; grant numbers AGS1602086, AGS1801329 and AGS-1801280); the NASA graduate fellowship (grant number NASA-NNX16AP36H); the Swiss National Science Foundation (grant numbers 200021169090, 200020172602 and 20FI20172622); the European Community (EC) Seventh Framework Programme and the European Union (EU) H2020 programme (Marie Skłodowska Curie ITN CLOUD-TRAIN grant number 316662 and CLOUD-MOTION grant number 764991); a European Research Council (ERC) Advanced Grant (number ATM-GP 227463); an ERC Consolidator Grant (NANODYNAMITE 616075); an ERC Starting Grant (GASPARCON 714621), the Academy of Finland (grants 306853, 296628, 316114 and 299544); the Academy of Finland Center of Excellence programme (grant 307331); the German Federal Ministry of Education and Research (CLOUD-12 number 01LK1222A and CLOUD-16 number 01LK1601A); the Knut and Alice Wallenberg Foundation Wallenberg Academy Fellow project AtmoRemove (grant number 2015.0162); the Austrian Science Fund (grant number P 27295-N20); the Portuguese Foundation for Science and Technology (grant number CERN/FIS-COM/0014/2017); and the Presidium of the Russian Academy of Sciences ('High energy physics and neutrino astrophysics' 2015). The FIGAERO-CIMS was supported by a Major Research Instrumentation (MRI) grant for the US NSF (AGS-1531284), and by the Wallace Research Foundation. We thank H. Cawley for producing Fig. 3.11a.

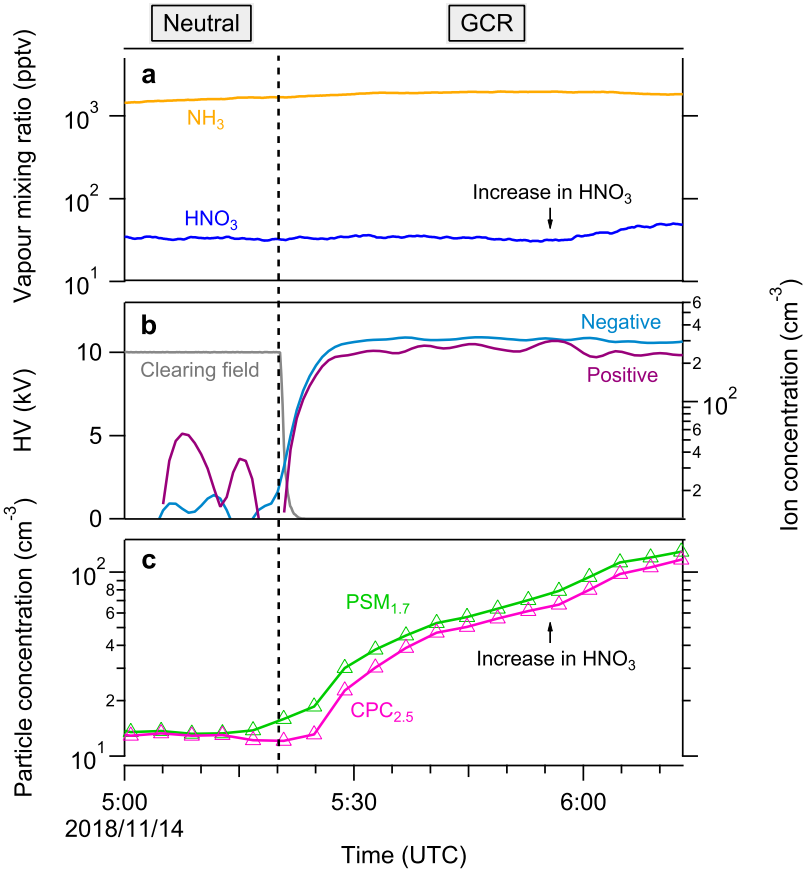

Figure 3.1: Example of a typical measurement sequence of nucleation purely from nitric acid and ammonia with no sulfuric acid (measured as $< 5 \times 10^4$ cm^{-3} or 2×10^{-3} pptv) as a function of coordinated universal time (UTC), at 60 % relative humidity and -25 °C. a) Gas-phase ammonia and nitric acid mixing ratios. The run started with injecting the nitric acid and ammonia flow into the chamber to reach chosen steady-state values near 30 pptv and 1500 pptv, respectively. The nitric acid flow was increased at 5:53, 14 Nov. 2018 to prove consistency. b) Clearing field voltage and ion concentrations. Primary ions were formed from galactic cosmic rays (GCR). The clearing field high voltage (HV) was used to sweep out small ions at the beginning of the run, and turned off at 05:21, 14 Nov. 2018 to allow the ion concentration to build up to a steady state between GCR production and wall deposition. c) Particle concentrations at two different sizes. Particles formed slowly in the chamber under "neutral" conditions with the HV clearing field on and thus without ions present. The presence of ions (GCR condition) caused a sharp increase in the particle number concentration by about one order of magnitude, with a slower approach to steady state because of the longer wall deposition time constant for the larger particles. Particle numbers rose again with rising nitric acid.

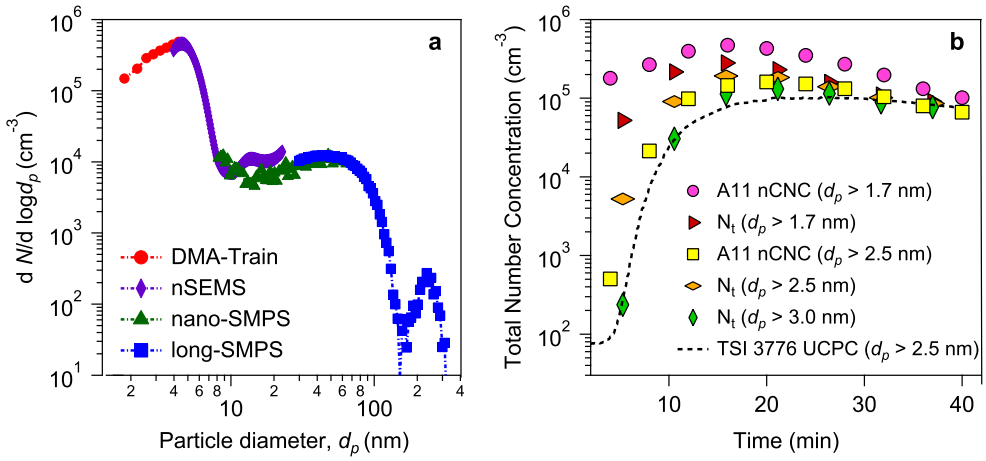

Figure 3.2: Combined particle-size distribution and total concentrations from four particle characterization instruments. (a) Combined size distributions, $n_N^\circ\left(d_p\right) = dN/d\log\ d_p$, from four electrical mobility particle size spectrometers of different, but overlapping, detection ranges. The DMA-Train, nSEMS and nano-SMPS data were averaged every five minutes to coordinate with the long-SMPS scanning time resolution. The tail of the size distribution of large particles outside the detection range was extrapolated by fitting a lognormal distribution. (b) Comparison of the integrated number concentrations from the combined size distributions in (a) with total number counts obtained from fixed cut-off size condensation particle counters. We obtained the total number concentration of particles, $N_t(d_{p_0})$, above a cut-off size, d_{p_0}, by integrating the particle size distribution using (Seinfeld and Pandis, 2006): $N_t = \int_{d_{p_0}}^{\infty}\left\{n_N\left(d_p\right) \times \eta_{\mathrm{UCPC}}\right\}\mathrm{d}d_p$, applying the size-dependent detection efficiency, η_{UCPC} (Mordas et al., 2008), to adjust the integrated total number concentration. We plot the total number concentrations for three different cut-off sizes: $d_{p_0} = 1.7, 2.5,$ and 3.0 nm, obtained every 5 minutes, with colored symbols as shown in the legend. We also plot measured total number concentrations from two instruments: the Airmodus A11 nCNC-system at nominal cut-off sizes $d_{p_0} = 1.7$ and 2.5 nm and a TSI 3776 UCPC with a nominal cut-off size $d_{p_0} = 2.5$ nm. The Airmodus A11 nCNC-system consists of an A10 PSM and an A20 CPC, which determined both the size distribution of 1-4 nm aerosol particles and the total number concentration of particles smaller than 1 μm (Lehtipalo et al., 2016). The TSI 3776 UCPC has a rapid response time and so rather than the 5-minute basis for the other points we plot the values from this instrument with a dashed curve.

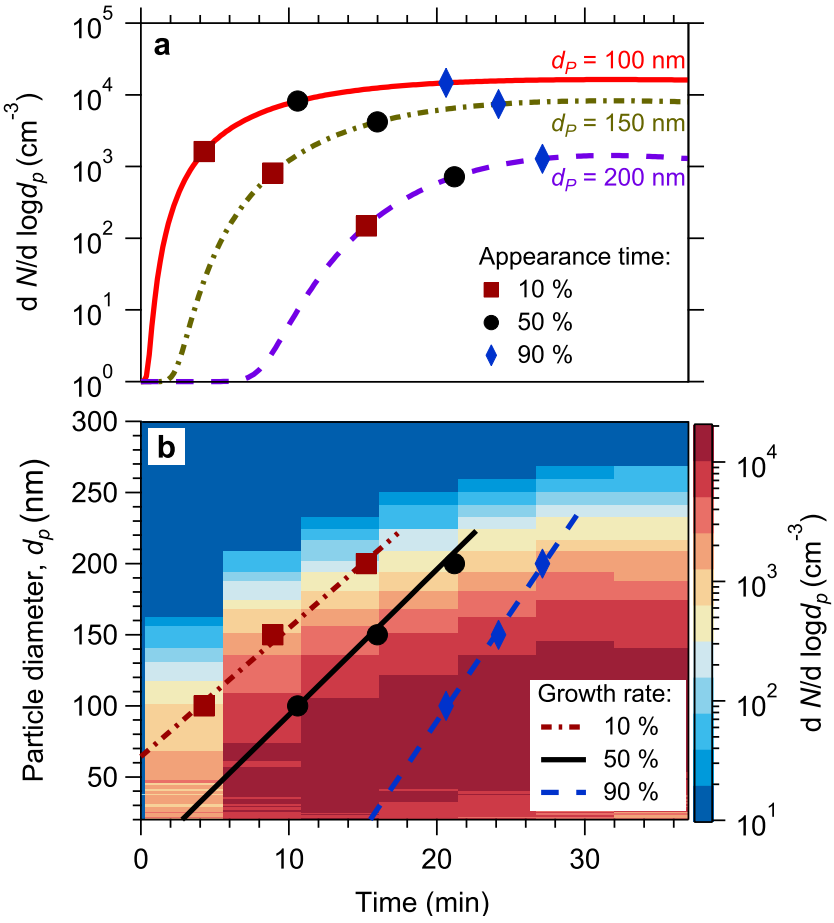

Figure 3.3: Determination of growth rate using appearance time method. (a) Logarithmic interpolated time-dependent growth profiles for particles of 100 nm, 150 nm, and 200 nm diameters. Three appearance times when particle number concentrations reached 10 %, 50 %, and 90 % of their maximum are labelled with different symbols for the three different diameters, respectively. (b) Growth rate calculation for a rapid growth event (same as Fig. 3.9) above the activation diameter. The growth rates, in nm h^{-1}, that we report in this work are the slopes of linear fits to the 50 % appearance times calculated from all sizes above the activation diameter (the slope of the solid black line and the black circles in (b)).

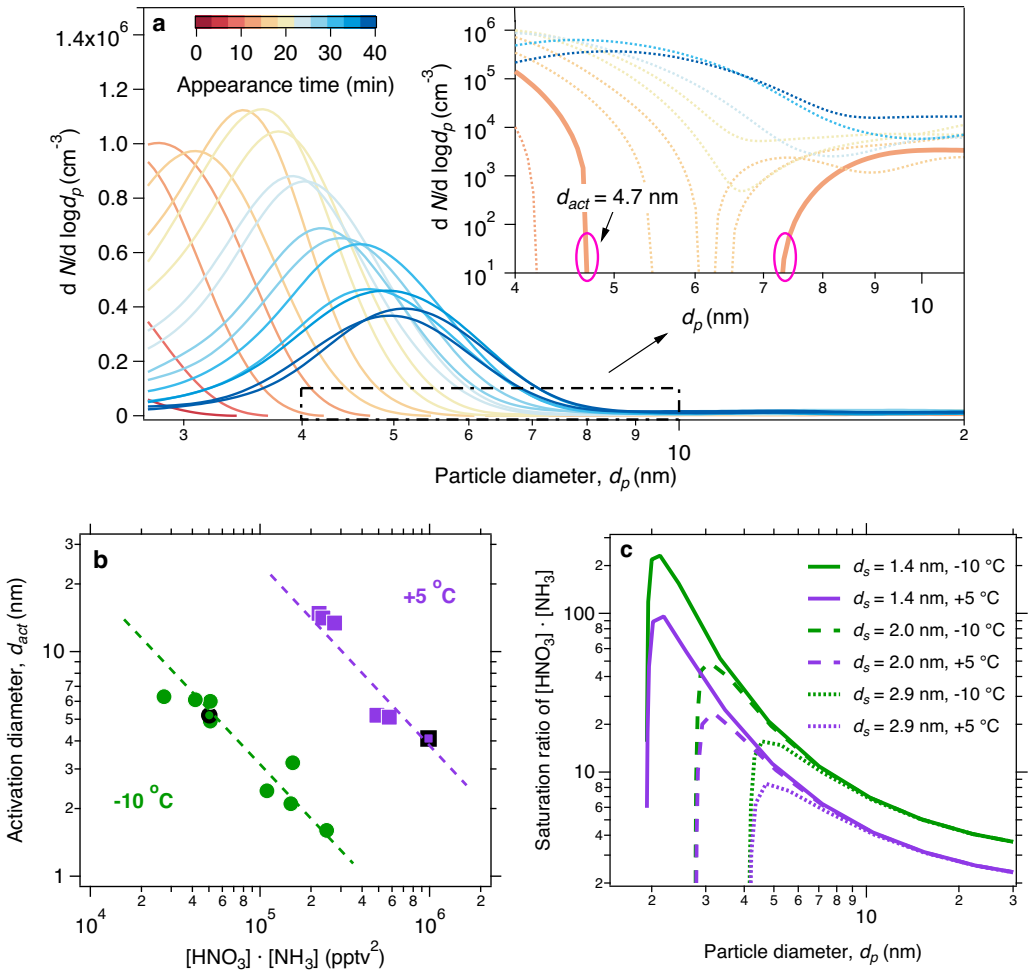

Figure 3.4: Activation diameter of newly-formed particles. (a) Determination of the activation diameter, d_{act}, from a rapid growth event at +5 °C, in the presence of nitric acid, ammonia, and sulfuric acid. The solid orange trace in the insert indicates the first size distribution curve that exhibited a clear bimodal distribution, which appeared roughly 7 minutes after nucleation. We define the activation diameter a the largest observed size of the smaller mode. In this case, d_{act} = 4.7 nm, which agrees well with the MABNAG simulation of ~ 4 nm under the same conditions as shown in Fig. 3.11. (b) Activation diameter versus vapor product. Measured activation diameters at a given temperature correlate inversely with the product of nitric acid and ammonia vapors, in a log-log space. Approximately 1 order of magnitude higher vapor product is required for the same d_{act} at +5 °C than at -10 °C because of the higher vapor pressure (faster dissociation) of ammonium nitrate when it is warmer. (c) Equilibrium particle diameter (d_{p}) at different saturation ratios of ammonium nitrate calculated according to nano-Köhler theory. Purple curves are for +5 °C and green curves are for -10 °C, as with all figures in this work. The line type shows the diameter of the seed particle (d_{s}). The maximum of each curve corresponds to the activation diameter (d_{act}). A higher supersaturation is required for activation at lower temperature.

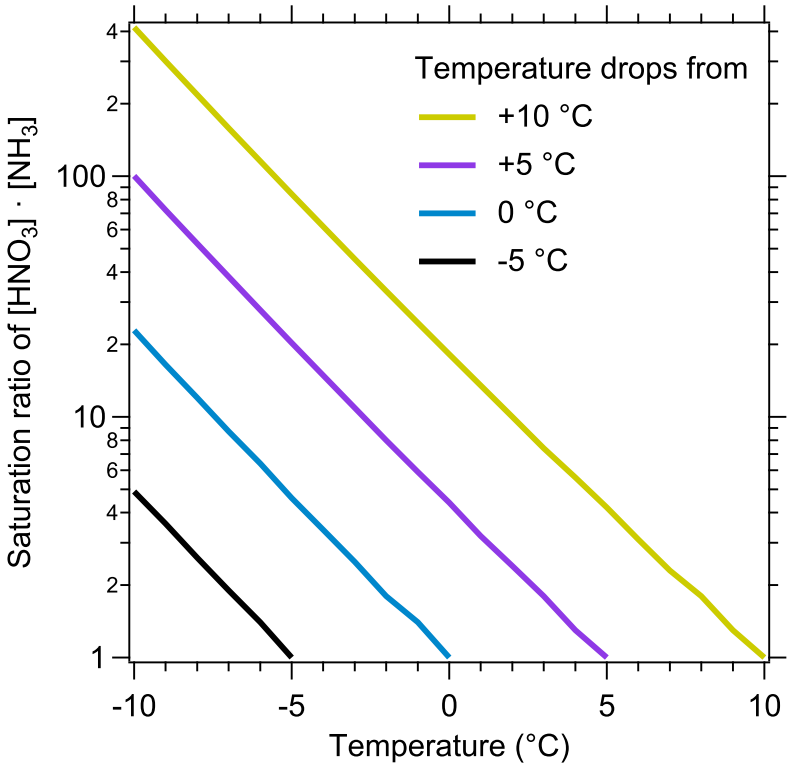

Figure 3.5: Saturation ratio as a function of temperature. At constant nitric acid and ammonia, a decline in temperature leads to an exponential increase in the saturation ratio of ammonium nitrate, given by the product of nitric acid and ammonia vapor concentration. With an adiabatic lapse rate of -9 °C/km during adiabatic vertical mixing, upward transport of a few hundred meters alone is sufficient for a saturated nitric acid and ammonia air parcel to reach the saturation ratio capable of triggering rapid growth at a few nanometers.

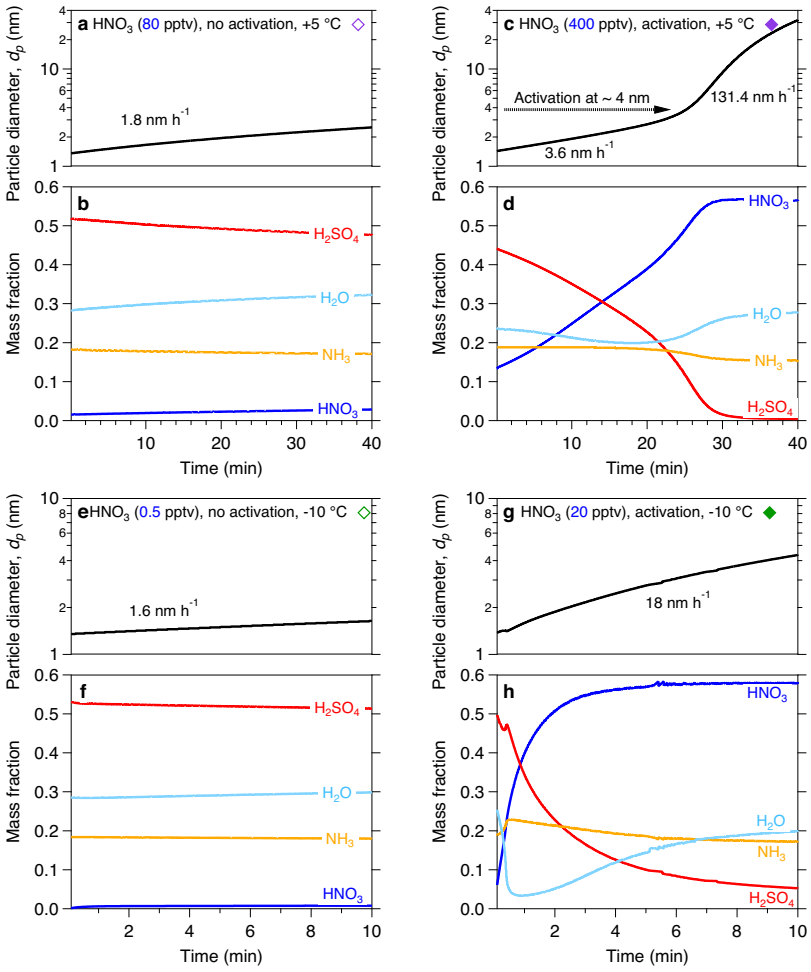

Figure 3.6: Comparison of growth rates and chemical composition in four simulations at +5 °C and -10 °C with the thermodynamic model MABNAG. The simulation points are shown in Fig 3.10a) with diamonds as indicated (open for non activating, filled for activating). Top panels (a, c, e and g) show temporal evolution of the particle diameter. Lower panels (b, d, f and h) show temporal evolution of the particle-phase chemical composition. The left-hand column (a, b and e, f) shows simulations without activation. The right-hand column (c, d and g, h) shows simulations with activation. We set the HNO_3 mixing ratios at 80 pptv and 400 pptv with 1500 pptv NH_3 at +5 °C, and set the HNO_3 mixing ratios at 20 pptv and 0.5 pptv with 1500 pptv NH_3 at -10 °C, to simulate unsaturated (a, b and e, f) and supersaturated (c, d and g, h) conditions, respectively. All other conditions were held constant for the simulations, with the $[H_2SO_4]$ at 2×10^7 cm^{-3} and relative humidity at 60 %. Activation corresponds to a rapid increase in the nitric acid (nitrate) mass fraction; the simulations for activation conditions suggest that water activity may be an interesting variable influencing activation behavior. The activated model results (c, d and g, h) confirm that supersaturated nitric acid and ammonia lead to rapid growth of nanoparticles. The simulated activation diameter at +5 °C is ~ 4 nm, similar to that from the chamber experiment (4.7 nm, Fig 3.10a); at -10 °C the simulated activation diameter is < 2 nm, smaller than observed.

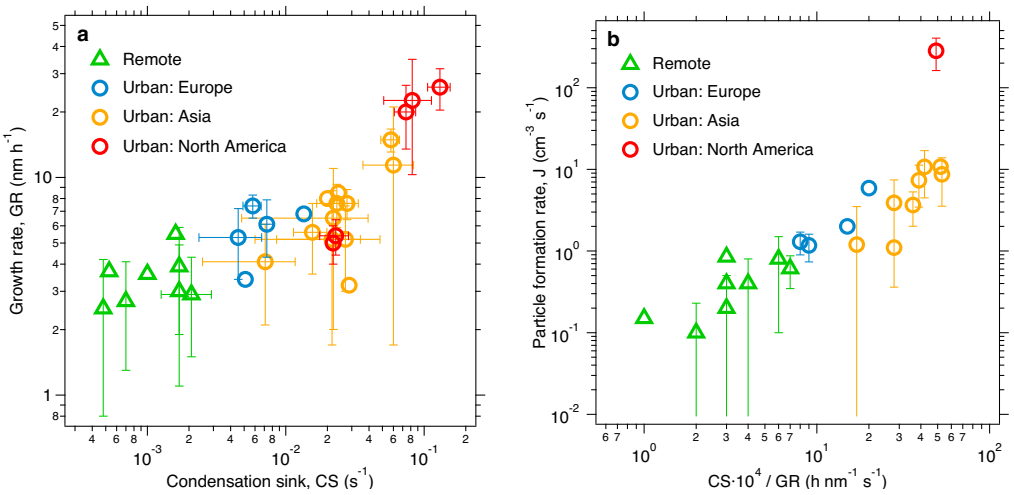

Figure 3.7: New-particle formation events observed in various remote and urban environments (see Table 3.3 for a complete set of references). (a) Growth rates (GR) versus condensation sink (CS) showing both the GR and CS are higher in polluted urban environments than in other environments. (b) Particle formation rates (J) versus a measure of particle loss via coagulation (CS·10^4/GR, similar to the the McMurry L parameter) showing high new-particle formation rates in urban conditions where the condensation sinks were so high compared to the growth rate that survival of nucleated particles should be very low. J and GR were calculated over the size range from a few nm to over 20 nm, except for J at Shanghai Xiao et al., 2015 and Tecamac Iida et al., 2008, which were calculated from 3 to 6 nm. The bars indicate 1σ total errors.

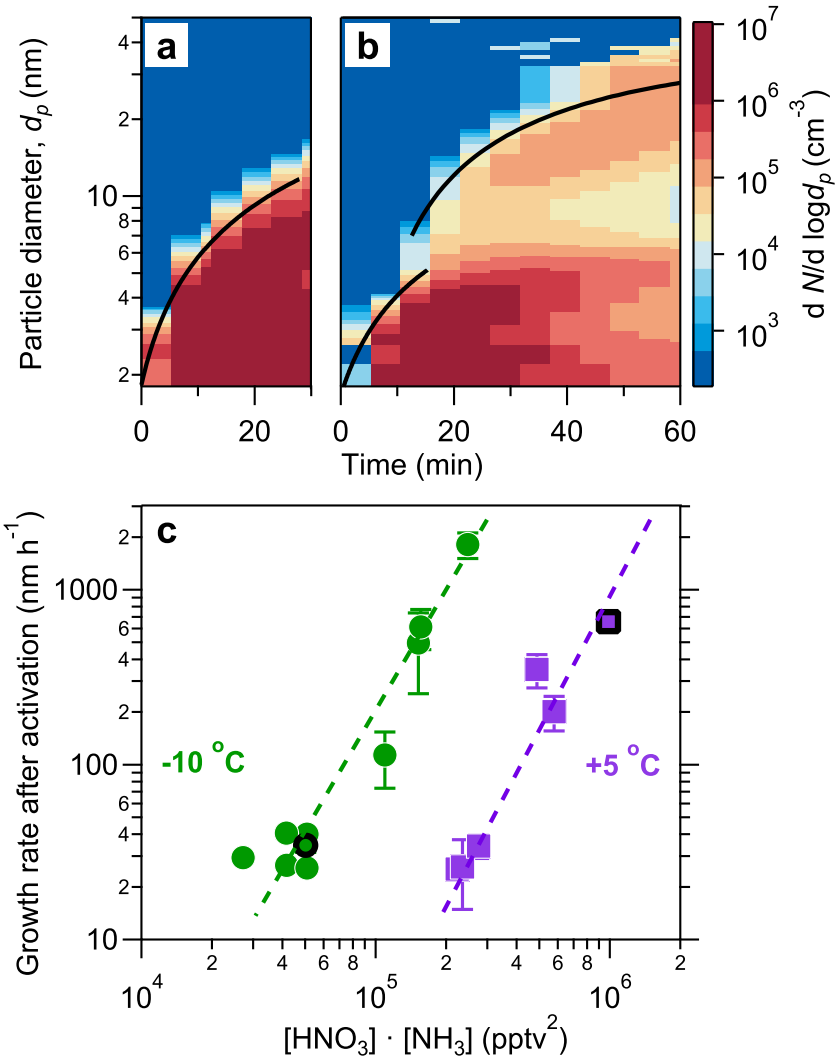

Figure 3.8: Rapid growth events observed in the CERN CLOUD chamber. (a) Particle nucleation and growth at -10 °C with a mixture of 0.44 pptv sulfuric acid and 1915 pptv ammonia at 60 % RH. Particles form and grow to roughly 10 nm in 30 min. The black curve shows the linear fit to the 50 % appearance times. (b) Particle formation and growth under identical conditions but with the addition of 24 pptv of nitric acid vapor formed via NO_2 oxidation. Once particles reach roughly 5 nm they experience rapid growth to much larger sizes, reaching more than 30 nm in 45 min. (c) Observed growth rates after activation versus the product of measured nitric acid and ammonia levels at +5 and -10 °C. The point corresponding to (b) is a black bordered green circle and the point corresponding to Fig. 3.9 is a black bordered purple square. Growth rates at a given vapor product are significantly faster at -10 °C than at +5 °C, consistent with semi-volatile condensation that is rate-limited by ammonium nitrate formation. Error bars are 95 % confidence limits on the fitting coefficients used to determine growth rates. The overall systematic scale uncertainty of ± 10 % on NH_3 mixing ratio and ± 25 % on HNO_3 mixing ratio are not shown.

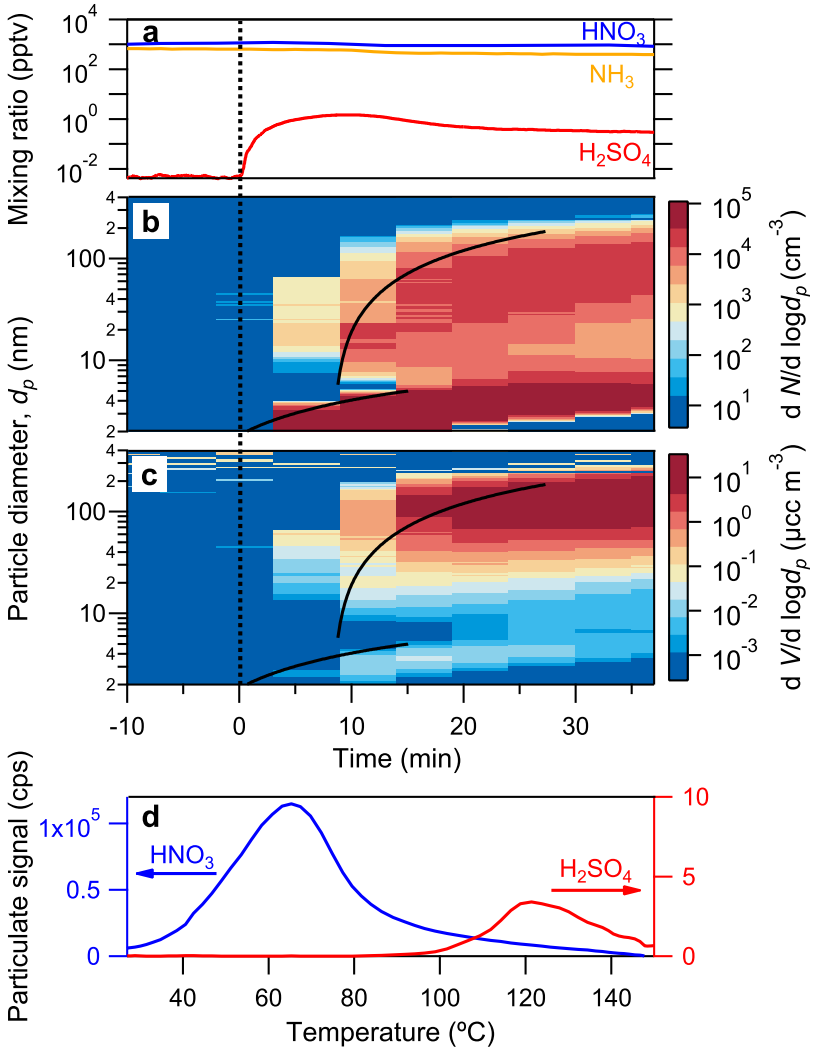

Figure 3.9: Chemical composition during a rapid growth event at +5 °C and 60 % RH, indicated in Fig. 3.8 with a black outlined purple square. (a) Gas-phase nitric acid, ammonia and sulfuric acid mixing ratios versus time in an event initiated by SO_2 oxidation, with constant nitric acid and ammonia. (b) Particle number distributions versus time showing a clean chamber, followed by nucleation after sulfuric acid formation and rapid growth once particles reach 2.3 nm. Black curves are the linear fit to the 50 % appearance times. (c) Particle volume distributions from the same data, showing that 200 nm particles dominate the mass after 15 minutes. (d) FIGAERO thermogram from a 30 minute filter sample after rapid growth. Particle composition is dominated by nitrate with a core of sulfate, consistent with rapid growth by ammonium nitrate condensation on an ammonium sulfate (or bisulfate) core (note the different y scales; the instrument is not sensitive to ammonia). A thermogram from just before the formation event shows no signal from either nitrate or sulfate, indicating that vapor adsorption did not interfere with the analysis.

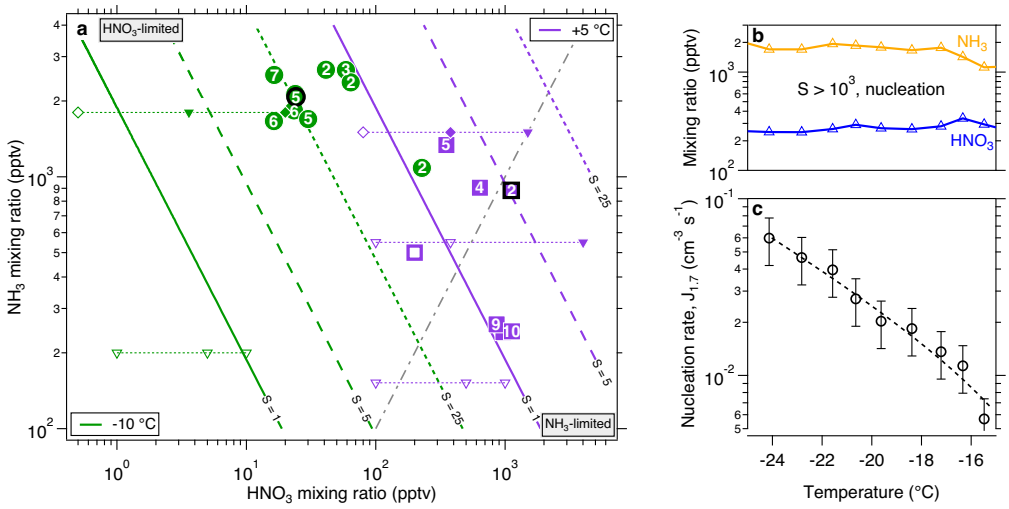

Figure 3.10: Phase space for rapid growth and nucleation. (a) Ammonium nitrate saturation ratios versus gas-phase nitric acid and ammonia at 60 % RH. Solid (slope = -1) lines are S = 1 (bold), 5 (dashed), and 25 (dotted) at -10 °C (green) and +5 °C (purple). The slope = +1 dot-dashed gray line indicates a 1:1 ammonia:nitric-acid stoichiometry; the phase space to the upper left is nitric-acid limited. Observed activation diameters for measured nitric acid – ammonia pairs are plotted as numbers inside solid circle and square symbols; open symbols show no activation. Activation only occurs for $S > 1$ and the activation diameter decreases as S increases. Points for MABNAG simulations are shown with open triangles for no activation and filled triangles for activation; simulations indicated with diamonds are shown in detail in Fig. 3.11 and Fig. 3.6. Points for runs shown in Figs 3.8 and 3.9 are emphasized with a thick black outline. (b) Ammonia and nitric acid vapor during a pure ammonium nitrate nucleation scan from -16 to -24 °C. (c) Particle formation rates ($J_{1.7}$) during the nucleation scan, showing a strong inverse relationship with temperature at constant HNO_3 and NH_3, with $H_2SO_4 < 0.002$ pptv and RH starting at 60 % and ending at 40 %. The bars indicate 30 % estimated total error on the nucleation rates, although the overall systematic scale uncertainties of ± 10 % on NH_3 mixing ratio and ± 25 % on HNO_3 mixing ratio are not shown.

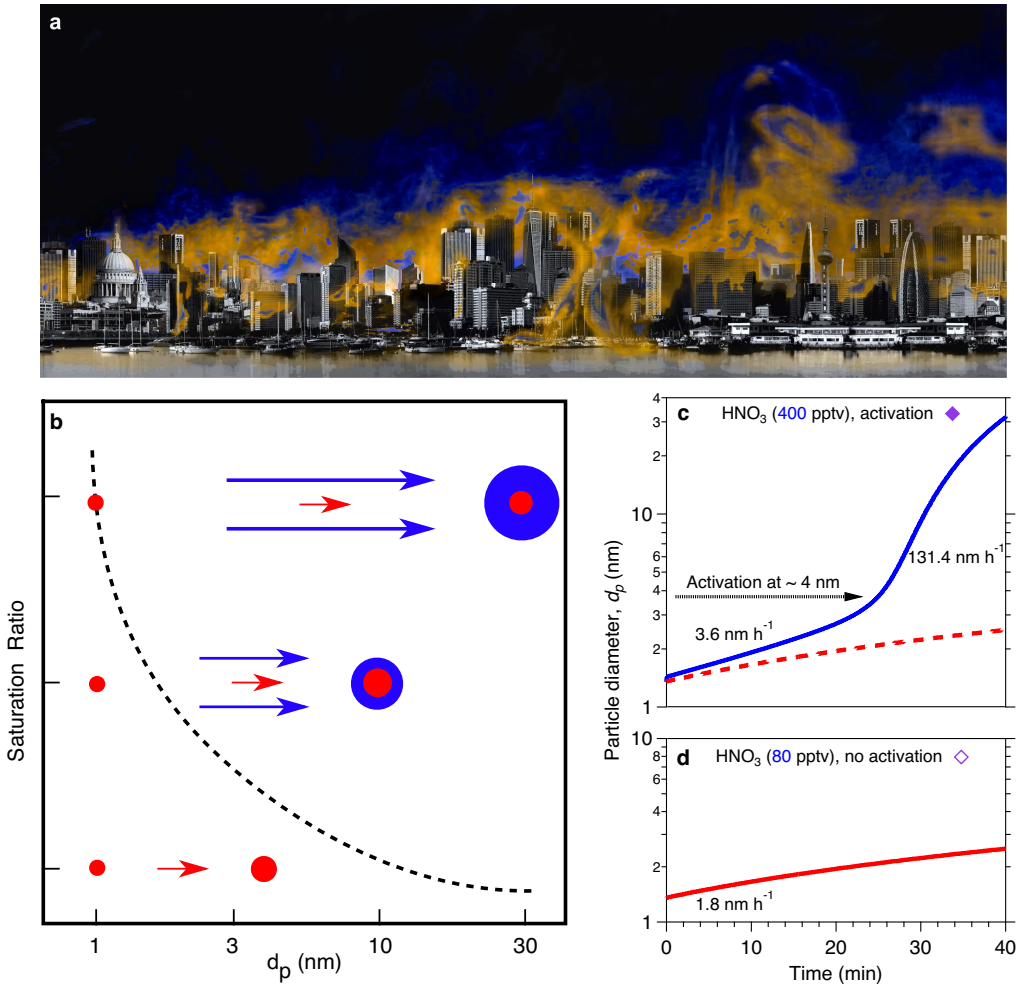

Figure 3.11: Conditions for rapid growth. Persistent supersaturations of ammonia and nitric acid with respect to ammonium nitrate will be sustained by inhomogeneity for high source-strength urban conditions. This will be sufficient to accelerate particle growth in the 1-10 nm range, where survival is threatened by high coagulation surface area from high pollution. (a) Concept for urban conditions, where inhomogeneity in ammonia and nitric acid vapor concentrations as well as temperature are caused by non-uniform sources and large-scale eddies. (b) Particles nucleate and grow slowly as (base stabilized) sulfate (red). Activation size (dashed curve corresponding to x-axis) depends on the ammonium-nitrate saturation ratio (qualitatively on y axis). Available gas-phase nitric acid can exceed sulfuric acid by a factor of 1000, so modest supersaturation drives rapid growth (blue) above an activation diameter determined by particle curvature (the Kelvin term, indicated as a dashed curve). (c,d) Monodisperse thermodynamic growth calculations (MABNAG) for high and low ammonium-nitrate saturation ratios corresponding to (b) and also the closed and open diamonds towards the upper right in Fig. 3.10a. For a saturation ratio near 4, activation is predicted to occur near 4 nm, consistent with our observations.

References

J. An et al. (May 2015). "Characteristics of new particle formation events in Nanjing, China: Effect of water-soluble ions". en. In: *Atmospheric Environment* 108, pp. 32–40. ISSN: 1352-2310. DOI: 10.1016/j.atmosenv.2015.01.038.

J. S. Apte et al. (2018). "Ambient $PM_{2.5}$ Reduces Global and Regional Life Expectancy". In: *Environmental Science & Technology Letters* 5.9, pp. 546–551. DOI: 10.1021/acs.estlett.8b00360.

O. Boucher et al. (2013). "Clouds and Aerosols". In: *Climate Change 2013: The Physical Science Basis. Contribution of Working Group I to the Fifth Assessment Report of the Intergovernmental Panel on Climate Change*. Ed. by T. Stocker et al. Cambridge, United Kingdom and New York, NY, USA: Cambridge University Press. Chap. 7, pp. 571–658. ISBN: ISBN 978-1-107-66182-0. DOI: 10.1017/CBO9781107415324.016.

M. Breitenlechner et al. (2017). "PTR3: An Instrument for Studying the Lifecycle of Reactive Organic Carbon in the Atmosphere". In: *Analytical Chemistry* 89, pp. 5824–5831. DOI: 10.1021/acs.analchem.6b05110.

G. Chen et al. (Dec. 2018). "Circulation responses to regional aerosol climate forcing in summer over East Asia". In: *Climate Dynamics* 51.11, pp. 3973–3984. DOI: 10.1007/s00382-018-4267-3.

S. L. Clegg and J. H. Seinfeld (2006a). "Thermodynamic models of aqueous solutions containing inorganic electrolytes and dicarboxylic acids at 298.15 K. 1. The acids as nondissociating components". In: *The Journal of Physical Chemistry A* 110.17, pp. 5692–5717. DOI: 10.1021/jp056149k.

– (2006b). "Thermodynamic models of aqueous solutions containing inorganic electrolytes and dicarboxylic acids at 298.15 K. 2. Systems including dissociation equilibria". In: *The Journal of Physical Chemistry A* 110.17, pp. 5718–5734. DOI: 10.1021/jp056150j.

M. Dal Maso et al. (Oct. 2005). "Formation and growth of fresh atmospheric aerosols: Eight years of aerosol size distribution data from SMEAR II, Hyytiälä, Finland". In: *Boreal Environment Research* 10.5, pp. 323–336. URL: http://www.borenv.net/BER/pdfs/ber10/ber10-323.pdf.

M. Dal Maso et al. (Jan. 2007). "Aerosol size distribution measurements at four Nordic field stations: identification, analysis and trajectory analysis of new particle formation bursts". In: *Tellus B: Chemical and Physical Meteorology* 59.3. Publisher: Taylor & Francis _eprint: https://doi.org/10.1111/j.1600-0889.2007.00267.x, pp. 350–361. ISSN: null. DOI: 10.1111/j.1600-0889.2007.00267.x.

M. Dal Maso et al. (Apr. 2008). "Aerosol particle formation events at two Siberian stations inside the boreal forest". In: *Boreal Environment Research* 13.2. Publisher: Boreal Environment Research, pp. 81–92. ISSN: 12396095. DOI: 10.1007/978-1-4020-6475-3_166.

K. G. Denbigh and K. G. Denbigh (1981). *The principles of chemical equilibrium: with applications in chemistry and chemical engineering*. Cambridge University Press.

A. Dias et al. (2017). "Temperature uniformity in the CERN CLOUD chamber". In: *Aerosol Measurement Techniques* 10, pp. 5075–5088. DOI: 10.5194/amt-10-5075-2017.

J. Duplissy et al. (2016). "Effect of ions on sulfuric acid-water binary particle formation II: Experimental data and comparison with QC-normalized classical nucleation theory". In: *Journal of Geophysical Research Atmospheres* 212, pp. 1752–1775. DOI: 10.1002/2015JD023539.

F. Eisele and D. Tanner (1993). "Measurement of the gas phase concentration of H2SO4 and methane sulfonic acid and estimates of H2SO4 production and loss in the atmosphere". In: *Journal of Geophysical Research: Atmospheres* 98.D5, pp. 9001–9010. DOI: 0.1029/93JD00031.

J. Gao et al. (Jan. 2012). "Particle number size distribution and new particle formation: New characteristics during the special pollution control period in Beijing". en. In: *Journal of Environmental Sciences* 24.1, pp. 14–21. ISSN: 1001-0742. DOI: 10.1016/S1001-0742(11)60725-0.

M. Gautrois and R. Koppmann (1999). "Diffusion technique for the production of gas standards for atmospheric measurements". In: *Journal of Chromatography A* 848.1-2, pp. 239–249. DOI: 10.1016/S0021-9673(99)00424-0.

C. Ge et al. (2018). "A molecular perspective for global modeling of upper atmospheric NH3 from freezing clouds". In: *Proceedings of the National Academy of Sciences* 115.24, pp. 6147–6152. ISSN: 0027-8424. DOI: 10.1073/pnas.1719949115.

H. Gordon et al. (2017). "Causes and importance of new particle formation in the present-day and pre-industrial atmospheres". In: *Journal of Geophysical Research Atmospheres* 122, pp. 8739–8760. DOI: 10.1002/2017JD026844.

S. M. L. Hama et al. (Sept. 2017). "Sub-micron particle number size distribution characteristics at two urban locations in Leicester". en. In: *Atmospheric Research* 194, pp. 1–16. ISSN: 0169-8095. DOI: 10.1016/j.atmosres.2017.04.021.

A. Hamed et al. (Jan. 2007). "Nucleation and growth of new particles in Po Valley, Italy". English. In: *Atmospheric Chemistry and Physics* 7.2. Publisher: Copernicus GmbH, pp. 355–376. ISSN: 1680-7316. DOI: 10.5194/acp-7-355-2007.

E. Herrmann et al. (Feb. 2014). "Aerosols and nucleation in eastern China: first insights from the new SORPES-NJU station". en. In: *Atmospheric Chemistry and Physics* 14.4, pp. 2169–2183. ISSN: 1680-7375. DOI: 10.3929/ethz-b-000081840.

M. Höpfner et al. (2019). "Ammonium nitrate particles formed in upper troposphere from ground ammonia sources during Asian monsoons". In: *Nature Geoscience* 12.8, pp. 608–612. DOI: 10.1038/s41561-019-0385-8.

T. Hussein et al. (Jan. 2008). "Observation of regional new particle formation in the urban atmosphere". In: *Tellus B: Chemical and Physical Meteorology* 60.4. Publisher: Taylor & Francis _eprint: https://doi.org/10.1111/j.1600-0889.2008.00365.x, pp. 509–521. ISSN: null. DOI: 10.1111/j.1600-0889.2008.00365.x.

K. Iida et al. (2006). "Contribution of ion-induced nucleation to new particle formation: Methodology and its application to atmospheric observations in Boulder, Colorado". In: *Journal of Geophysical Research: Atmospheres* 111.D23. DOI: 10.1029/2006JD007167.

K. Iida et al. (2008). "Estimating nanoparticle growth rates from size-dependent charged fractions: Analysis of new particle formation events in Mexico City". en. In: *Journal of Geophysical Research: Atmospheres* 113.D5. DOI: 10.1029/2007JD009260.

T. Jokinen et al. (2012). "Atmospheric sulphuric acid and neutral cluster measurements using CI-APi-TOF". In: *Atmospheric Chemistry and Physics* 12.9, pp. 4117–4125. DOI: 10.5194/acp-12-4117-2012.

H. Junninen et al. (2010). "A high-resolution mass spectrometer to measure atmospheric ion composition". In: *Atmospheric Measurement Techniques* 3.4, pp. 1039–1053. DOI: 10.5194/amt-3-1039-2010.

Z. Jurányi et al. (2011). "A 17 month climatology of the cloud condensation nuclei number concentration at the high alpine site Jungfraujoch". In: *Journal of Geophysical Research: Atmospheres* 116.D10. DOI: 10.1029/2010JD015199.

V. P. Kanawade et al. (Sept. 2014). "Infrequent occurrence of new particle formation at a semi-rural location, Gadanki, in tropical Southern India". en. In: *Atmospheric Environment* 94, pp. 264–273. ISSN: 1352-2310. DOI: 10.1016/j.atmosenv.2014.05.046.

V.-M. Kerminen and M. Kulmala (2002). "Analytical formulae connecting the "real" and the "apparent" nucleation rate and the nuclei number concentration for atmospheric nucleation events". In: *Journal of Aerosol Science* 33.4, pp. 609–622. DOI: 10.1016/S0021-8502(01)00194-X.

J. Kirkby et al. (Aug. 2011). "Role of sulphuric acid, ammonia and galactic cosmic rays in atmospheric aerosol nucleation". In: *Nature* 476.7361, pp. 429–433. ISSN: 0028-0836. DOI: 10.1038/nature10343.

J. Kirkby et al. (2016). "Ion-induced nucleation of pure biogenic particles". In: *Nature* 530, pp. 521–526. DOI: 10.1038/nature17953.

M. Komppula et al. (2003). “Observations of new particle formation and size distributions at two different heights and surroundings in subarctic area in northern Finland”. In: *Journal of Geophysical Research: Atmospheres* 108.D9. DOI: 10.1029/2002JD002939.

J. Kontkanen et al. (2018). “Exploring the potential of nano-Köhler theory to describe the growth of atmospheric molecular clusters by organic vapors using cluster kinetics simulations”. In: *Atmospheric Chemistry and Physics* 18.18, pp. 13733–13754. DOI: 10.5194/acp-18-13733-2018.

C. Kuang et al. (2009). “Determination of cloud condensation nuclei production from measured new particle formation events”. In: *Geophysical Research Letters* 36.9. DOI: 10.1029/2009GL037584.

M. Kulmala et al. (2017). “Atmospheric gas-to-particle conversion: why NPF events are observed in megacities?” In: *Faraday Discuss.* 200, pp. 271–288. DOI: 10.1039/C6FD00257A.

M. Kulmala et al. (2013). “Direct Observations of Atmospheric Aerosol Nucleation”. In: *Science* 339.6122, pp. 943–946. DOI: 10.1126/science.1227385.

A. Kürten et al. (2011). “Performance of a corona ion source for measurement of sulfuric acid by chemical ionization mass spectrometry”. In: *Atmospheric Measurement Techniques* 4.3, pp. 437–443. DOI: 10.5194/amt-4-437-2011.

K. Lehtipalo et al. (May 2016). “The effect of acid–base clustering and ions on the growth of atmospheric nano-particles”. en. In: *Nature Communications* 7.1. Number: 1 Publisher: Nature Publishing Group, pp. 1–9. ISSN: 2041-1723. DOI: 10.1038/ncomms11594.

K. Lehtipalo et al. (2018). “Multi-component new particle formation from sulfuric acid, ammonia and biogenic vapors”. In: *Science Advances* 4, pp. 1–9. DOI: 10.1126/sciadv.aau5363.

M. O. Letzel et al. (Dec. 2012). “LES case study on pedestrian level ventilation in two neighbourhoods in Hong Kong”. In: *Meteorologische Zeitschrift* 21.6, pp. 575–589. DOI: 10.1127/0941-2948/2012/0356.

L. Liu et al. (2018). “The role of nitric acid in atmospheric new particle formation”. In: *Physical Chemistry Chemical Physics* 20, pp. 17406–17414. DOI: 10.1039/C8CP02719F.

F. D. Lopez-Hilfiker et al. (2014). “A novel method for online analysis of gas and particle composition: description and evaluation of a Filter Inlet for Gases and AEROsols (FIGAERO)”. In: *Atmospheric Measurement Techniques* 7.4, pp. 983–1001. DOI: 10.5194/amt-7-983-2014.

K. Lu et al. (Aug. 2019). “Fast photochemistry in wintertime haze: Consequences for pollution mitigation strategies.” In: *Environmental Science & Technology*. DOI: 10.1021/acs.est.9b02422.

H. Mai and R. C. Flagan (Oct. 2018). "Scanning DMA Data Analysis I. Classification Transfer Function". In: *Aerosol Science and Technology*, pp. 1–40. DOI: 10.1080/02786826.2018.1528005.

H. Mai et al. (Oct. 2018). "Scanning DMA data analysis II. Integrated DMA-CPC instrument response and data inversion". In: *Aerosol Science and Technology*, pp. 1–35. DOI: 10.1080/02786826.2018.1528006.

H. Man et al. (June 2015). "Comparison of Daytime and Nighttime New Particle Growth at the HKUST Supersite in Hong Kong". In: *Environmental Science & Technology* 49.12. Publisher: American Chemical Society, pp. 7170–7178. ISSN: 0013-936X. DOI: 10.1021/acs.est.5b02143.

H. E. Manninen et al. (2010). "EUCAARI ion spectrometer measurements at 12 European sites – analysis of new particle formation events". In: *Atmospheric Chemistry and Physics* 10.16, pp. 7907–7927. DOI: 10.5194/acp-10-7907-2010.

P. H. McMurry (1980). "Photochemical aerosol formation from SO_2: A theoretical analysis of smog chamber data". In: *Journal Colloid and Interface Science* 78, pp. 513–527. DOI: 10.1016/0021-9797(80)90589-5.

P. H. McMurry et al. (2005). "A criterion for new particle formation in the sulfur-rich Atlanta atmosphere". In: *Journal of Geophysical Research: Atmospheres* 110.D22. DOI: 10.1029/2005JD005901.

P. Mönkkönen et al. (Jan. 2005). "Measurements in a highly polluted Asian mega city: observations of aerosol number size distribution, modal parameters and nucleation events". In: *Atmospheric Chemistry and Physics* 5.1. Publisher: European Geosciences Union, pp. 57–66. DOI: 10.5194/acp-5-57-2005.

G. Mordas et al. (Jan. 2008). "On Operation of the Ultra-Fine Water-Based CPC TSI 3786 and Comparison with Other TSI Models (TSI 3776, TSI 3772, TSI 3025, TSI 3010, TSI 3007)". In: *Aerosol Science and Technology* 42.2, pp. 152–158. DOI: 10.1080/02786820701846252.

M. Mozurkewich (1993). "The dissociation constant of ammonium nitrate and its dependence on temperature, relative humidity and particle size". In: *Atmospheric Environment. Part A. General Topics* 27.2, pp. 261–270. DOI: 10.1016/0960-1686(93)90356-4.

W. Mui et al. (2017). "Design, simulation, and characterization of a radial opposed migration ion and aerosol classifier (ROMIAC)". In: *Aerosol Science and Technology* 51.7, pp. 801–823. DOI: 10.1080/02786826.2017.1315046.

C. D. O'Dowd et al. (2002). "Atmospheric particles from organic vapours". In: *Nature* 416.6880, pp. 497–498. DOI: 10.1038/416497a.

J. F. Peng et al. (Sept. 2014). "Submicron aerosols at thirteen diversified sites in China: size distribution, new particle formation and corresponding contribution to cloud condensation nuclei production". In: *Atmospheric Chemistry & Physics* 14, pp. 10249–10265. ISSN: 1680-7316. DOI: 10.5194/acp-14-10249-2014.

J. Pfeifer et al. (2019). "Measurement of ammonia, amines and iodine species using protonated water cluster chemical ionization mass spectrometry". In: *Atmospheric Measurement Techniques Discussions* 2019, pp. 1–36. DOI: 10.5194/amt-2019-215.

J. R. Pierce and P. J. Adams (Feb. 2007). "Efficiency of cloud condensation nuclei formation from ultrafine particles". In: *Atmospheric Chemistry and Physics* 7, pp. 1367–1379. DOI: 10.5194/acp-7-1367-2007.

J. R. Pierce et al. (2011). "Quantification of the volatility of secondary organic compounds in ultrafine particles during nucleation events". In: *Atmospheric Chemistry and Physics* 11, pp. 9019–9036. DOI: 10.5194/acp-11-9019-2011.

M. Pikridas et al. (Sept. 2015). "In situ formation and spatial variability of particle number concentration in a European megacity". In: *Atmospheric Chemistry & Physics* 15.17. Publisher: Copernicus Gesellschaft mbH, pp. 10219–10237. ISSN: 16807316. DOI: 10.5194/acp-15-10219-2015.

I. Riipinen et al. (July 2012). "The contribution of organics to atmospheric nanoparticle growth". English. In: *Nature Geoscience* 5.7, pp. 453–458. ISSN: 1752-0908. DOI: 10.1038/ngeo1499.

R. Schnitzhofer et al. (2014). "Characterisation of Organic Contaminants in the CLOUD Chamber at CERN". In: *Aerosol Measurement Techniques* 7, pp. 2159–2168. DOI: :10.5194/amt-7-2159-2014.

J. H. Seinfeld and S. N. Pandis (2006). *Atmospheric Chemistry and Physics*. 2nd ed. Hoboken, New Jersey: John Wiley & Sons.

C. O. Stanier et al. (2004). "Nucleation events during the Pittsburgh Air Quality Study: Description and relation to key meteorological, gas phase, and aerosol parameters". In: *Aerosol Science and Technology* 38, pp. 253–264. DOI: 10.1080/02786820390229570.

D. Stolzenburg et al. (2017). "A DMA-train for precision measurement of sub-10 nm aerosol dynamics". In: *Atmospheric Measurement Techniques* 10.4, pp. 1639–1651. DOI: 10.5194/amt-10-1639-2017.

D. Stolzenburg et al. (2018). "Rapid growth of organic aerosol nanoparticles over a wide tropospheric temperature range". In: *Proceedings of the National Academy of Sciences* 115, pp. 9122–9127. DOI: 10.1073/pnas.1807604115.

S. Takahama et al. (2004). "Modeling the diurnal variation of nitrate during the Pittsburgh Air Quality Study". In: *Journal of Geophysical Research: Atmospheres* 109, D16S06. DOI: 10.1029/2003JD004149.

J. Tröstl et al. (2015). “Fast and precise measurement in the sub-20nm size range using a Scanning Mobility Particle Sizer”. In: *Journal of Aerosol Science* 87, pp. 75–87. DOI: 10.1016/j.jaerosci.2015.04.001.

J. Tröstl et al. (2016). “The role of low-volatility organic compounds in initial particle growth in the atmosphere”. In: *Nature* 530, pp. 527–531. DOI: 10.1038/nature18271.

H. Vehkamäki et al. (2004). “Atmospheric particle formation events at Värriö measurement station in Finnish Lapland 1998-2002”. In: *Atmospheric Chemistry and Physics* 4.7, pp. 2015–2023. DOI: 10.5194/acp-4-2015-2004.

M. Wang et al. (2016). “Reactions of atmospheric particulate stabilized Criegee intermediates lead to high molecular weight aerosol components”. In: *Environmental Science & Technology* 50, pp. 5702–5710. DOI: 10.1021/acs.est.6b02114.

Z. B. Wang et al. (2013). “Characteristics of regional new particle formation in urban and regional background environments in the North China Plain”. In: *Atmospheric Chemistry and Physics* 13.24, pp. 12495–12506. DOI: 10.5194/acp-13-12495-2013. URL: https://www.atmos-chem-phys.net/13/12495/2013/.

A. Wiedensohler et al. (Mar. 2012). “Mobility particle size spectrometers: Harmonization of technical standards and data structure to facilitate high quality long-term observations of atmospheric particle number size distributions”. In: *Atmospheric Measurement Techniques* 5, pp. 657–685. DOI: 10.5194/amt-5-657-2012.

C. J. Williamson et al. (2019). “A large source of cloud condensation nuclei from new particle formation in the tropics”. In: *Nature* 574.7778, pp. 399–403. DOI: 10.1038/s41586-019-1638-9.

D. Wimmer et al. (2013). “Performance of diethylene glycol-based particle counters in the sub-3 nm size range”. In: *Atmospheric Measurement Techniques* 6.7, pp. 1793–1804. DOI: 10.5194/amt-6-1793-2013.

S. Xiao et al. (Feb. 2015). “Strong atmospheric new particle formation in winter in urban Shanghai, China”. English. In: *Atmospheric Chemistry and Physics* 15.4. Publisher: Copernicus GmbH, pp. 1769–1769. ISSN: 16807316. DOI: 10.5194/acp-15-1769-2015.

W. Xu et al. (2019). “Changes in Aerosol Chemistry From 2014 to 2016 in Winter in Beijing: Insights From High-Resolution Aerosol Mass Spectrometry”. In: *Journal of Geophysical Research: Atmospheres* 124.2, pp. 1132–1147. DOI: 10.1029/2018JD029245.

L. Yao et al. (2018). “Atmospheric new particle formation from sulfuric acid and amines in a Chinese megacity”. In: *Science* 361.6399, pp. 278–281. DOI: 10.1126/science.aao4839.

T. Yli-Juuti et al. (2013). “Model for acid-base chemistry in nanoparticle growth (MABNAG)”. In: *Atmospheric Chemistry and Physics* 13.24, pp. 12507–12524. DOI: 10.5194/acp-13-12507-2013.

H. Yu et al. (2016). “Nucleation and growth of sub-3\,nm particles in the polluted urban atmosphere of a megacity in China”. In: *Atmospheric Chemistry and Physics* 16.4, pp. 2641–2657. DOI: 10.5194/acp-16-2641-2016.

D. Yue et al. (Feb. 2018). “Characteristics of aerosol size distributions and new particle formation in the summer in Beijing”. In: *Journal of Geophysical Research: Atmospheres*. Publisher: John Wiley & Sons, Ltd. DOI: 10.1029/2008JD010894@10.1002/(ISSN)2169-8996.CARBS1.

Y. M. Zhang et al. (Jan. 2011). “Characterization of new particle and secondary aerosol formation during summertime in Beijing, China”. In: *Tellus B: Chemical and Physical Meteorology* 63.3, pp. 382–394. DOI: 10.1111/j.1600-0889.2011.00533.x.

Chapter 4

SIZE-DEPENDENT NITRATE PARTICLE GROWTH PARAMETERIZATION FOR LARGE-SCALE MODELING

W. Kong, A. Ranjithkumar, R. X. Ward, H. Gordon, R. Marten, M. Wang, the CLOUD Collaboration, K. Carslaw, J. H. Seinfeld, and R. C. Flagan (2020). "Size-Dependent Nitrate Particle Growth Parameterization for Large-Scale Modeling". In: *in prep*.

Abstract

Atmospheric new particle formation (NPF) and its subsequent growth is a major contributor to the global cloud condensation nuclei (CCN) budget and thus can affect cloud reflectivity and the Earth's albedo. The early growth of the freshly nucleated particles can determine their survival possibilities as sub-10 nm particles may be lost to pre-existing particles by coagulation. Ammonium nitrate was long thought contribute little to new particle formation and growth due to its semi-volatility. A recently discovered mechanism, thermodynamically driven by the condensation of nitric acid and ammonia, has suggested the potential of ammonium nitrate to facilitate extremely fast growth of nanoparticles in the size range where they are most vulnerable to coagulational loss, thereby increasing their survival probability. The Cosmics Leaving OUtdoor Droplets (CLOUD) experiments have shown that this mechanism may help to explain the high survival probability of nucleated clusters in urban haze conditions. In an effort to quantify its impact on a large scale, this rapid growth from gas-to-particle conversion has been modeled and parameterized as time- and size-dependent condensational growth. Compared to the conventional growth parameters used in large-scale modeling, this approach can provide additional details of transient aerosol dynamics. The derived parameters will be incorporated into the Global Model of Aerosol Processes (GLOMAP) to better constrain nanoparticle early growth and nitrate contribution to CCNs worldwide.

4.1 Introduction

New particle formation (NPF), which is a sudden burst of high concentrations of stable molecular clusters in the air, has been estimated to contribute to half of the global cloud condensation nuclei (CCN) budget (Merikanto et al., 2009; Gordon

et al., 2017). Atmospheric NPF often occurs in two stages, the initial formation of the critical nuclei from the gas-to-particle condensation of reactive vapors and the subsequent growth of these newly formed particles through condensation and coagulation (O'Dowd et al., 2002). Since freshly nucleated particles ($d_p < 10$ nm) are often vulnerable to scavenging loss, i.e., simultaneous capture and removal by coagulation with the pre-existing aerosol particles, the early growth of nanoparticles plays a crucial role in their survival probabilities and thus has a significant impact on CCN concentrations and properties (Kulmala and Kerminen, 2008; Stolzenburg et al., 2018).

Nanoparticles formed from atmospheric nucleation have been frequently observed at lower temperatures and are believed to affect CCN concentrations and properties globally (Lee et al., 2003; Kulmala et al., 2004; Zhang et al., 2012; Bianchi et al., 2016; Kerminen et al., 2018). It has been long believed that only atmospheric constituents with low vapor pressures are responsible for particle formation and early growth. For instance, sulfuric acid is considered to be the primary source of atmospheric nucleation (Sipilä et al., 2010) and ammonia (Ziereis and Arnold, 1986; Behera et al., 2013), iodine oxides (O'Dowd et al., 2002), and low-volatility organic compounds (Tröstl et al., 2016) are all thought to enhance the nucleation process and facilitate nanoparticle growth. Even though ammonium nitrate, formed from reactions between nitric acid and ammonia, is a major component of atmospheric aerosol particles (Russell et al., 1983), due to its semi-volatility, it is never thought to play an important role in nucleation and particle early growth. However, as nitric acid and ammonia can be one thousand times more abundant than sulfuric acid vapor in ambient conditions, even a small fractional supersaturation of gas-phase nitric acid and ammonia with respect to ammonium nitrate can drive fast nanoparticle growth (Wang et al., 2020). These extremely rapid growth events were observed in experiments conducted in the Cosmics Leaving OUtdoor Droplets (CLOUD) environmental chamber at the European Organization for Nuclear Research (CERN), with growth rates exceeding 100 nm/h under ambient conditions. This recently found mechanism has suggested the potential of ammonium nitrate facilitating atmospheric NPF and particle early growth, especially in the cold, upper troposphere, where nitric acid can be produced by electrical storms and anthropogenic emissions of ammonia can be convected from the surface. As a matter of fact, satellite observations have suggested that ammonium nitrate particles are ubiquitous in the upper troposphere during the Asian Monsoon Anticyclone; sub-10 nm nanoparticles containing nitrate and ammonium are also found in the tropical convective regions over both Pacific

and Atlantic oceans (Höpfner et al., 2019; Williamson et al., 2019). In addition, this mechanism can help to explain the survival of nucleated clusters to CCNs under polluted urban environment despite the presence of large amount of pre-existing particles, i.e., urban high condensation sink (CS).

In an effort to quantify the contribution of nitrate and ammonium on global CCN budget, a number of global models have been used to predict nitrate- and ammonium-containing aerosol particle concentrations and their direct or indirect radioactive effects (Liao and J. H. Seinfeld, 2005; Feng and Penner, 2007; Myhre et al., 2009; Xu and Penner, 2012). However, most of the modeling works have only focused on particles in the coarse mode, and even those that examined particles in fine mode have not yet evaluated the contribution of ammonium nitrate in particle formation and early growth. Compared to in situ or satellite observations, models tend to underestimate the magnitude of NPF and the subsequent growth of nanoparticles to CCN sizes (Williamson et al., 2019), and the discrepancy between measurements and simulations is even more significant for nitrate particles (Myhre et al., 2009). Many efforts have been dedicated to characterize particle growth, i.e., $\mathrm{d}d_\mathrm{p}/\mathrm{d}t$, and to better represent nanoparticle early growth in large-scale modeling. The detailed schemes of atmospheric nucleation and nanoparticle growth observed in laboratory are often too computationally expensive to include in large-scale modeling. As a result, particle growth was often oversimplified by parameterization using mathematical fitting without reference to the underlying physics. One common approach is to use the growth rates (in nm/h) derived from the appearance time method (Kulmala et al., 2012; Wang et al., 2020) to describe particle growth as a function of the relevant vapor concentrations (Gordon et al., 2017). However, this method only takes account of particle concentration at a certain time (at peak concentration or 50% of the peak concentration) and cannot fully capture the size- and time- dependent growth of newly formed particles. Others have attempted to better describe $\mathrm{d}d_\mathrm{p}/\mathrm{d}t$ by solving the aerosol general dynamic equation that helps to quantify the effect of sinks in the experiment in order to recover loss-free particle size distributions at an instant in time (Kuang et al., 2012; Pichelstorfer et al., 2018), but these methods are yet to be incorporated into large-scale modeling.

Here we verify the ambient significance of the rapid sub-10 nm nanoparticle growth from nitric acid and ammonia in urban conditions, where high growth rates help the survival of freshly nucleated particles under high CS. Given the potential contribution of this mechanism to global CCN budget, we propose a new approach to

parameterize this rapid nanoparticle growth based on the physics of gas-to-particle conversion. Because the thermodynamic driving force for this rapid growth is solely saturation ratio, and there is no complex organic reaction involved, the contribution of condensation on particle growth can be isolated and carefully examined. The derived parameters will be then incorporated into the Global Model of Aerosol Processes (GLOMAP, Spracklen et al., 2005). The new growth mechanism will bridge the gap between particles in nucleation mode, Aitken mode, and accumulation mode, which were previously in separate modules and thought to be irrelevant to one another for nitrate particles within one simulation time step. Since adding the new mechanism will reduce the vapors available for particle formation and grow particles to larger sizes, it will affect particles in all sizes. This work opens up a new perspective on describing nanoparticle growth and activation to CCNs in large-scale modeling, which may help to bring the modeling results closer to observations and reduce the uncertainty for calculating the Earth's radiative forcing.

4.2 Methods

Rapid particle growth experiments in CLOUD

Experiments to study the chemical and physical mechanisms of nitric acid and ammonia driven rapid growth were performed in the 26.1 m^3 electropolished stainless-steel CLOUD atmospheric chamber at CERN during the CLOUD 13 campaign (Fall 2018). The integrity of the CLOUD chamber has been verified in many previous works, which allows particle formation and growth to take place with minimal contamination at precisely controlled conditions (Kirkby et al., 2011; Kirkby et al., 2016; Tröstl et al., 2016). Dry air was supplied by the evaporation of liquid nitrogen (Messer, 99.999%) and liquid oxygen (Messer, 99.999%), mixed in the atmospheric gas volume ratio of 79:21. The temperature was varied between +20 ^{o}C to 10 ^{o}C and relative humidity was kept at 60% using a Nafion® humidifier with ultrapure water (18 MΩ, Millipore Corporation). Trace gases such as SO_2 (CARBAGAS AG, 500 ppm) and NH_3 (Messer, 100 ppm) were injected directly from pressurized gas cylinders. Toluene (Messer), an anthropogenic volatile organic compound (VOC), was added by flushing air through a evaporator. OH radicals were either generated by the photolysis of O_3, produced by introducing air through a UVC-illuminated quartz tube, or nitrous acid (HONO), synthesized by continual mixing of H_2SO_4 (Sigma-Aldrich, 99%) with $NaNO_2$ (Sigma Aldrich, 99%), depending on the target NO_x conditions. Photolysis was initiated by illumination from a set of UV sources, including a 4-W KrF excimer UV laser (UVX) at 248 nm and four 200-W Hama-

matsu Hg-Xe UVH lamps at wavelengths between 250 to 450 nm. Experiments were conducted in the presence of ions produced by galactic cosmic rays (GCR), at concentrations typical at sea level, or by a high-flux pion beam (3.6-GeV) to reproduce ion-pairs concentrations in the upper troposphere. Additional experiments were performed under neutral conditions by removing ions with field cage electrodes at the end of the chamber ($\pm 30kV$).

Gas-phase sulfuric acid, nitric acid, and ammonia concentrations were monitored by a nitrate chemical ionization atmospheric pressure interface time-of-flight (CI-APi-TOF) mass spectrometer (Kürten et al., 2011), a bromide CI-APi-TOF mass spectrometer (Jokinen et al., 2012), and a water cluster CI-APi-TOF mass spectrometer (Pfeifer et al., 2020), respectively. VOCs were measured by a proton transfer reaction time-of-flight mass spectrometer (PTR-TOF-MS Breitenlechner et al., 2017. An iodide adduct chemical ionization time-of-flight mass spectrometer equipped with a Filter Inlet for Gases and Aerosols (FIGAERO-CIMS) was employed to measure particle phase composition (Lopez-Hilfiker et al., 2014). Particle size distributions were retrieved from combining measurements from a differential mobility analyzer train (DMA-train, Stolzenburg et al., 2017), a custom-built nano-Scanning Electrical Mobility Spectrometer (Kong et al., 2020), a nano-scanning mobility particle sizer (nano-SMPS, Tröstl et al., 2015), and a long-SMPS (Jurányi et al., 2011), with size ranges specified as in Wang et al. (2020).

Growth rate parameterization using aerosol dynamic equation

The continuous general aerosol dynamic equation is defined in J. Seinfeld and Pandis (2006) as:

$$\begin{aligned}\frac{\partial n\,(v,\ t)}{\partial t} &= \frac{1}{2}\int_0^v K(v-q,q)\ n(v-q,\ t)\ n(q,\ t)\ \mathrm{d}q \\ &- n(v,\ t)\int_0^\infty K(q,v)\ n(q,\ t)\ \mathrm{d}q - \frac{\partial}{\partial v}[I(v)\ n(v,\ t)] \\ &+ J_0(v,t)\ \delta(v-v_0) + S(v,t) - R(v,t) \end{aligned} \tag{4.1}$$

where v_0 is the lower limit of volume for a stable particle, $n(v,\ t)$ is the particle volume distribution at time t and volume v, $K(q,v)$ is the coagulation coefficient between particle of volume v and q, J_0 is the homogeneous nucleation rate that provides a source of particles of size v_0, $S(v,t)$, $R(v,t)$, and $I(v,t)$ are the sources, sinks, and growth of particle of volume v, respectively. The time- and size-dependent condensational growth rate of aerosols within a well-defined air mass at size d_p can

then be written as:

$$\begin{aligned} \frac{\partial n\left(d_{\mathrm{p}},\ t\right)}{\partial t}+\frac{\partial}{\partial d_{\mathrm{p}}}\left[n\left(d_{\mathrm{p}},\ t\right) I\left(d_{\mathrm{p}},\ t\right)\right] &= J_{\nu}\left(\delta(d_{\mathrm{p}})\right)+S\left(d_{\mathrm{p}},\ t\right) \\ &- K_{c}\left(d_{\mathrm{p}},\ t\right) n\left(d_{\mathrm{p}},\ t\right) \\ &- \sum_{i} R_{i}\left(d_{\mathrm{p}},\ t\right) n\left(d_{\mathrm{p}},\ t\right) \end{aligned} \tag{4.2}$$

where $K_c\left(d_{\mathrm{p}},\ t\right)$ represents the complete coagulation kernel for particle at diameter d_p. The entire equation can be solved numerically by showing that $d_{\mathrm{p}}=d_{\mathrm{p}}\left(t\right)$ along a growth characteristic, and the rate of diameter change of a particle as a result of condensation or evaporation is then:

$$I_{\mathrm{d}}\left(d_{\mathrm{p}},\ t\right)=\frac{\mathrm{d}d_{\mathrm{p}}}{\mathrm{d}t} \tag{4.3}$$

for a particle that is neither added to the population at size d_{p} nor lost from that size at time t. Furthermore, if we define the flux through size space as $F\left(d_{\mathrm{p}}\left(t\right)\right)=n\left(d_{\mathrm{p}}\left(t\right)\right) I_d\left(d_{\mathrm{p}}\left(t\right)\right)$, we can apply the method of characteristics to show that the time rate of change of F along the growth path of any particle is:

$$\begin{aligned} \frac{\mathrm{d}F\left(d_{\mathrm{p}}\left(t\right)\right)}{\mathrm{d}t} &= -n\left(d_{\mathrm{p}}\left(t\right)\right)\frac{\mathrm{d}I_d\left(d_{\mathrm{p}}\left(t\right)\right)}{\mathrm{d}t}+J_{\nu}\left(\delta(d_{\mathrm{p}})\right)+S\left(d_{\mathrm{p}}t\right) \\ &- K_{\mathrm{c}}\left(d_{\mathrm{p}},\ t\right) n\left(d_{\mathrm{p}},\ t\right)-\sum_{i} R_{i}\left(d_{\mathrm{p}},\ t\right) n\left(d_{\mathrm{p}},\ t\right) \end{aligned} \tag{4.4}$$

To evaluate the flux and diameter variation along a growth characteristic, we then model the gas-to-particle conversion contribution to the growth rate as:

$$I\left(d_{\mathrm{p}}\right)=2\pi d_{\mathrm{p}}\ f\left(\mathrm{Kn},\alpha\right)\left[N_{\infty}-N_{\mathrm{sat}}\exp\left(\frac{d_{\mathrm{K}}}{d_{\mathrm{p}}}\right)\right] \tag{4.5}$$

where $f\left(\mathrm{Kn},\alpha\right)$ is the correction factor due to noncontinuum effects (Kn) and imperfect surface accommodation (α), N_{∞} and N_{sat} are vapor concentration and saturation vapor concentration, respectively, and

$$d_{\mathrm{K}}=\frac{2\sigma M}{RT\rho_{\mathrm{p}}} \tag{4.6}$$

is the Kelvin diameter, a material property that accounts for the effect of the surface free energy of the particle on the partial pressure that is required to maintain vapor-liquid equilibrium with the droplet. σ is the surface tension and M is the molecular weight of the substance, and ρ_{p} is the liquid-phase density. The sinks of particles

considered in this study include dilution loss, particle wall loss, and coagulational loss. With all the instruments connected the CLOUD facility, the total sampling flow rate was 270 L min^{-1}, resulting in a dilution lifetime of 1.6 h in the 26.1 m^3 chamber:

$$R_{\mathrm{dil}} = k_{\mathrm{dil}}\, n(d_{\mathrm{p}},\, t) = 1.72 \times 10^{-4} \mathrm{s}^{-1}\, n(d_{\mathrm{p}},\, t) \tag{4.7}$$

Particle wall lose rate was extrapolated from the sulfuric acid wall loss rate:

$$R_{\mathrm{wall}} = k_{\mathrm{wall}} n(d_{\mathrm{p}},\, t) = 2.116 \times 10^{-3} \left(\frac{T}{278\ \mathrm{T}}\right)^{0.875} \left(\frac{0.82}{d_{\mathrm{p}}}\right)\, n(d_{\mathrm{p}},\, t) \tag{4.8}$$

The coagulation coefficient between two particles at $d_{\mathrm{p,i}}$ and $d_{\mathrm{p,j}}$ is defined as:

$$\begin{aligned} K_{i,j} &= 2\pi(\mathcal{D}_i + \mathcal{D}_j)(d_{\mathrm{p,i}} + d_{\mathrm{p,j}}) \\ &\times \left[\frac{d_{\mathrm{p,i}} + d_{\mathrm{p,j}}}{d_{\mathrm{p,i}} + d_{\mathrm{p,j}} + 2(g_i^2 + g_j^2)^{1/2}} + \frac{8(\mathcal{D}_i + \mathcal{D}_j)}{\alpha(\bar{c}_i^2 + \bar{c}_j^2)^{1/2}(d_{\mathrm{p,i}} + d_{\mathrm{p,j}})}\right] \end{aligned} \tag{4.9}$$

where $\mathcal{D}$ is particle diffusivity, $\bar{c}$ is the particle mean velocity and g is the mean distance from the surface of a sphere covered by a particle after moving one mean free path (**FUCHS:1971aa**; Charan et al., 2019):

$$g_i = \frac{\sqrt{2}\pi\bar{c}_i}{24\mathcal{D}_i\, d_{\mathrm{p,i}}}\left[\left(d_{\mathrm{p,i}} + \frac{8\mathcal{D}_i}{\pi\bar{c}_i}\right)^3 - \left(d_{\mathrm{p,i}}^2 + \frac{64\mathcal{D}_i^2}{\pi^2\bar{c}_i^2}\right)^{3/2}\right] - d_{\mathrm{p,i}} \tag{4.10}$$

After solving the given general dynamic equation and recovering the sink-free particle growth profile, the condensational flux, $I(d_{\mathrm{p}})$, as defined in Eq. (4.5), and the Kelvin diameter, d_{K}, defined in Eq. (4.6), can be computed as the two signature parameters that will then be applied in the aerosol box model GLOMAP to represent the gas-to-particle conversion for nanoparticle growth.

Global modeling of nitric acid and ammonia with TOMCAT/GLOMAP

The GLobal Model of Aerosol Processes (GLOMAP) is the aerosol microphysics module in the TOMCAT 3-D Eulerian offline chemical transport model (Spracklen et al., 2005; Mann et al., 2010). The baseline model of GLOMAP nitrate module includes all the nucleation mechanisms from previous CLOUD experiments, such as the ternary inorganic nucleation, biogenic nucleation and amines nucleation (Kirkby et al., 2011; Riccobono et al., 2014; Kirkby et al., 2016). The meteorology is forced by ERA-Interim (Berrisford et al., 2011). Climatology of biomass burning

emissions and dust are included, but there is no marine or anthropogenic organic emission. Emission data are retrieved from the AeroCom 2000 dataset (Dentener et al., 2006), including the ammonia emission data from Bouwman et al. (1997). The nitrate solver assumes all particles are liquid or in aqueous solution, irrespective of relative humidity, temperature, or particle size. Particle sizes are represented by four different modes: nucleation (3-10 nm), Aitken (10-100 nm), accumulation (100–1000 nm), and coarse (> 1000 nm). Figure 4.1, 4.2, and 4.3 shows the annual mean concentrations at different altitudes of SO_2, NH_3 and HNO_3 respectively, using the described baseline model. Figure 4.4 demonstrates the particle number concentration predicted by the current baseline model, which already indicates an underestimation of nucleation events in the upper free troposphere as particle numbers decreases with altitudes. In addition, the current model also shows the molecular ratio of ammonium to sulfate (NH_4^+/SO_4^{2-}) in particle phase can be as high as 20 at the lower altitude, suggesting nitrate may be a major contributor to particles in the nucleation mode (Figure 4.5) at the surface. The seasonal variation of nitrate particulate mass fractions shown in Figure 4.6 indicates that nitrate has a great impact on particles in the nucleation mode at lower temperatures. The simulated total number concentration using the baseline GLOMAP model is generally biased low compared to the observation data from the NASA Atmospheric Tomography Campaign (Atom-1) (Wofsy et al., 2018), especially in the tropics (Figure 4.7).

4.3 Results and Discussion

The survival probability of nucleated clusters in urban environment

In order to examine whether the rapid growth caused by nitric acid and ammonia can help to explain the observed high survival probability of nucleated clusters under highly polluted conditions, a series of experiments were conducted at the CLOUD chamber with a mixture of anthropogenic vapors, under condensation sinks up to 0.1 s^{-1}, typical of urban haze conditions (Mönkkönen et al., 2005; Xiao et al., 2015; Yu et al., 2017). Figure 4.8 shows two representative nucleation events at 5 ^oC with (Figure 4.8 a,c) and without HNO_3 (Figure 4.8 b,d). The black lines on the particle size distribution results show the linear fit to the 50% appearance times. The condensation sink, a measure of coagulation scavenging by pre-existing particles, is calculated using method described in Pirjola et al. (1999). Figure 4.8c shows that although nucleation can take place under a constant CS of 0.06 s^{-1} (Figure 4.8a) that is formed from secondary vapors, the freshly nucleated particles are effectively scavenged by the large number of pre-existing. The observed growth rate

(5.5 nm/h) is very similar to experiments or ambient observations under relatively clean conditions. However, in the presence of ammonia and nitric acid vapors, the survival probability of particles formed from nucleation increases significantly with rapid growth (above 100 nm/h) shown in Figure 4.8d, even under a CS of 0.025 s^{-1} (Figure 4.8b). The observed high growth rates agree with the hypothesis that in order for nanoparticles to survive under urban high CS, they have to grow much faster than we thought (Kulmala et al., 2017). The experimental results demonstrate that the previously unconsidered contribution from HNO_3 as a condensing species at low size regime needs to be further evaluated on a large scale. The fact that nitric acid can help nucleated clusters survive under urban CS may help us to better constrain the large-scale modeling and to bridge discrepancy between simulations and observations of particle number concentrations at the surface.

Temperature dependence of the Kelvin diameter

The Kelvin diameter for the rapid growth from nitric acid and ammonia co-condensation is simply the activation diameter at which the runaway growth takes place, as measured in Wang et al. (2020). Since saturation is the key factor that determines the activation, the Kelvin diameter, defined in Eq. (4.6) can also be rewritten as:

$$d_{\mathrm{K}} = \frac{4\sigma v}{kT \ln S} \tag{4.11}$$

where v is the volume occupied by a molecule in the liquid phase, and the saturation ratio, S, is the ratio of the vapor product of HNO_3 and NH_3 to the dissociation constant, K_{p}, defined as the product of the equilibrium partial pressure of HNO_3 and NH_3. Since all the experiments were conducted at 60% RH, which is much lower than the deliquescence relative humidity of ammonium nitrate, the dissociation constant can be approximated as (Mozurkewich, 1993):

$$\ln K_{\mathrm{p}} = 118.87 - \frac{24084}{T} - 6.025 \ln T \tag{4.12}$$

Given that the dependence of σ on temperature, T, cannot be solved numerically, the Kelvin diameters were fitted against saturation ratio, S, with temperature dependence, such that:

$$d_{\mathrm{K}} = a(T) \exp\left(b(T)\ S\right) \tag{4.13}$$

The optimization was achieved using the first order Broyden–Fletcher–Goldfarb–Shanno algorithm (BFGS, Mogensen and Riseth, 2018), while assuming a Gaussian error of 30% uncertainty on the measured activation diameters. Figure 4.10 shows the fitted results using the described optimization method with the temperature dependent terms:

$$\begin{aligned} a &= 0.586634\,T - 148.02 \\ b &= 0.0254364\,T - 6.6778 \end{aligned} \tag{4.14}$$

in the temperature range of -10 °C to 20 °C, which is substituted into Eq. (4.5) to compute for the condensational flux.

Growth rate extraction from CLOUD size distribution data

Since the GLOMAP box model originally uses the conventional growth rates (in nm/h) to represent nanoparticle growth (Gordon et al., 2017), to facilitate the initialization of the nitrate scheme in the model, growth rates have been calculated by fitting the 50% appearance time linearly as a function of d_{p}. Figure 4.9 shows the observed growth rates from CLOUD experiments as a function of excess vapor product of nitric acid and ammonia. The excess vapor product is simply the difference between the measured vapor product and K_{p}. The growth rate is fitted with a log-log function as:

$$\log(\mathrm{GR}) = 1.018 \times \log\left(\left[[\mathrm{HNO_3}][\mathrm{NH_3}]\right]_{\mathrm{ex}} - 3.255\right) \tag{4.15}$$

4.4 Summary and Conclusions

Recent experiments performed at the CERN CLOUD chamber have suggested the importance of the ammonia-nitric acid system in NPF. Here we demonstrated that this new mechanism, resulting from the co-condensation of nitric acid and ammonia, can help freshly nucleated clusters to grow out of the "valley of death", i.e., the sub-10 nm size regime where they are most vulnerable to coagulational loss, under high condensation sink, thereby increasing their survival probabilities in polluted urban environments. This gas-to-particle conversion has been parameterized as condensational flux using aerosol general dynamic equations. Furthermore, the dependence of the Kelvin diameters or the activation sizes on saturation ratio has also been optimized using the BFGS algorithm. A baseline nitrate module has been constructed in the GLOMAP aerosol box model, which will be used as the platform

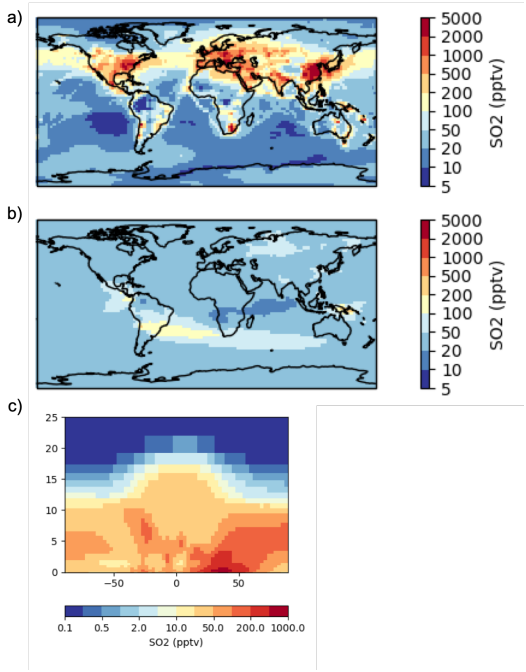

Figure 4.1: Annual mean SO_2 concentration in pptv predicted by the current GLOMAP model (a) at the surface, (b) at 10 km, and (c) latitude vs altitude in km, with an annual mean over longitudes.

to evaluate the impact of the recently found rapid growth mechanism on a large scale. Both the conventional growth rates derived using the appearance time method and the newly derived parameters will be incorporated into GLOMAP once the complexity with the simulation time step has been resolved. This new perspective of quantifying NPF contribution to global CCN budget can better represent nanoparticle early growth in climate models, which will help to resolve the large uncertainties in estimates and interpretations of cloud reflectivity and the Earth's changing energy budget.

Acknowledgement

The authors would like to thank the CLOUD experiment for providing the facility for instrument testing and operation. This work was supported by the National Science Foundation under Grant No. AGS 1602086 and AGS 1801329.

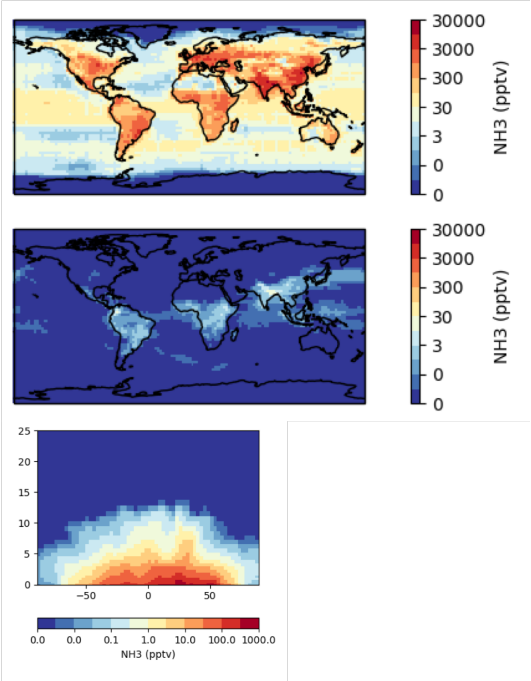

Figure 4.2: Annual mean NH_3 concentration in pptv predicted by the current GLOMAP model (a) at the surface, (b) at 10 km, and (c) latitude vs altitude in km, with an annual mean over longitudes.

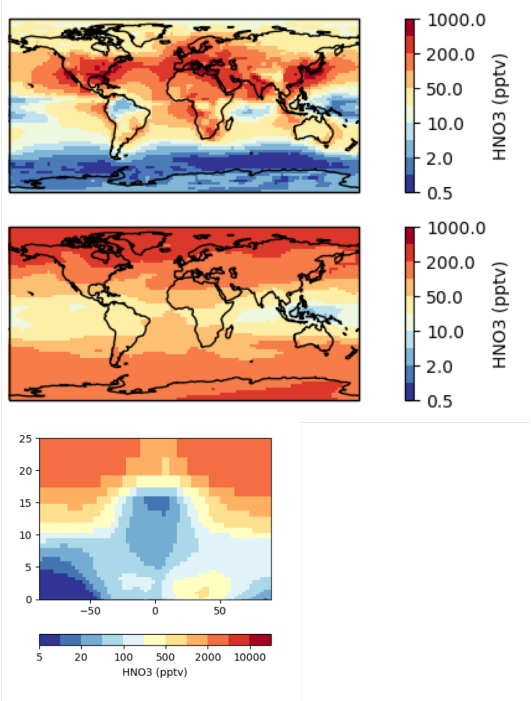

Figure 4.3: Annual mean HNO_3 concentration in pptv predicted by the current GLOMAP model (a) at the surface, (b) at 10 km, and (c) latitude vs altitude in km, with an annual mean over longitudes.

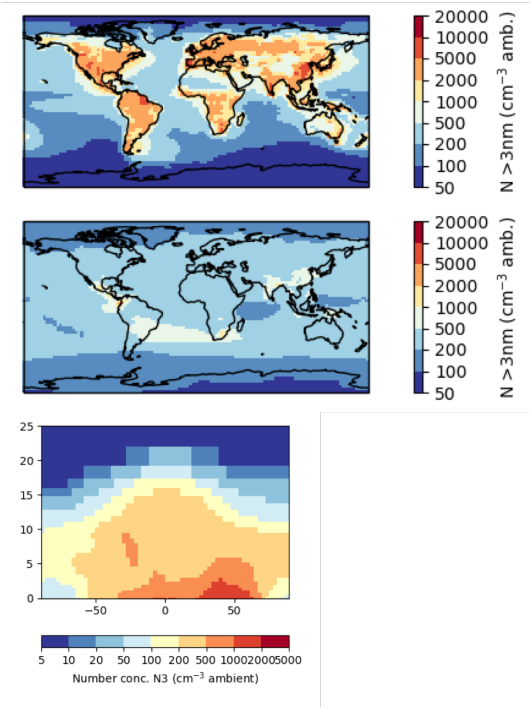

Figure 4.4: Annual mean particle number concentration in cm^{-3} predicted by the current GLOMAP model (a) at the surface, (b) at 10 km, and (c) latitude vs altitude in km, with an annual mean over longitudes. Since particle number concentration decreases with altitude, it already suggests that there is not enough nucleation represented in the model in the upper troposphere.

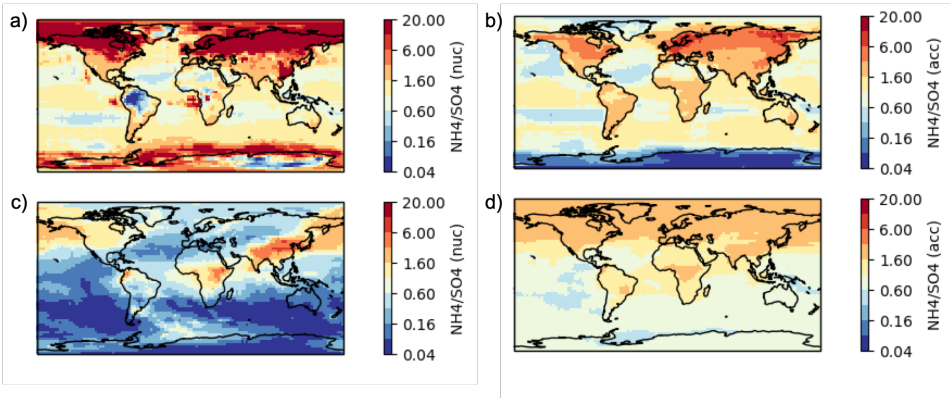

Figure 4.5: Molecular ratio of ammonium to sulfate (NH_4^+/SO_4^{2-}) predicted by GLOMAP in particle phase for (a) nucleation mode particles at the surface, (b) accumulation mode particles at the surface, (c) accumulation mode particles at 10 km altitude, (d) accumulation mode particles at 10 km altitude. Since the ratio of NH_4^+/SO_4^{2-} can be over 20 at the surface (a), it indicates that there are a large number of nitrate particles in the nucleation mode, which are yet to be included. Ammonia is limited in remote oceans and Antarctica at the surface, suggesting not much nitrate particle may be formed at higher altitude.

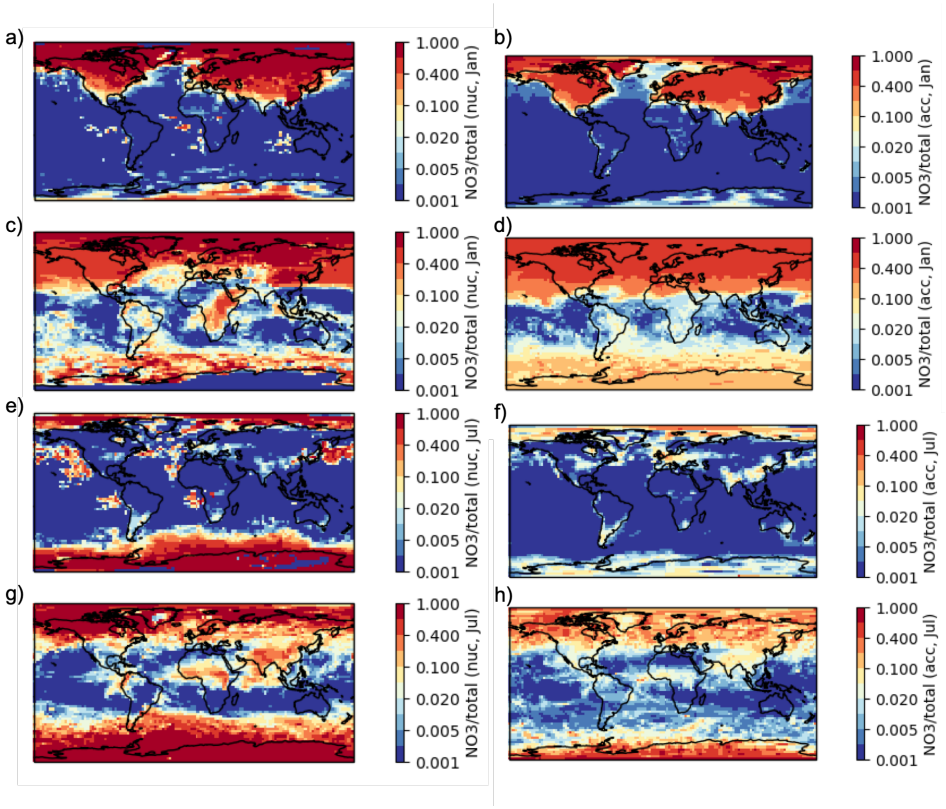

Figure 4.6: Nitrate particulate mass fraction predicted by the GLOMAP simulation for (a) particles in nucleation mode at the surface in January; (b) particles in accumulation mode at the surface in January; (c) particles in nucleation mode at 10 km altitude in January; (d) particles in accumulation mode at 10 km altitude in January; (e) particles in nucleation mode at the surface in July; (f) particles in accumulation mode at the surface in July; (g) particles in nucleation mode at 10 km altitude in July; (h) particles in accumulation mode at 10 km altitude in July.

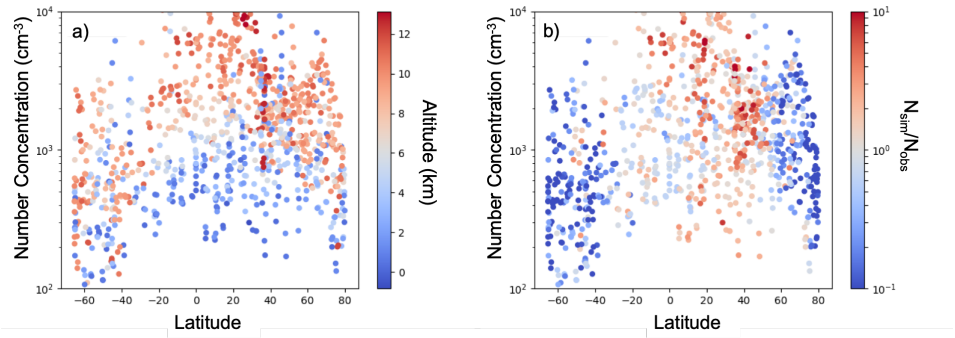

Figure 4.7: Comparison of 2016 daily mean total particle number concentrations to Atom1 observations. (a) Five-minute-averaged observation data from the NASA Atom1 campaign plotted as total number concentrations against latitude. The color denotes the altitudes of the measurement; (b) Similar to (a), but the color indicates the value of the ratio of simulated to observed particle number concentration with blue meaning that the model underestimates particle numbers, and red meaning it overestimates. 577 out of 996 data points have simulated number concentrations a factor of 2 or more below observed number concentration; 105 have a factor 2 or more above.

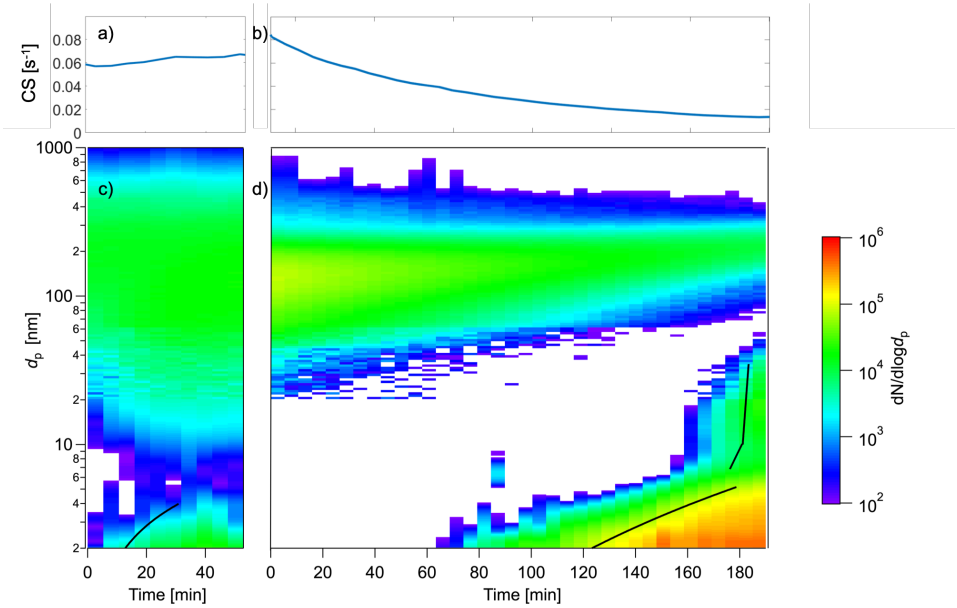

Figure 4.8: Rapid growth events observed in the CLOUD chamber. (a) (b) condensation sinks calculated for the two events. (c) Particle nucleation and growth at 5 °C from a mixture of 0.2 pptv sulfuric acid, 3 ppbv ammonia, 10 ppbv HONO, 10 pptv dimethylamine at 60% RH under a constant CS of 0.06 s^{-1}. Nanoparticles grow to roughly 4.3 nm with a growth rate of 5.5 nm/h in 30 min before they lost to the larger particles. (d) Particle formation and growth under similar sulfuric acid and HONO conditions, but with 150 pptv dimethylamine, 8 ppbv ammonia, and the addition of 600 pptv HNO_3. The nucleation took place when the CS decreases from 0.08 s^{-1} to 0.025 s^{-1} and was more intense due to the extra dimethylamine. The existence of HNO_3 resulted in an extremely fast growth with a growth rate above 100 nm/h, 80 min after nucleation started, growing particles from 5 nm to 50 nm in 30 min.

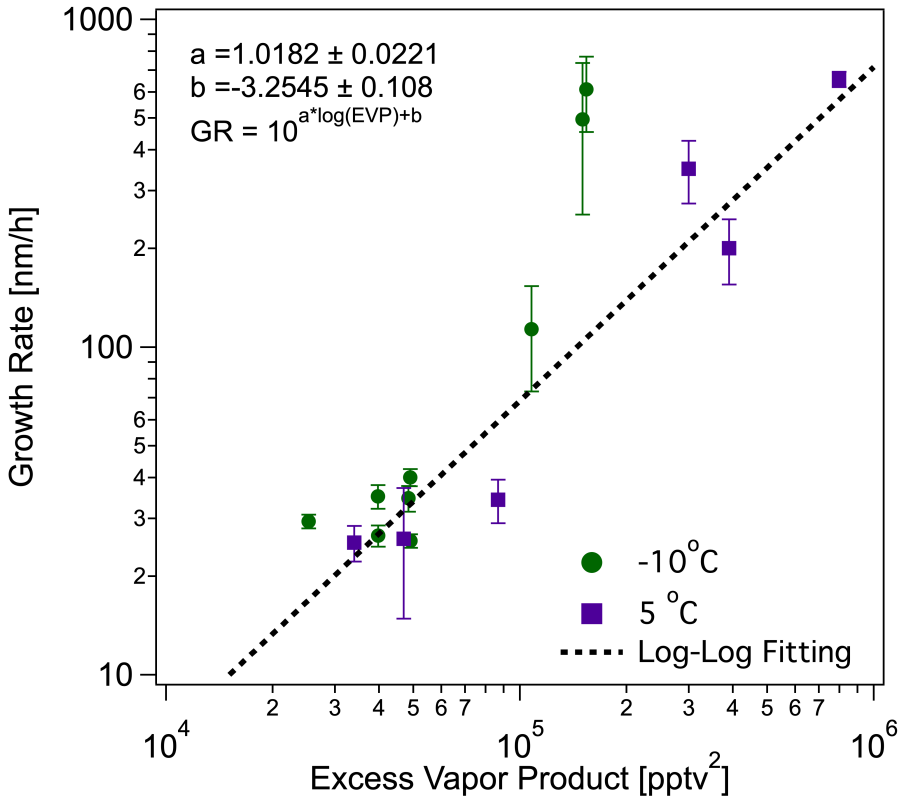

Figure 4.9: Growth rates after activation versus the excess vapor product of measured nitric acid and ammonia levels at +5°C and −10°C. The growth rates are the slopes of linear fits to the 50% appearance times calculated from all sizes above the activation diameter. The excess vapor product (denoted by EVP in the fitting equation), is calculated using the dissociation constant as described in Eq.(4.12).

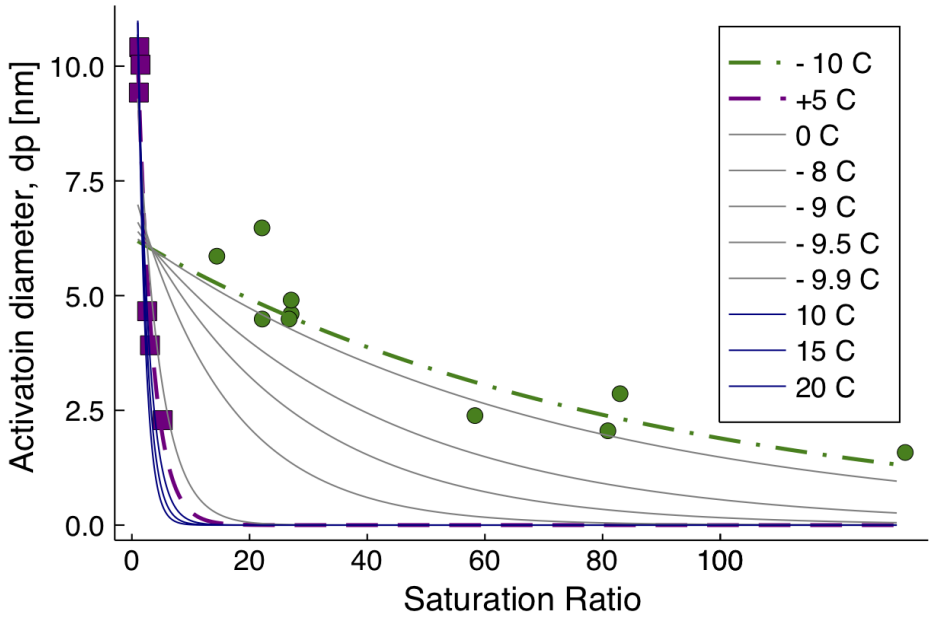

Figure 4.10: Observed activation diameters versus saturation ratio, with a temperature dependence. The activation diameters are the sizes at which the rapid growth from nitric acid and ammonia co-condensation take place. The experimental data at +5 ^{o}C and -10 ^{o}C are fitted using the BFGS algorithm with two temperature dependent terms, as shown in Eq.4.13. Predictions of the Kelvin diameters are given in solid lines from -10 ^{o}C to 20 ^{o}C using the optimization results.

References

S. N. Behera et al. (Nov. 2013). "Ammonia in the atmosphere: a review on emission sources, atmospheric chemistry and deposition on terrestrial bodies". en. In: *Environmental Science and Pollution Research* 20.11, pp. 8092–8131. ISSN: 1614-7499. DOI: 10.1007/s11356-013-2051-9.

P. Berrisford et al. (Nov. 2011). "The ERA-Interim archive Version 2.0". In: 1, p. 23. URL: https://www.ecmwf.int/node/8174.

F. Bianchi et al. (May 2016). "New particle formation in the free troposphere: A question of chemistry and timing". In: *Science*, aad5456. DOI: 10.1126/science.aad5456.

A. F. Bouwman et al. (1997). "A global high-resolution emission inventory for ammonia". en. In: *Global Biogeochemical Cycles* 11.4, pp. 561–587. ISSN: 1944-9224. DOI: 10.1029/97GB02266.

M. Breitenlechner et al. (2017). "PTR3: An Instrument for Studying the Lifecycle of Reactive Organic Carbon in the Atmosphere". In: *Analytical Chemistry* 89, pp. 5824–5831. DOI: 10.1021/acs.analchem.6b05110.

S. M. Charan et al. (Dec. 2019). "Computational Simulation of Secondary Organic Aerosol Formation in Laboratory Chambers". en. In: *Chemical Reviews* 119.23, pp. 11912–11944. ISSN: 0009-2665, 1520-6890. DOI: 10.1021/acs.chemrev.9b00358.

F. Dentener et al. (Sept. 2006). "Emissions of primary aerosol and precursor gases in the years 2000 and 1750 prescribed data-sets for AeroCom". English. In: *Atmospheric Chemistry and Physics* 6.12, pp. 4321–4344. ISSN: 1680-7316. DOI: https://doi.org/10.5194/acp-6-4321-2006.

Y. Feng and J. E. Penner (2007). "Global modeling of nitrate and ammonium: Interaction of aerosols and tropospheric chemistry". en. In: *Journal of Geophysical Research: Atmospheres* 112.D1. ISSN: 2156-2202. DOI: 10.1029/2005JD006404.

H. Gordon et al. (2017). "Causes and importance of new particle formation in the present-day and preindustrial atmospheres". en. In: *Journal of Geophysical Research: Atmospheres* 122.16, pp. 8739–8760. ISSN: 2169-8996. DOI: 10.1002/2017JD026844. (Visited on 05/06/2020).

M. Höpfner et al. (Aug. 2019). "Ammonium nitrate particles formed in upper troposphere from ground ammonia sources during Asian monsoons". en. In: *Nature Geoscience* 12.8, pp. 608–612. ISSN: 1752-0908. DOI: 10.1038/s41561-019-0385-8.

T. Jokinen et al. (2012). "Atmospheric sulphuric acid and neutral cluster measurements using CI-APi-TOF". In: *Atmospheric Chemistry and Physics* 12.9, pp. 4117–4125. DOI: 10.5194/acp-12-4117-2012.

Z. Jurányi et al. (2011). "A 17 month climatology of the cloud condensation nuclei number concentration at the high alpine site Jungfraujoch". en. In: *Journal of Geophysical Research: Atmospheres* 116.D10. ISSN: 2156-2202. DOI: 10.1029/2010JD015199.

V.-M. Kerminen et al. (Sept. 2018). "Atmospheric new particle formation and growth: review of field observations". en. In: *Environmental Research Letters* 13.10, p. 103003. ISSN: 1748-9326. DOI: 10.1088/1748-9326/aadf3c. (Visited on 03/23/2020).

J. Kirkby et al. (Aug. 2011). "Role of sulphuric acid, ammonia and galactic cosmic rays in atmospheric aerosol nucleation". en. In: *Nature* 476.7361, pp. 429–433. ISSN: 1476-4687. DOI: 10.1038/nature10343. (Visited on 10/23/2018).

J. Kirkby et al. (May 2016). "Ion-induced nucleation of pure biogenic particles". en. In: *Nature* 533.7604, pp. 521–526. ISSN: 1476-4687. DOI: 10.1038/nature17953. (Visited on 06/25/2018).

W. Kong, S. Amanatidis, H. Mai, C. Kim, B. Schulze, Y. Huang, J. H. Seinfeld, and R. C. Flagan (2020). "The nano-scanning electrical mobility spectrometer (nSEMS) and its application to size distribution measurements of 1.5-25nm particles". In: *Atmospheric Measurement Techniques Discussion*. preprint.

C. Kuang et al. (Apr. 2012). "Size and time-resolved growth rate measurements of 1 to 5 nm freshly formed atmospheric nuclei". English. In: *Atmospheric Chemistry and Physics* 12.7, pp. 3573–3589. ISSN: 1680-7316. DOI: https://doi.org/10.5194/acp-12-3573-2012.

M. Kulmala et al. (Aug. 2017). "Atmospheric gas-to-particle conversion: why NPF events are observed in megacities?" In: *Faraday Discussions* 200.0, pp. 271–288. ISSN: 1364-5498. DOI: 10.1039/C6FD00257A.

M. Kulmala and V.-M. Kerminen (Nov. 2008). "On the formation and growth of atmospheric nanoparticles". en. In: *Atmospheric Research* 90.2-4, pp. 132–150. ISSN: 01698095. DOI: 10.1016/j.atmosres.2008.01.005.

M. Kulmala et al. (2004). "Formation and growth rates of ultrafine atmospheric particles: A review of observations". In: *Journal of Aerosol Science* 35, pp. 143–176. DOI: 10.1016/j.jaerosci.2003.10.003.

M. Kulmala et al. (Sept. 2012). "Measurement of the nucleation of atmospheric aerosol particles". en. In: *Nature Protocols* 7.9, pp. 1651–1667. ISSN: 1750-2799. DOI: 10.1038/nprot.2012.091.

A. Kürten et al. (2011). "Performance of a corona ion source for measurement of sulfuric acid by chemical ionization mass spectrometry". In: *Atmospheric Measurement Techniques* 4.3, pp. 437–443. DOI: 10.5194/amt-4-437-2011.

S.-H. Lee et al. (Sept. 2003). "Particle Formation by Ion Nucleation in the Upper Troposphere and Lower Stratosphere". en. In: *Science* 301.5641, pp. 1886–1889. ISSN: 0036-8075, 1095-9203. DOI: 10.1126/science.1087236.

H. Liao and J. H. Seinfeld (2005). “Global impacts of gas-phase chemistry-aerosol interactions on direct radiative forcing by anthropogenic aerosols and ozone”. en. In: *Journal of Geophysical Research: Atmospheres* 110.D18. ISSN: 2156-2202. DOI: 10.1029/2005JD005907.

F. D. Lopez-Hilfiker et al. (2014). “A novel method for online analysis of gas and particle composition: description and evaluation of a Filter Inlet for Gases and AEROsols (FIGAERO)”. In: *Atmospheric Measurement Techniques* 7.4, pp. 983–1001. DOI: 10.5194/amt-7-983-2014.

G. W. Mann et al. (Oct. 2010). “Description and evaluation of GLOMAP-mode: a modal global aerosol microphysics model for the UKCA composition-climate model”. English. In: *Geoscientific Model Development* 3.2, pp. 519–551. ISSN: 1991-959X. DOI: https://doi.org/10.5194/gmd-3-519-2010.

J. Merikanto et al. (2009). “Impact of nucleation on global CCN”. en. In: *Atmos. Chem. Phys.*, p. 16. DOI: 10.5194/acp-9-8601-2009.

P. Mogensen and A. Riseth (Apr. 2018). “Optim: A mathematical optimization package for Julia”. en. In: *Journal of Open Source Software* 3.24, p. 615. ISSN: 2475-9066. DOI: 10.21105/joss.00615.

P. Mönkkönen et al. (Jan. 2005). “Measurements in a highly polluted Asian mega city: observations of aerosol number size distribution, modal parameters and nucleation events”. In: *Atmospheric Chemistry and Physics* 5.1, pp. 57–66. ISSN: 1680-7316. DOI: https://doi.org/10.5194/acp-5-57-2005.

M. Mozurkewich (1993). “The dissociation constant of ammonium nitrate and its dependence on temperature, relative humidity and particle size”. In: *Atmospheric Environment. Part A. General Topics* 27.2, pp. 261–270. DOI: 10.1016/0960-1686(93)90356-4.

G. Myhre et al. (Feb. 2009). “Modelled radiative forcing of the direct aerosol effect with multi-observation evaluation”. English. In: *Atmospheric Chemistry and Physics* 9.4, pp. 1365–1392. ISSN: 1680-7316. DOI: https://doi.org/10.5194/acp-9-1365-2009.

C. D. O’Dowd et al. (June 2002). “Marine aerosol formation from biogenic iodine emissions”. en. In: *Nature* 417.6889, pp. 632–636. ISSN: 1476-4687. DOI: 10.1038/nature00775. (Visited on 05/06/2020).

J. Pfeifer et al. (May 2020). “Measurement of ammonia, amines and iodine compounds using protonated water cluster chemical ionization mass spectrometry”. English. In: *Atmospheric Measurement Techniques* 13.5, pp. 2501–2522. ISSN: 1867-1381. DOI: https://doi.org/10.5194/amt-13-2501-2020.

L. Pichelstorfer et al. (Jan. 2018). “Resolving nanoparticle growth mechanisms from size- and time-dependent growth rate analysis”. English. In: *Atmospheric Chemistry and Physics* 18.2, pp. 1307–1323. ISSN: 1680-7316. DOI: https://doi.org/10.5194/acp-18-1307-2018.

L. Pirjola et al. (Sept. 1999). “FORMATION OF SULPHURIC ACID AEROSOLS AND CLOUD CONDENSATION NUCLEI: AN EXPRESSION FOR SIGNIFICANT NUCLEATION AND MODEL COMPRARISON”. en. In: *Journal of Aerosol Science* 30.8, pp. 1079–1094. ISSN: 0021-8502. DOI: 10.1016/S0021-8502(98)00776-9.

F. Riccobono et al. (May 2014). “Oxidation Products of Biogenic Emissions Contribute to Nucleation of Atmospheric Particles”. en. In: *Science* 344.6185, pp. 717–721. ISSN: 0036-8075, 1095-9203. DOI: 10.1126/science.1243527.

A. G. Russell et al. (Jan. 1983). “Mathematical modeling of the formation and transport of ammonium nitrate aerosol”. en. In: *Atmospheric Environment (1967)* 17.5, pp. 949–964. ISSN: 0004-6981. DOI: 10.1016/0004-6981(83)90247-0.

J. Seinfeld and S. Pandis (2006). *Atmospheric Chemistry and Physics*. 2nd ed. Hoboken, New Jersey: John Wiley & Sons.

M. Sipilä et al. (Mar. 2010). “The Role of Sulfuric Acid in Atmospheric Nucleation”. en. In: *Science* 327.5970, pp. 1243–1246. ISSN: 0036-8075, 1095-9203. DOI: 10.1126/science.1180315.

D. V. Spracklen et al. (Aug. 2005). “A global off-line model of size-resolved aerosol microphysics: I. Model development and prediction of aerosol properties”. English. In: *Atmospheric Chemistry and Physics* 5.8, pp. 2227–2252. ISSN: 1680-7316. DOI: https://doi.org/10.5194/acp-5-2227-2005.

D. Stolzenburg et al. (May 2017). “A DMA-train for precision measurement of sub-10 nm aerosol dynamics”. English. In: *Atmospheric Measurement Techniques* 10.4, pp. 1639–1651. ISSN: 1867-1381. DOI: doi.org/10.5194/amt-10-1639-2017. (Visited on 11/21/2018).

D. Stolzenburg et al. (Aug. 2018). “Rapid growth of organic aerosol nanoparticles over a wide tropospheric temperature range”. en. In: *Proceedings of the National Academy of Sciences*, p. 201807604. ISSN: 0027-8424, 1091-6490. DOI: 10.1073/pnas.1807604115.

J. Tröstl et al. (Sept. 2015). “Fast and precise measurement in the sub-20nm size range using a Scanning Mobility Particle Sizer”. In: *Journal of Aerosol Science* 87, pp. 75–87. ISSN: 0021-8502. DOI: 10.1016/j.jaerosci.2015.04.001. (Visited on 06/26/2019).

J. Tröstl et al. (May 2016). “The role of low-volatility organic compounds in initial particle growth in the atmosphere”. en. In: *Nature* 533.7604, pp. 527–531. ISSN: 1476-4687. DOI: 10.1038/nature18271.

M. Wang et al. (May 2020). “Rapid growth of new atmospheric particles by nitric acid and ammonia condensation”. en. In: *Nature* 581.7807, pp. 184–189. ISSN: 1476-4687. DOI: 10.1038/s41586-020-2270-4. (Visited on 05/13/2020).

C. J. Williamson et al. (2019). “A large source of cloud condensation nuclei from new particle formation in the tropics”. In: *Nature* 574.7778, pp. 399–403. DOI: 10.1038/s41586-019-1638-9.

S. Wofsy et al. (2018). *ATom: Merged Atmospheric Chemistry, Trace Gases, and Aerosols*. eng. ORNL Distributed Active Archive Center. DOI: 10.3334/ORNLDAAC/1581.

S. Xiao et al. (Feb. 2015). “Strong atmospheric new particle formation in winter in urban Shanghai, China”. English. In: *Atmospheric Chemistry and Physics* 15.4, pp. 1769–1769. ISSN: 16807316.

L. Xu and J. E. Penner (Oct. 2012). “Global simulations of nitrate and ammonium aerosols and their radiative effects”. English. In: *Atmospheric Chemistry and Physics* 12.20, pp. 9479–9504. ISSN: 1680-7316. DOI: https://doi.org/10.5194/acp-12-9479-2012.

H. Yu et al. (Dec. 2017). “New Particle Formation and Growth Mechanisms in Highly Polluted Environments”. en. In: *Current Pollution Reports* 3.4, pp. 245–253. ISSN: 2198-6592. DOI: 10.1007/s40726-017-0067-3.

R. Zhang et al. (Mar. 2012). “Nucleation and Growth of Nanoparticles in the Atmosphere”. In: *Chemical Reviews* 112.3, pp. 1957–2011. ISSN: 0009-2665. DOI: 10.1021/cr2001756.

H. Ziereis and F. Arnold (May 1986). “Gaseous ammonia and ammonium ions in the free troposphere”. en. In: *Nature* 321.6069, pp. 503–505. ISSN: 1476-4687. DOI: 10.1038/321503a0.

Chapter 5

INDEX OF CHAMBER ATMOSPHERIC RESEARCH IN THE UNITED STATES

Abstract

Research conducted in environmental chambers have significantly improved our understanding of chemical and physical mechanisms in the atmosphere and provided opportunities to examine the complicated processes under precisely controlled conditions. While tremendous valuable information have been collected from different chamber facilities across the US, including the Caltech dual Teflon chambers, there has yet to be an infrastructure where data can be stored, shared, and used by a broader community. Previously, the results from chamber experiments could only be obtained through direct communication with the research groups that produced the results, and no public catalogue of results was available to guide the queries. Here we developed a convention to report experimental data for the Caltech chamber users and carefully documented chambers and instruments characteristics to facilitate data organization and archiving. In addition, an online, open-access, searchable, central repository to store and share atmospheric chamber experimental data has also been established. The database, named the Index of Chamber Atmospheric Research in the United States (ICARUS), can promote collaboration between atmospheric researchers and facilitate model mechanisms by expanding modelers' access to atmospheric chamber data.

5.1 Background and Motivation

Atmospheric chamber, sometimes called environmental chamber or smog chamber, has been widely used to study atmospheric chemistry and aerosol dynamics under well-controlled conditions. Chemistry of different phases (gaseous, aqueous, solid, or heterogeneous), secondary organic aerosol (SOA) formation, and particle growth can all be studied in such chambers. Chamber facilities make it possible to connect bench-top laboratory research and ambient measurement. The CERN CLOUD chamber, for example, which studies the mechanisms of atmospheric nucleation as discussed in previous chapters, is an example of numerous chamber facilities in the world. Many breakthroughs of atmospheric sciences have been made in chamber studies all across the globe, including the Caltech dual Teflon chambers (Cocker

et al., 2001; Schwantes et al., 2016).

The Caltech chambers have been the source of much of data on quantifying the contribution of volatile organic compounds (VOCs) to SOA formation (Ng et al., 2008; Loza et al., 2013; Shiraiwa et al., 2013) and on investigating reaction dynamics between different atmospheric constituents (Nguyen et al., 2014; Zhang et al., 2015; Kenseth et al., 2018). Data from the Caltech chambers have been used to constrain the comprehensive chemical mechanisms for SOA formation (McVay et al., 2016; Sunol et al., 2018). In addition, the empirical data are also used to parameterize SOA formation in large-scale atmospheric models that predict the climate feedbacks to human activities (Bates et al., 2016). While many more atmospheric chambers in the US, similar to the Caltech chambers, are making key contributions to improve our understanding of atmospheric sciences, there is no central data storage mechanism to organize the vast amount of information from chamber research. The limited public accessibility and the lack of a shareable platform hinder a wider application of these valuable information. Furthermore, the chamber-to-chamber variations in experimental data resulted from chamber characteristics, data analysis methods, operational protocols, and instrumentation features have never been evaluated rigorously, which also obstructs data comparisons and integration.

Here we develop an open-access online infrastructure, the Index of Chamber Atmospheric Research in the United States (ICARUS, `https://icarus.ucdavis.edu/`), to store, archive, organize, and use atmospheric chamber data across the major institutions in the US (Table 5.1). In order to facilitate this process for the Caltech chambers users, the metadata, which is defined as a set of data that describes and gives information about other data, of the chamber characteristics and instrumentation have been documented. A convention to report experimental data has also been established for the Caltech chambers, as well as a user-friendly interface to assist the Caltech researchers to archive experiment data. In addition, a comprehensive description of chamber experimental protocol to conduct photochemical experiment project yield study using α-pinene + OH has also been prepared to lead and to conduct the inter-comparison study between different chambers.

5.2 Chamber Data Organization and Archiving Convention

One of the major objectives for ICARUS is to extend chamber data accessibility to a broader community, especially to the modelers who use experimental chamber data

to develop atmospheric physical or chemical mechanisms. Therefore, data utilities have to be ensured for end users and data have to be documented carefully with information that describes the main dataset, which is often referred to as metadata. This supplemental documentation should cover information that can constrain the experimental data, such as specific chamber characteristics, experimental timeline with key actions, instrumental notes, data analysis and quantification, etc. A uniform metadata template has been developed and tested across the ICARUS collaboration.

Chamber characteristics

Chamber characteristics provide a detailed description of each atmospheric chamber from each institution, including chamber physical properties, mixing protocols, cleaning/flushing protocols, temperature controls, and humidity controls. In addition to the conventional Teflon chambers, the Caltech research group also uses a Photooxidation Flow Tube (CPOT) to study gas-phase atmospheric chemistry and SOA formation (Huang et al., 2017). Table 5.2 lists the important characteristics of near bag, far bag, and CPOT, respectively. In addition, since the impact of chamber-to-chamber variances can be significant on experimental results, particle wall loss, vapor-wall loss, and light flux characterization data are also provided for each chamber so that the end users can correct the data in a uniform manner. At Caltech, particle wall loss is characterized following the protocol as described in Charan et al. (2018), vapor-wall loss as in Huang et al. (2018), and light flux as the k1 method in Zafonte et al. (1977) with a quartz k1 tube from UC Riverside.

Chamber experiment timeline

In an effort to record noteworthy actions in an experiment, such as seed injection, photolysis initiation, and offline sample collection, each archived experiment must be accompanied by one timeline document that serves as electronic experiment notes. A user-friendly ICARUS timeline generator tool has been developed in MATLAB®, which allows users to generate new experiment timeline, to edit experimental procedures, to add extra experiment steps, and to automatically reorder the procedures based on the times from user input (Figure 5.1). The method also reads computer local time zones automatically. All the user input information is acquired from user-interface windows and no editing within the script is needed. The auto-generated timeline includes two columns: time and action, the format of which, in comma-separated values (.CSV), is compatible with the ICARUS website uploading requirement. This script is shared among all the ICARUS participating

groups.

Instrument documentation and experiment data convention

In order to better understand the data collected from different instruments, every instrument has one metadata document that describes the instrument make, model, measurement type, data recording frequency, sensitivity and limits-of-detection, and methods and protocols for data analysis, quantification, calibration, sampling and uncertainty estimation. The Caltech chamber analytical suite includes a XMAN SMPS, a RHT Probe, a CIMS, a GC-FID, a HR-ToF-AMS, a PILS+LC−ESI−MS, and two NO_x monitors. A data format converting tool that convert the Caltech default instrument data into ICARUS compatible format (in .csv) has been developed in MATLAB®, with details listed in Table 5.4.

XMAN SMPS

The soft x-ray differential mobility analyzer in negative mode, or the XMAN SMPS, measures online particle size distribution during chamber experiments. The instrument was built in 2019, and data recording is accomplished using National Instrument® FPGA data acquisition board with LabVIEW, and data analysis is done in MATLAB®. The instrument employs a Po-210 ion source, a TSI 3081A long-column differential mobility analyzer (DMA), and an Aerosol Dynamics Inc. (ADI) MAGIC ™ water-based CPC. The raw data time resolution, i.e., data recording frequency, of the XMAN SMPS is 0.5 s, with analysis data averaging over 330 s. The detection limit for the XMAN SMPS is 10 nm - 1 μm with low sensitivity to temperature. The sensitivity to relative humidity remains low up to 40% RH, where a dryer tube is needed to connect before the inlet and particle size needs to be corrected based on reduced humidity. Sample is directly withdrawn at 0.5 L/min from the chamber through a 80 cm long, 1/4 inch stainless-steel tubing, with a mean sample residence time of 13 second. Data analysis is carried through using the data inversion method developed based on finite-element analysis of particle trajectories along the differential mobility analyzer column, Monte Carlo simulation of particle Brownian motion, and modeling of the condensation particle counter residence time distribution (Mai and Flagan, 2018; Mai et al., 2018). The custom-built MATLAB® software takes in the raw output from the instrument (particle counts), and inverts it to particle size distribution. Flow calibration is performed by fitting pressure transducer response current to flow rates measured from Gilibrator directly. Voltage calibration is done by fitting high-voltage source loop feedback current to the true

voltage measured by a multimeter connected to a high-voltage probe. Mobility peaks are verified by the measuring the transfer functions of spherical polystyrene latex particles of different sizes (50 nm, 150 nm, 300 nm, 500 nm, 750 nm). Calibration drift is estimated to be low and calibration is performed as needed. The measurement uncertainty is around 10%. Data is reported in $\mathrm{d}N/\mathrm{d}\log d_\mathrm{p}$ as cm^{-3} at different diameters.

RHT Probe

The Vaisala HMM211 humidity and temperature (RHT) Probe (built in 2009) measures online temperature and relative humidity (RH) during chamber experiments. The data recording is accomplished using National Instrument® data acquisition board with LabVIEW, and data is recorded in .txt format. The raw data time resolution, i.e., data recording frequency, is 30 s. RH can be calibrated from 11% to 95% using LiCl, KNO3, $Mg(NO_3)_2$ and $MgCl_2$ salts. The calibration is not likely to drift and only needs to be performed every few years. The temperature (in °C) and RH (in%) values for the chamber experiments are often averaged over time, with one standard deviation as the measurement uncertainty ($T \pm 0.2$°C).

CIMS

The Varian 1200 Triple Quadrupole chemical ionization mass spectrometer with CF_3O^-, or the CIMS (built in 2008), measures the concentration (in ppb) of gas-phase compounds when conducting chamber experiments (online). The data is recorded every ~3 mins (162 - 172 s for benzyl alcohol), and is normalized using the m/z = 86 peak (the M+1 peak for CF_3O^-). The measurements are very sensitive to RH, and water signals must be accounted for when analyzing CIMS data. Different compounds are identified by scan numbers (m/z number) and the data is analyzed in MATLAB®. For example, benzyl alcohol concentration can be calculated using m/z = 193, which is the sum of the mass of benzyl alcohol and CF_3O^-. We first divide the signal of m/z = 193 by that of m/z = 86, and then use the calculated ratio to compare to the normalized signal value from calibration. The calibration is performed by diluting a known concentration of gaseous compound (~44 ppb benzyl alcohol) in a 800 L Teflon bag. The concentration of the gas-phase compound in this bag is verified using Fourier transform infrared absorption (FT-IR) spectroscopy with a 19 cm path-length and absorption cross sections from the Pacific Northwest National Laboratory (PNNL) database (Sharpe et al., 2004). In this way, any wall

or sampling loss can be accounted for since the CIMS is sampled from the same volume as the FT-IR. Multiple FT-IR samples must be taken until they give the same concentration, thereby ensuring a minimal effect from any compound deposited on the instrument walls. The standard deviation of the compound mixing ratio along with the uncertainty in the calibration is used to estimate the uncertainty of the initial mixing ratio of the compound during the background collection period of each experiment (first ~1 h), as well as the time-dependent gas-phase mixing ratios throughout the entire experiment. For SOA yield studies, where the reacted gaseous compound concentration is measured by subtracting the initial concentration from the time-dependent gas-phase concentration, the variance of the reacted concentration is the sum of the variances of the two values. The uncertainty is then reported as the square root of the reacted compound mixing ratio variance.

GC-FID

The Hewlett Packard® 6890N gas chromatograph with flame ionization detector (GC-FID) measures gas-phase compound concentration as low as 10 ppt throughout the experiment. Data is recorded by the HPCore Chemstation software every 14 min. The concentration is computed by integrating the peak area of the spectrum. Calibration for the GC-FID is done similarly as the CIMS, through pillow bag dilution using FT-IR and the PNNL absorption database. The drift is estimated to be low and the uncertainty is roughly 10%.

HR-ToF-AMS

The Aerodyne 215-037 high-resolution time-of-flight aerosol mass spectrometer (HR-ToF-AMS) measures submicrometer, nonrefractory aerosol chemical composition, with chemical speciation of sulfate, nitrate, ammonium, chloride, and organic aerosol constituents. The data is recorded with ToF-AMS DAQ v4.0.40 and data can be analyzed with SQUIRREL v1.61 and PIKA v1.21 modules for Igor Pro, which needs to be corrected for gas-phase interferences (e.g., N_2 interfering with aerosol-derived CO at m/z = 28) and composition-dependent collection efficiencies. The raw data time resolution is 100 Hz and data is averaged every 10 s (0.1 Hz). The detection limits for each class of chemical constituents are calculated as three times the standard deviation of blank signals measured from high-efficiency particulate air (HEPA) filter samples taken before each experiment. Submicrometer aerosol particles (35 nm - 1.5 μm) is sampled into the instrument through an aerodynamic

lens at a flow rate of ~1.3 mL/s, producing a collimated particle beam that is directed onto a resistively heated surface where particles undergo vaporization (~600 °C) and electron impact ionization (~70 eV). Ions formed via electron impact ionization are then detected with a custom-designed Tofwerk HR-ToF-MS configured in V-mode and operating at a mass resolution of ~2100. The instrumental ionization efficiency is calibrated using dry, 350 nm ammonium nitrate particles that are size-selected by a DMA operating in static mode. Mass loadings of sulfate, ammonium, chloride, and organic aerosol constituents are reported as "nitrate equivalent mass loadings (μg/m^3)," assuming ionization efficiencies for these species relative to nitrate. The analyzed data can be reported as, O:C, the oxygen to carbon atom ratio, H:C, the hydrogen to carbon atom ratio, N:C, the nitrogen to carbon atom ratio, and OM:OC, the organic mass to organic carbon ratio (Aiken et al., 2008). The calibration drift is estimated to be low and the uncertainties for O:C and H:C are estimated to be ±30% and ±10%, respectively.

PILS+LC−ESI−MS

The particle-into-liquid sampler (PILS) coupled with the ultra-performance liquid chromatography/electrospray ionization quadrupole time-of-flight mass spectrometry (UPLC/ESI-Q-TOF-MS, built in 2014), or the PILS+LC-ESI-MS, is an offline technique to measure the negative (−) and positive (+) ion mass spectra from m/z 40 to 1000 of SOA molecular constituents in PILS samples. Analytes are detected as $[M\text{-}H]^-$ ions in negative mode, and as both $[M+H]^+$ ions as well as adducts with Na^+ and NH_4^+ in positive mode. The Caltech PILS is based on a modification of the original design of Weber et al. (2001). Sample is collected every 5 minutes at 12.5 L/min and a total of 48 liquid samples can be collected for chamber experiments within ~ 4 hr duration. The detection limit of the PILS sample is 10 ppbm. PILS samples are then analyzed by a Waters ACQUITY UPLC I-Class system coupled to a Xevo® G2-S Q-TOF-MS equipped with an ESI source and operating at a mass resolution of 20,000-34,000 and a mass accuracy of <5 mDa. The detailed operating parameters of the instrument, and methods for PILS sampling, chemical identification, data analysis, quantification, calibration, and uncertainty estimation, can be found in the Supporting Information of Kenseth et al. (2018). Uncertainty in the PILS method is mainly related to the variation in the collected liquid volume due to the existence of air bubbles, and has been estimated to be ±11%. Uncertainty associated with the chromatographic and mass spectral reproducibility of the UPLC/ESI-Q-TOF-MS is estimated to be ±3%.

NO_x monitors

The Teledyne T200 NO_x monitor, NO_xTele (built in 2012), measures the NO and NO2 concentrations. Data acquisition is achieved using LabView, with a frequency of 30 s. The detection limit is 1 PPM. Samples are drawn at 200 mL/min from the chamber directly and then passed through a filter to remove O_3. Calibration using 889.5 ppb (±5%) NO needs to be done frequently as the drift is estimated to be relatively high (50% in 6 months).

The Fritz Aerometric Technologies Luminol NO2/Acyl Peroxynitrate Analyzer, or the NO_xLum, measures NO_2 and peroxyacyl nitrates (PAN) concentrations. Both data acquisition and analysis are accomplished using Labview, with a frequency of 10 s. The NO_xLum shares the same sampling line as the NO_xTele. The NO_2 signals may be interfered with CH_3ONO, organic nitrates, nitric acid, or other NO_y compounds. Measurement uncertainties for both instruments are estimated to be 10%.

5.3 The ICARUS Online Database

The ICARUS online website (`https://icarus.ucdavis.edu/`) has been built from scratch on a PHP framework by the ICARUS website developers based on the content that is agreed on by the participating institutions. An organization for the Caltech facilities, "Caltech Atmospheric Chamber", has been created on the website as an "Organization" (Figure 5.2). Three chamber and nine instruments, along with the metadata and characteristics documentation as discussed above, are listed under the organization. Experiment set, a series of chamber experiments that serve similar scientific purpose, can be added in one specific chamber. A publication associated with the experiment set can also be created with details such as title, author list, DOI number, publisher details and manuscript abstract. Each experiment set will have its associated characterization files, instrument, and publication. Experiment data, organized following the reporting convention, can be uploaded for each instrument separately.

Extensive work has been done to minimize the labor that is involved in uploading and describing experimental dataset while upholding the high quality of data. For example, reactant can be added to the experiment though an interactive search using the PubChem database so that the synonyms for each compound can be controlled by its CAS number. Experiments can be copied both within one experiment set and across different sets to reduce redundancy in the form-filling and data upload

process. One experiment set can be downloaded as one zip file, that contains a table of content with a set identification number, datasets from all experiments, characterization data, and experiment set description. Each data file contains the corresponding instrument metadata in addition to the main data. Furthermore, although uploaded datasets are in default available to public to promote broad dissemination of publically funded data, they can be set to private temporarily so that provisional data can also be organized and stored using the same format. The website is still undergoing testing by research groups to further refine the data storage fields, remove redundancy, identify bugs and improve user-interface.

5.4 Inter-comparison Study Experimental Protocol

The ICAURS inter-comparison studies aim to help us to understand the similarities and differences of participating chambers when characterization studies are performed with the same protocols (Table 5.3). It is recommended that the following procedure (Kenseth et al., 2018) be carried out by each participating chamber as part of the ICARUS inter-comparison photochemical experiment product yield study using α-pinene + OH. The purpose of this study is to compare SOA and individual product yields using vapor/particle wall loss corrections and the photon flux protocol to determine modeled vs. experimental OH (via decay of VOC).

Suggested procedures

α-Pinene photooxidation experiments will be carried out at ambient temperature (~295 K), atmospheric pressure (~1 atm), and low relative humidity (~15% RH). At Caltech, temperature and RH will be monitored with a Vaisala HMM211 probe. Experiments will be performed in the presence of $(NH_4)_2SO_4$ seed aerosol, and at an initial NO_x mixing ratio of 15 ppb (injected as pure NO). At Caltech, O_3 and NO_x mixing ratios are quantified by a Horiba APOA-360 O63 absorption monitor and a Teledyne T200 NOx monitor, respectively. The detection limits for O_3, NO, and NO_2 are 0.5, 0.4, and 0.4 ppb, respectively. Prior to each experiment, the chamber should be flushed with dry, purified air for 24 hr such that the particle number and volume concentrations are less than 10 cm^{-3} and 0.01 μm^3 cm^{-3}, respectively. α-Pinene (>99%, Sigma-Aldrich) should be injected into the chamber such that the initial mixing ratio is ~100 ppb. Polydisperse seed aerosol should be generated via atomization of a dilute (0.06 M) aqueous solution of $(NH_4)_2SO_4$, followed by diffusive drying and neutralization. The target volume concentration and mean particle diameter are ~70 μm^3 cm^{-3} and ~100 nm, respectively. H_2O_2 should

serve as the source of OH radical on photolysis under broadband UV irradiation. At the slow H_2O_2 photolysis rate in the Caltech chamber (350 nm backlights) and the relatively high initial mixing ratios of H_2O_2, steady-state OH and HO_2 concentrations are achieved (Eddingsaas et al., 2012). The initial H_2O_2 mixing ratio should produce steady-state OH and HO_2 concentrations of ~ 2×10^6 and ~1 1×10^10 molecules cm^{-3}, respectively. At Caltech, this requires an initial H_2O_2 mixing ratio of ~2 ppm. Experiments should be run for 4 hr.

Instrumentation

The required instruments to perform the propose experiment include: an instrument to monitor α-pinene mixing ratio, such as PTR-MS, SIFT-MS, GC-FID, GC-ECD, IMS, or similar; an instrument to monitor gaseous oxidation products, such as negative ion CIMS (any reagent ion), PTR-MS, SIFT-MS, or similar; an instrument to monitor particle size and concentration, such as SMPS, AMS, or similar. It is optional to have an instrument to monitor particle composition, PILS coupled with HPLC, FIGAERO, or similar.

Example calibration and data analysis protocols for Caltech chamber

Gas-phase α-pinene mixing ratio using GC-FID

α-Pinene mixing ratios are quantified with an Agilent 6890N gas chromatograph equipped with a flame ionization detector (GC-FID) and operated with an Agilent HP-5 column (30 m × 0.32 mm, 0.25 μm). The GC-FID is calibrated with a commercial α-pinene standard (>99%, Sigma- Aldrich) over a mixing ratio range from 100 to 200 ppb using a gas-tight volumetric syringe and a mass-controlled dilution flow of N_2 into a 100 L Teflon bag. At Caltech, the GC-FID is also calibrated with ppm-level bags (10-20 ppm) prepared via an analogous method and cross-calibrated using Fourier transform infrared spectroscopy (FT-IR) with tabulated absorption cross sections for α-pinene (Sharpe et al., 2002).

SMPS data analysis

At Caltech, SMPS data analysis is carried out through data inversion based on finite-element analysis of particle trajectories along the DMA, Monte Carlo simulation of particle Brownian motion, and residence time distribution modeling of CPC (Mai and Flagan, 2018; Mai et al., 2018). Based on instrumental limitations and inversion accuracies, the SMPS used in the Caltech chamber can measure particle-size distributions from 20 nm up to 800 nm, which is sufficient to cover the SOA size range in

this experiment. Noted that using different DMA transfer functions (Stolzenburg, 1988; Russell et al., 1995; Collins et al., 2004; Mamakos et al., 2008; Dubey and Dhaniyala, 2011) and instrumentation setup may result in differences in SOA yield calculations. As a result of particle growth driven by gas/particle-phase chemistry and gas-particle partitioning, mean geometric diameters typically shift from ~100 nm to ~230 nm after a 4 hr experiment. Aerosol volume concentrations are calculated from particle size distributions assuming homogenous spherical particles. Aerosol mass concentrations are derived assuming an effective density for α-pinene SOA of 1.25 g mL^{-1}.

AMS data analysis

AMS ionization efficiency is calibrated using dry, 350 nm NH_4NO_3 particles, generated from a dilute (0.01 M) aqueous solution of NH_4NO_3 and size-selected with a DMA. Detection limits for each class of chemical constituents are calculated as three times the standard deviation of blank signals measured from HEPA filter samples (~30 min) taken before each experiment. AMS data are analyzed using the SQUIRREL and PIKA modules for Igor Pro, and are corrected for gas-phase interferences (Aiken et al., 2008; Allan et al., 2004) and composition-dependent collection efficiencies (Middlebrook et al., 2012). Elemental O:C and H:C ratios are calculated using the "Improved-Ambient" elemental analysis method for AMS spectra (Canagaratna et al., 2015).

5.5 Summary and Future Work

Here we have developed a uniform convention to report Caltech atmospheric chamber data and metadata. Multiple user-friendly interfaces have also been established to assist the Caltech chamber users to organize experiment data. One full experiment set with 19 benzyl alcohol experiments have been uploaded on the ICARUS online database, and more legacy data that produced significant research values will be archived in the future. The development of this open-access database will likely foster collaboration between atmospheric chemistry researchers and maximize the discovery and use of atmospheric chamber datasets. These collaborative efforts are not only limited to the current participating institutions in the US, but can be expanded to researchers in other countries. As a sister initiative to EUROCHAMP (`http://www.eurochamp.org`) (Muñoz and Gómez-Alvarez, 2008; Wiesen, n.d.), ICARUS will help to increase the global reach of atmospheric data sharing. In addition, the project development occurs in parallel with the development of the

Data Asset Services Hub (DASH) at the National Center for Atmospheric Research (NCAR). The datasets and data management policies of ICARUS will be integrated with DASH for long-term data storage and management.

5.6 Code availability

Codes for the Caltech data archiving tools (timeline generator and data converter tool) can be found on `https://github.com/caltechchamber/icarus_tool` with detailed user instructions.

Acknowledgement

The authors would like to thank Dr. Tran B. Nguyen and NCAR for leading the development of the ICARUS infrastructure. This work was supported by the National Science Foundation under Grant No. AGS 1740552.

Institution	Principal Investigator	Years of Data	Volume	Chamber Material	Lights	Temperature Control?	Mixing Fan?
Caltech	Seinfeld, John H.	10+ Years	18 m^3	Teflon	UV black lamps	10 - 45 °C	No
Carnegie Mellon University	Donahue, Neil M. and Robinson, Allen L.	10+ Years	12 m^3	Teflon	UV black lamps	5 - 25 °C	No
CU Boulder	Jimenez, Jose L.	1-5 Years	25 m^3	Teflon	UV black lamps + visible lamps	4 - 40 °C	Some exp., Teflon fans
CU Boulder	Ziemann, Paul J.	10+ Years	8 m^3	Teflon	UV black lamps	No	Teflon coated Al
Georgia Tech	Ng, Nga Lee	1-5 Years	13 m^3	Teflon	UV black lamps + natural sunshine fluorescent lights	4 - 40 °C	No
NCAR	Tyndall, Geoffrey S. and Orlando, John J.	10+ Years	0.05 and 8 m^3 and	Stainless steel and Teflon	Xe lamps and UV black lamps	-47 - 77 °C	No
UC Davis	Nguyen, Tran B.	None	4 - 10 m^3	Teflon	UV black + UV-B lamps	10 - 50 °C	No
UC Irvine	Nizkorodov, Sergey A.	1-5 Years	5 m^3	Teflon	UV black + UV-B lamps	No	Only during filling; plastic
UC Riverside	Cocker, David R. and Carter, William P.L.	10 + Years	2 - 100 m^3	Teflon, some Teflon coated Al	UV black lamps, Ar and Xe lamps, sunlight	5 - 40 °C	Only prior to reaction
UT Austin	Hildebrandt Ruiz, Lea	1-5 Years	12 m^3	Teflon	UV black lamps	2 - 40 °C	No

Table 5.1: Institutions participating in ICARUS and their chamber characteristics. All the listed chambers have humidity controls and are primarily operated in batch mode.

Characteristics	Near Bag	Far Bag	CPOT
Volume (m^3)	19	18	0.043
Shape	Rectangular Prism	Rectangular Prism	Cylindrical
Surface area (m^2)	41.8	41.8	1.18
Flow Mode	Batch	Batch	Flow-through
Flow Rate (L/min)	N.A.	N.A.	2
Body Material	Teflon	Teflon	Quartz
Body thickness (mil)	50	50	N.A
Replacement date	08/08/17	08/08/17	N.A
Mixing	N.A.	N.A.	Axial dispersion

Table 5.2: Chamber characteristics for the Caltech Near Bag, Far Bag, and CPOT. Note that each chamber can be cleaned with air flushing, and CPOT can also be cleaned with solvent when necessary. The three chambers use the same temperature (20 - 45 °C) and relative humidity (5 - 100%) controls. The mixing of the two Teflon chambers is accomplished by injecting additional inflow air to the chamber.

Experiment	Leading Institution	Project Goals
Particle wall loss	UC Riverside	Comparison of wall loss trends and corrected particle concentrations using inorganic seeds
Vapor wall loss	CU Boulder	Comparison of wall loss trends and corrected vapor mixing ratios
Photolysis measurements	UC UC Irvine	Comparison of modeled and measured $J(NO_2)$ and $J(H_2O_2)$
Project yield study, dark experiment	Carnegie Mellon University	Possibly O3 + α-Pinene with Scavenger; Comparison of SOA yield and some product yields, using the particle and vapor loss corrections
Project yield study, photochemical experiment	Caltech	Possibly OH + α-Pinene; Comparison of SOA yield and some product yields, using the particle/vapor loss corrections and photolysis measurement to determine modeled OH vs. experimental OH

Table 5.3: Proposed experiments for the ICARUS inter-comparison study with experimental details and leading research groups.

Data Type	Original File Format	Output Format (Archiving Convention, in .csv)
Timeline	Default list of experimental actions in .xlsx	Time (HH:MM) + Actions
SMPS	Data structure in .mat	Time series $\mathrm{d}N/\mathrm{d}\log d_\mathrm{p}$ for all the size bins and total number, surface and volume concentrations
GC-FID	Manually integrated peak area input in .xlsx or peak area integrated and saved in .mat	Time series concentrations (in ppb)
CIMS	Data structure in .mat	Time series m/z information
RHT	.txt (directly from the instrument)	Time series RHT data
NO_x/O_3	.txt (directly from the instrument)	Time series NO_x/O_3 data

Table 5.4: ICARUS experiment data formatting convention with the file converting tool. Since the data reporting format of the HR-ToF-AMS and the PILS+LC-ESI-MS can vary given the different scientific nature of the experiments, there is currently no convention established for these two instruments for Caltech chamber users.

Time should be recorded in 24-hour Clock, HH:MM, as is in local time
Avoid using comma "," in descriptions; do not use enter to start a new line
To Add a new step, just add to the empty row in the end or overwrite the unused default lines
No need to delete step as everthing without a timestamp will be deleted with the reordering function
Close this window when finished, everything will be saved automatically

	Time (America/Los_Angeles)	Action
1		GC on
2		RHT/NOx/O3 on
3		AMS on filter
4		AMS on chamber
5		SMPS on
6		CIMS on
7		PILS on
8		OH injection starts
9		OH injection ends (OH concentration is...)
10		VOC injection starts (VOC compound is...)
11		VOC injection ends (VOC concentration is ...)
12		Seed injection starts
13		Seed injection ends (seed concentration is...)
14		Time background starts
15		Lights on
16		Lights off
17		Refill bag starts
18		Refill bag ends
19		Mixing starts
20		Mixing ends
21		Wall loss starts
22		Wall loss ends
23		GC off
24		RHT/Nox/O3 off
25		AMS off
26		DMA off
27		CIMS off

Figure 5.1: A list of default experiment procedures in the ICARUS timeline generator

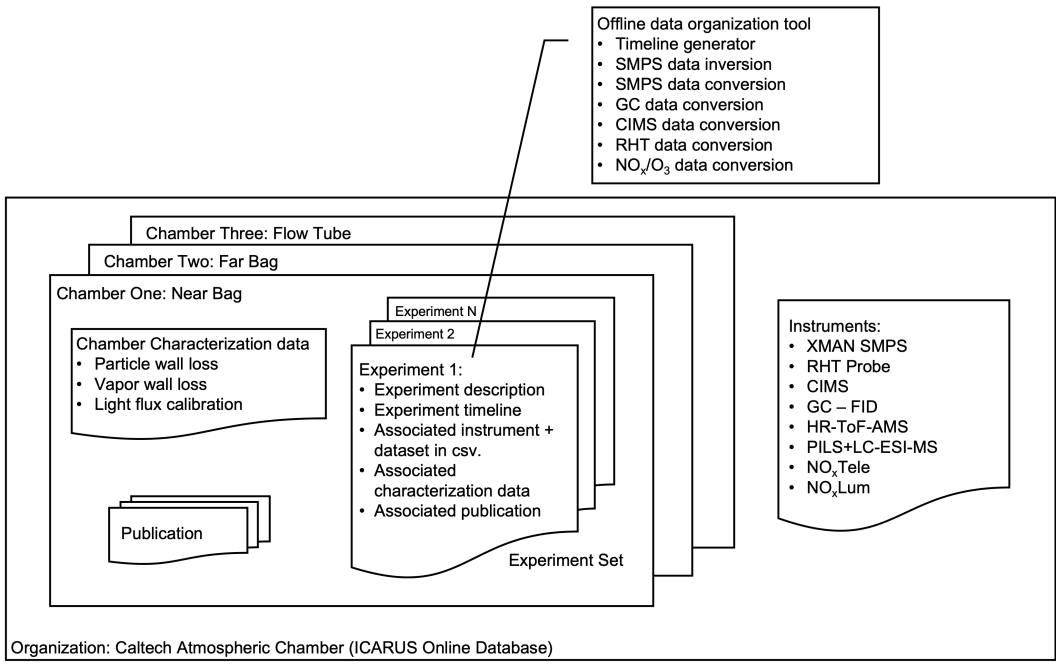

Figure 5.2: A simplified entity-relationship diagram for the Caltech Atmospheric Chamber.

References

A. C. Aiken et al. (June 2008). "O/C and OM/OC Ratios of Primary, Secondary, and Ambient Organic Aerosols with High-Resolution Time-of-Flight Aerosol Mass Spectrometry". In: *Environmental Science & Technology* 42.12, pp. 4478–4485. ISSN: 0013-936X. DOI: 10.1021/es703009q.

J. D. Allan et al. (July 2004). "A generalised method for the extraction of chemically resolved mass spectra from Aerodyne aerosol mass spectrometer data". en. In: *Journal of Aerosol Science* 35.7, pp. 909–922. ISSN: 0021-8502. DOI: 10.1016/j.jaerosci.2004.02.007.

K. H. Bates et al. (Jan. 2016). "Production and Fate of C4 Dihydroxycarbonyl Compounds from Isoprene Oxidation". In: *The Journal of Physical Chemistry A* 120.1, pp. 106–117. ISSN: 1089-5639. DOI: 10.1021/acs.jpca.5b10335.

M. R. Canagaratna et al. (Jan. 2015). "Elemental ratio measurements of organic compounds using aerosol mass spectrometry: characterization, improved calibration, and implications". English. In: *Atmospheric Chemistry and Physics* 15.1, pp. 253–272. ISSN: 1680-7316. DOI: https://doi.org/10.5194/acp-15-253-2015.

S. M. Charan et al. (May 2018). "Effect of Particle Charge on Aerosol Dynamics in Teflon Environmental Chambers". In: *Aerosol Science and Technology* 0.ja, pp. 1–46. DOI: 10.1080/02786826.2018.1474167.

D. R. Cocker et al. (June 2001). "State-of-the-Art Chamber Facility for Studying Atmospheric Aerosol Chemistry". In: *Environmental Science & Technology* 35.12, pp. 2594–2601. ISSN: 0013-936X. DOI: 10.1021/es0019169.

D. R. Collins et al. (Aug. 2004). "The Scanning DMA Transfer Function". In: *Aerosol Science and Technology* 38.8, pp. 833–850. ISSN: 0278-6826. DOI: 10.1080/027868290503082. (Visited on 05/09/2020).

P. Dubey and S. Dhaniyala (Aug. 2011). "A New Approach to Calculate Diffusional Transfer Functions of Scanning DMAs". In: *Aerosol Science and Technology* 45.8, pp. 1031–1040. ISSN: 0278-6826. DOI: 10.1080/02786826.2011.579644. (Visited on 05/09/2020).

N. C. Eddingsaas et al. (July 2012). "α-pinene photooxidation under controlled chemical conditions – Part 1: Gas-phase composition in low- and high-NO_x environments". English. In: *Atmospheric Chemistry and Physics* 12.14, pp. 6489–6504. ISSN: 1680-7316. DOI: https://doi.org/10.5194/acp-12-6489-2012.

Y. Huang et al. (Jan. 2017). "The Caltech Photooxidation Flow Tube reactor: design, fluid dynamics and characterization". en. In: *Atmospheric Measurement Techniques* 10.3. DOI: 10.5194/amt-10-839-2017.

Y. Huang et al. (Feb. 2018). "Unified Theory of Vapor–Wall Mass Transport in Teflon-Walled Environmental Chambers". In: *Environmental Science & Technology* 52.4, pp. 2134–2142. ISSN: 0013-936X. DOI: 10.1021/acs.est.7b05575.

C. M. Kenseth et al. (Aug. 2018). “Synergistic O3 + OH oxidation pathway to extremely low-volatility dimers revealed in -pinene secondary organic aerosol”. en. In: *Proceedings of the National Academy of Sciences* 115.33, pp. 8301–8306. ISSN: 0027-8424, 1091-6490. DOI: 10.1073/pnas.1804671115.

C. L. Loza et al. (June 2013). “On the Mixing and Evaporation of Secondary Organic Aerosol Components”. In: *Environmental Science & Technology* 47.12, pp. 6173–6180. ISSN: 0013-936X. DOI: 10.1021/es400979k.

H. Mai and R. C. Flagan (Dec. 2018). “Scanning DMA Data Analysis I. Classification Transfer Function”. In: *Aerosol Science and Technology* 52.12, pp. 1382–1399. ISSN: 0278-6826. DOI: 10.1080/02786826.2018.1528005. (Visited on 05/09/2020).

H. Mai et al. (Dec. 2018). “Scanning DMA data analysis II. Integrated DMA-CPC instrument response and data inversion”. In: *Aerosol Science and Technology* 52.12, pp. 1400–1414. ISSN: 0278-6826. DOI: 10.1080/02786826.2018.1528006. (Visited on 05/09/2020).

A. Mamakos et al. (Mar. 2008). “Differential mobility analyser transfer functions in scanning mode”. en. In: *Journal of Aerosol Science* 39.3, pp. 227–243. ISSN: 0021-8502. DOI: 10.1016/j.jaerosci.2007.11.005.

R. C. McVay et al. (Mar. 2016). “SOA formation from the photooxidation of -pinene: systematic exploration of the simulation of chamber data”. English. In: *Atmospheric Chemistry and Physics* 16.5, pp. 2785–2802. ISSN: 1680-7316. DOI: https://doi.org/10.5194/acp-16-2785-2016.

A. M. Middlebrook et al. (Mar. 2012). “Evaluation of Composition-Dependent Collection Efficiencies for the Aerodyne Aerosol Mass Spectrometer using Field Data”. In: *Aerosol Science and Technology* 46.3, pp. 258–271. ISSN: 0278-6826. DOI: 10.1080/02786826.2011.620041.

A. Muñoz and E. Gómez-Alvarez (2008). “Overview Of The Eurochamp Database Of European Atmosphere Simulation Chambers”. en. In: *Simulation and Assessment of Chemical Processes in a Multiphase Environment*. Ed. by I. Barnes and M. M. Kharytonov. NATO Science for Peace and Security Series C: Environmental Security. Dordrecht: Springer Netherlands, pp. 61–70. ISBN: 978-1-4020-8846-9. DOI: 10.1007/978-1-4020-8846-9_5.

N. L. Ng et al. (Aug. 2008). “Secondary organic aerosol (SOA) formation from reaction of isoprene with nitrate radicals (NO_3)”. English. In: *Atmospheric Chemistry and Physics* 8.14, pp. 4117–4140. ISSN: 1680-7316. DOI: https://doi.org/10.5194/acp-8-4117-2008.

T. B. Nguyen et al. (Jan. 2014). “Overview of the Focused Isoprene eXperiment at the California Institute of Technology (FIXCIT): mechanistic chamber studies on the oxidation of biogenic compounds”. en. In: *Atmospheric Chemistry and Physics* 14.24. DOI: 10.5194/acp-14-13531-2014.

L. M. Russell et al. (Jan. 1995). “Asymmetric Instrument Response Resulting from Mixing Effects in Accelerated DMA-CPC Measurements”. In: *Aerosol Science and Technology* 23.4, pp. 491–509. ISSN: 0278-6826. DOI: 10.1080/02786829508965332. (Visited on 05/06/2020).

R. H. Schwantes et al. (Aug. 2016). “Science of the Environmental Chamber”. In: *Advances in Atmospheric Chemistry*. Vol. Volume 1. Advances in Atmospheric Chemistry Volume 1. World Scientific, pp. 1–93. ISBN: 978-981-314-734-8. DOI: 10.1142/9789813147355_0001.

S. W. Sharpe et al. (2002). “The PNNL quantitative IR database for infrared remote sensing and hyperspectral imaging”. In: *Applied Imagery Pattern Recognition Workshop, 2002. Proceedings.* Pp. 45–48. DOI: 10.1109/AIPR.2002.1182253.

S. W. Sharpe et al. (Dec. 2004). “Gas-Phase Databases for Quantitative Infrared Spectroscopy”. EN. In: *Applied Spectroscopy* 58.12, pp. 1452–1461.

M. Shiraiwa et al. (July 2013). “Size distribution dynamics reveal particle-phase chemistry in organic aerosol formation”. en. In: *Proceedings of the National Academy of Sciences* 110.29, pp. 11746–11750. ISSN: 0027-8424, 1091-6490. DOI: 10.1073/pnas.1307501110.

M. R. Stolzenburg (1988). *An Ultrafine Aerosol Size Distribution Measuring System*. en. University of Minnesota.

A. M. Sunol et al. (Apr. 2018). “Computational simulation of the dynamics of secondary organic aerosol formation in an environmental chamber”. In: *Aerosol Science and Technology* 52.4, pp. 470–482. ISSN: 0278-6826. DOI: 10.1080/02786826.2018.1427209.

R. J. Weber et al. (Jan. 2001). “A Particle-into-Liquid Collector for Rapid Measurement of Aerosol Bulk Chemical Composition”. In: *Aerosol Science and Technology* 35.3, pp. 718–727. ISSN: 0278-6826. DOI: 10.1080/02786820152546761.

P. Wiesen (n.d.). “The EUROCHAMP Integrated Infrastructure Initiative”. en. In: (), p. 5.

L. Zafonte et al. (May 1977). “Nitrogen dioxide photolysis in the Los Angeles atmosphere”. English. In: *Environ. Sci. Technol.; (United States)* 11:5. DOI: 10.1021/es60128a006.

X. Zhang et al. (Nov. 2015). “Formation and evolution of molecular products in -pinene secondary organic aerosol”. en. In: *Proceedings of the National Academy of Sciences* 112.46, pp. 14168–14173. ISSN: 0027-8424, 1091-6490. DOI: 10.1073/pnas.1517742112.

Chapter 6

CONCLUSIONS AND FUTURE WORK

The foregoing chapters of this dissertation, along with the following appendices, have discussed a variety of approaches to help us understand climate forcings from human activities, in particular, from particulate matter. The importance of airborne particles for clouds formation and radiative forcing has been verified in many laboratory measurements, in situ observations, and large-scale climate models.

First the development of nanoparticle size-measuring technique was presented (Chapter 2, Appendix B). The nano-scanning electrical mobility spectrometer (nSEMS) has provided robust and effective particle size distribution measurements in the low-nanometer regime. The highly resolved size distribution data have helped to push the boundary of our understanding in critical aerosol dynamics of newly formed particles in atmospheric chamber studies. Well-controlled chamber experiments, along with many other state-of-the-art instruments, can provide valuable information when examining complex physical or chemical mechanisms of particle formation and growth (Chapter 3, Appendices C, D & E). While chamber studies can improve our understanding in fundamental sciences, field measurements (Appendix A) and model simulations (Chapter 4) are necessary to ensure that these data are realistic in ambient conditions and can be appropriately incorporated for evaluations of model mechanisms. In an effort to maximize chamber data usability, an online searchable public data infrastructure has been developed to streamline the data archiving, organizing, and sharing processes (Chapter 5).

Tremendous progress has been made in understanding atmospheric aerosol particles and their impact on cloud properties. However, the discrepancies between model simulations and observations still remain, largely due to the lack of representation of aerosol schemes in climate models. The detailed chemical and physical mechanisms of atmospheric new particle formation and secondary organic aerosol growth derived from chamber studies are often too computationally expensive to include in large-scale modeling. Yet the current simplified representation of these mechanisms and their contribution to cloud formation cannot fully capture the climate significance from these atmospheric constituents.

A new paradigm that can describe the interaction between aerosol, clouds, and

climate needs to be developed, incorporating the valuable in situ observations and laboratory measurements into climate models. Aerosol-cloud interaction remains to be one of the highly leveraged bottlenecks that experts have identified in climate change mitigation and that are believed to be particularly well-suited for machine learning applications (Rolnick et al., 2019). Data-driven machine learning algorithms have arisen as a powerful tool in parameterizing complex systems, including applications in climate sciences (Reichstein et al., 2019). For instance, random forest regression algorithms have been employed to replace the gas-phase chemical mechanism in GEOS-Chem and to explain PM10 concentration elevation in Switzerland (Grange et al., 2018; Keller and Evans, 2019). Gradient-boosted regression trees were used to determine a global spatial distribution of aerosol mixing state with respect to hygroscopicity (Hughes et al., 2018). Neural networks have been applied to successfully analyze the Carbon Bond Mechanism Z (CBM-Z) gas-phase chemical mechanism and to emulate the behavior of a high-resolution cloud simulation (Kelp et al., 2018). The viability of machine learning has offered an alternative to the existing physical model structures, which do not always offer great trade-offs between computation cost and accuracy. With the establishment of an online database which enables inter-chamber exchange of valuable experimental results, the accessibility to large quantity of high quality data will certainly facilitate this data-driven approach to study how aerosols affect clouds - and how clouds affect aerosols. Reducing the discrepancies between modeling and measurements on a global scale will undoubtedly help climate scientists to better estimate the Earth's radiation and climate change.

References

S. K. Grange et al. (May 2018). "Random forest meteorological normalisation models for Swiss PM_{10} trend analysis". English. In: *Atmospheric Chemistry and Physics* 18.9, pp. 6223–6239. ISSN: 1680-7316. DOI: https://doi.org/10.5194/acp-18-6223-2018.

M. Hughes et al. (Jan. 2018). "Machine Learning to Predict the Global Distribution of Aerosol Mixing State Metrics". en. In: *Atmosphere* 9.1, p. 15. DOI: 10.3390/atmos9010015.

C. A. Keller and M. J. Evans (Mar. 2019). "Application of random forest regression to the calculation of gas-phase chemistry within the GEOS-Chem chemistry model v10". English. In: *Geoscientific Model Development* 12.3, pp. 1209–1225. ISSN: 1991-959X. DOI: https://doi.org/10.5194/gmd-12-1209-2019.

M. M. Kelp et al. (Aug. 2018). "Orders-of-magnitude speedup in atmospheric chemistry modeling through neural network-based emulation". In: *arXiv:1808.03874 [physics, stat]*. URL: http://arxiv.org/abs/1808.03874.

M. Reichstein et al. (Feb. 2019). "Deep learning and process understanding for data-driven Earth system science". en. In: *Nature* 566.7743, pp. 195–204. ISSN: 1476-4687. DOI: 10.1038/s41586-019-0912-1.

D. Rolnick et al. (Nov. 2019). "Tackling Climate Change with Machine Learning". In: *arXiv:1906.05433 [cs, stat]*. URL: http://arxiv.org/abs/1906.05433.